

POLITECNICO DI TORINO

Master of Science in Aerospace Engineering

Final Project

**Design and aerodynamic characterization of a small UAV:
stability and control derivatives**



External advisors:

Prof. Elisa Franco (UCLA)
Ph.D. Candidate Raffaele Baggi (UCR)

Candidate:

Marco Mattei

Internal advisors:

Prof. Domenic D'Ambrosio
Prof. Gaetano Iuso

July 2020

Alla mia famiglia, che mi ha sempre sostenuto e appoggiato.

A tutti i miei amici che mi hanno accompagnato in questo percorso.

I would like to thank my roommates Mustafa, Raj, Juliet, and Kyle for all the good time we spent together in Riverside like a big family, making me feel like at home since the first day.

Abstract

In the present thesis, an unmanned aerial vehicle (UAV) is designed in terms of wing geometry and control surfaces available on it to represent a wide range of civil aircraft. However, unlike civil jet aircraft, the UAV will have a V-Tail.

The wing airfoil is chosen considering the UAV's flight regime. The airfoil's choice is done through two-dimensional CFD analysis at low to moderate Reynolds numbers. Due to the low computational power available, the analyses are done only for reduced angles of attack, which are representative of the flight condition of the cruise, and where the problem can be considered in the first approximation as steady-state. The CFD tool employed is ANSYS Fluent, and the Reynolds Averaged Navier Stokes equations are solved using the transitional model $k - kl - \omega$ for the incompressible flow over the airfoil. A more detailed analysis is performed on a test case to do the mesh independence study and compare the obtained numerical results with the experimental values available in literature. With the found mesh and model settings, two different class of airfoil are investigated, and the best airfoil in terms of effectiveness is individuated for each airfoils family.

The aerodynamic characterization of the UAV is done using XFLR5, open-source software that implements the vortex lattice method (VLM). Its numerical results are compared with the experimental results obtained for another UAV from wind tunnel investigation. The mesh independence study is conducted to individuate the optimal distributions of the panels and the best type of VLM. Therefore, the found XFLR5 settings are used for the UAV characterization. In the longitudinal static stability study, two wings are investigated. Thanks to the approximation of linear lift and moment at low angles of attack, the flight angle of attack and the elevator deflection are calculated. Moreover, the wing that allows the plane to fly at a minimum angle of attack and minimum elevator deflection is chosen. Later, the sideslip angle's influence on the UAV is examined. Finally, the control surfaces are studied, and it is showed how they affect the UAV's dynamic. A finite-difference finite scheme is used to calculate the UAV's aerodynamic and control derivatives, starting from the results obtained in XFLR5, where all the simulations are performed assuming small perturbations angles.

The obtained results indicate that the UAV is statically stable about the lateral axis, directionally stable, and the control surfaces can maneuver it. The UAV configuration seems to avoid the aileron-adverse yaw. However, the results obtained by XFLR5 need to be refined and validated using more accurate CFD analysis solving the RANS equations considering the effects of the parasite drag, and the fuselage. For doing that, the CAD file of the UAV would be used.

Contents

List of Tables

List of Figures

1	The UCR SkyTeam	1
1.1	Introduction to the Non-linear Adaptive Dynamic Control Allocation	1
1.2	Equipment used by the UCR SkyTeam	4
1.2.1	Radio-controlled aircraft	4
1.2.2	Avionics	6
1.3	Experimental flight test results	7
2	Design of the new small UAV	10
2.1	Reasons that lead to a new UAV	10
2.2	Small UAV requirements	11
2.3	Preliminary investigation	12
2.4	UAV wing geometry	13
2.5	UAV V-Tail	15
2.6	Control surfaces	17
2.7	Inertial properties	19
3	Two dimensional aerodynamic	23
3.1	Problem identification	23
3.2	Fundamental of airfoil aerodynamics	24
3.3	Laminar separation bubble	26
3.4	Turbulent boundary layer	28
3.5	Governing equations of fluid dynamics	30
3.6	Numerical solution of the Navier-Stokes equations	32
3.6.1	State of art: different computational tools	32
3.6.2	RANS $k - kl - \omega$ model	32
3.6.3	Discretization	35
3.6.4	Solver	36

4	Two dimensional CFD analysis of different airfoils	38
4.1	Airfoils identification	38
4.2	Test case	39
4.2.1	Computational domain	40
4.2.2	Computational and physical parameters	42
4.2.3	Results	46
4.2.4	CFD results: GEMINI airfoil at $\alpha = 0.76^\circ$	49
4.3	Airfoils selection	51
5	Validation of the XFLR5's results	53
5.1	Laplace's equation	53
5.2	Vortex Lattice Method in XFLR5	55
5.3	Experimental analysis at the wind tunnel	57
5.4	Aerodynamic coefficients	58
5.4.1	Drag coefficient	58
5.4.2	Lift and moment coefficients	59
5.5	Numerical grid	63
6	Aerodynamic characterization of the UAV	67
6.1	Longitudinal aerodynamic	68
6.1.1	Static stability	68
6.1.2	Background theory of longitudinal control	70
6.1.3	Longitudinal control of the UAV	71
6.2	Lateral aerodynamic	74
6.3	Control derivatives	75
6.3.1	Ailerons deflections	78
6.3.2	Symmetryc deflections	79
6.3.3	Leading edge flaps	81
6.3.4	Rudder deflection	82
7	CAD of the UAV	83
	Conclusions	84
	A Aerodynamic and control derivatives	
	Bibliography	

List of Tables

2.1	Medium-range aircraft geometry [4], [5], [6]	13
2.2	Medium-range aircraft: mean geometric values	13
2.3	UAV's geometry	15
2.4	Tail geometry	16
2.5	Geometry of the control surfaces	19
2.6	UAV's weights distribution	22
2.7	UAV's inertial properties	22
4.1	Low Reynolds number airfoils	38
4.2	UIUC - Aerodynamic coefficients of the Gemini airfoil	40
4.3	Mesh configurations	44
4.4	Angles of attack	44
4.5	Inlet boundary conditions	44
4.6	Outlet boundary conditions	44
4.7	Solver and solution methods	45
4.8	Calculated y^+ - Coarse mesh	47
4.9	Calculated y^+ - Medium mesh	48
4.10	Calculated y^+ - Fine mesh	48
4.11	Airfoil effectiveness	52
5.1	Experimental results	60
5.2	Mesh analyzed	62
5.3	Time elapsed	62
6.1	Results for the two wings	73
6.2	Sideslip derivatives	74
6.3	Derivatives due to ailerons deflections	78
6.4	Derivatives due to symmetry deflections	80
6.5	Derivatives due to rudder deflection	82
A.1	$\alpha = -6^\circ \div 9^\circ$ and $\beta = 0^\circ$	
A.2	$\alpha = -6^\circ \div 9^\circ$ and $\beta = 1^\circ$	
A.3	$\alpha = -6^\circ \div 9^\circ$ and $\beta = 2^\circ$	
A.4	$\alpha = -6^\circ \div 9^\circ$ and $\beta = 3^\circ$	

A.5	$\alpha = -6^\circ \div 9^\circ$ and $\beta = 4^\circ$
A.6	$\alpha = -6^\circ \div 9^\circ$ and $\beta = 5^\circ$
A.7	$\alpha = -6^\circ \div 9^\circ$ and $\beta = 6^\circ$
A.8	$\alpha = -6^\circ \div 9^\circ$ and $\beta = 7^\circ$
A.9	$\alpha = -6^\circ \div 9^\circ$ and $\beta = 8^\circ$
A.10	$\alpha = -6^\circ \div 9^\circ$ and $\beta = 9^\circ$
A.11	$\alpha = -6^\circ \div 9^\circ$ and $\beta = 10^\circ$
A.12	δ_{f1}^f for $\alpha = -6^\circ \div 9^\circ$ and $\beta = 0^\circ$
A.13	δ_{f2}^f for $\alpha = -6^\circ \div 9^\circ$ and $\beta = 0^\circ$
A.14	δ_a^a for $\alpha = -6^\circ \div 9^\circ$ and $\beta = 0^\circ$
A.15	δ_{f1}^a for $\alpha = -6^\circ \div 9^\circ$ and $\beta = 0^\circ$
A.16	δ_{f2}^a for $\alpha = -6^\circ \div 9^\circ$ and $\beta = 0^\circ$
A.17	δ_a^f for $\alpha = -6^\circ \div 9^\circ$ and $\beta = 0^\circ$
A.18	δ_t^e for $\alpha = -6^\circ \div 9^\circ$ and $\beta = 0^\circ$
A.19	δ_t^r for $\alpha = -6^\circ \div 9^\circ$ and $\beta = 0^\circ$
A.20	δ_s^s for $\alpha = -6^\circ \div 9^\circ$ and $\beta = 0^\circ$
A.21	C_y
A.22	C_L
A.23	C_M
A.24	C_l
A.25	C_n

List of Figures

1.1	Flight simulator schematics [2]	3
1.2	Non-linear adaptive Dynamic Control Allocation Autopilot scheme [2]	3
1.3	Freewing Eurofighter Typhoon [2]	5
1.4	Freewing Yak 130 [2]	5
1.5	Hobbyking Bixler3	5
1.6	Experimental flight test: ailerons at 50% [2]	9
1.7	Experimental flight test: ailerons at 0% [2]	9
2.1	Sketch of B737-700 NG	14
2.2	Different types of flap [3]	18
2.3	Top view of the wing	19
2.4	Lateral and front views of the V-Tail	19
2.5	Plane reference system	20
3.1	Flight Reynolds number spectrum [10]	25
3.2	Effectiveness variation with the Reynolds number [11]	26
3.3	Laminar separation bubble [12]	27
3.4	Velocity profile inside the boundary layer [15]	28
3.5	Different wall regions in th turbulent boundary layer [17]	29
3.6	Coupled solver flow chart [23]	37
4.1	Selected airfoils	39
4.2	Geometry of the computational domain	41
4.3	ICEM CFD - Blocking strategy and O-grid around the airfoil	42
4.4	Mesh around the airfoil	43
4.5	Mesh details: leading edge (top) - suction surface (bottom)	43
4.6	Numerical vs experimental results	46
4.7	Root mean square for different mesh	46
4.8	Velocity contour	49
4.9	Velocity vectors on the upper surface	49
4.10	Turbulent kinetic energy	49
4.11	Pressure coefficient	50
4.12	CFD results	51
4.13	Moment coefficient vs α	51

5.1	VLM1 (left) - VLM2 (right) [29]	56
5.2	Wing tunnel schematization	59
5.3	Customized Freewing Eurofighter Typhoon inside the TS n°1	59
5.4	Drag coefficient	60
5.5	Eurofighter model in XFLR5	61
5.6	Distribution $A - RMS(C_K)_{mesh}$	64
5.7	Distribution $B - RMS(C_K)_{mesh}$	64
5.8	Distribution $C - RMS(C_K)_{mesh}$	65
5.9	Distribution A , Mesh 5 - Aerodynamic coefficients	65
5.10	Distribution B , Mesh 5 - Aerodynamic coefficients	65
5.11	Distribution C , Mesh 5 - Aerodynamic coefficients	66
5.12	Mesh 5 - $RMS(C_K)_j$	66
6.1	UAV's reference system	67
6.2	Moment coefficient with respect to angle of attack [30]	68
6.3	Positions of CG and NP	70
6.4	Mesh used in XFLR5 to study the UAV	72
6.5	$C_{M\alpha}$ for the wing made of E343 airfoil	73
6.6	Sideslip angle $\beta > 0$	74
6.7	Control surfaces definition	77
6.8	Positive aileron deflections	77
6.9	Lift distribution: $\delta_{f1}^a > 0$	78
6.10	Elevator: $\delta_t^e > 0$	79
6.11	Positive flap deflections	79
6.12	Lift distribution: $\delta_{f1}^f > 0$	80
6.13	Leading edge flap $\delta_s^s > 0$	81
6.14	Rudder $\delta_t^r > 0$	82
7.1	Render of the UAV	83

Chapter 1

The UCR SkyTeam

The present thesis was developed inside the “The UCR SkyTeam” at the Mechanical Engineering Department of the University of California, Riverside. The Ph.D. candidate Raffaele Baggi has founded this team during his doctoral research project.

The thesis’ goal is to design an unmanned aerial vehicle (UAV) whose geometry is representative of a wide range of civil aircraft (i.e., B737, A220, A320, and E195) to design a flight controller that will operate a vehicle with similar control architecture and geometry of a real size aircraft. The control design process starts by determining the aerodynamic characteristics of the vehicle, including stability and control derivatives, that is the objective of this work. Given the aerodynamic model, it is possible to predict the aircraft’s behavior by creating an ad-hoc flight simulator used for control design. After the closed-loop validation of the autopilot in the simulation environment, the UCR SkyTeam will manufacture the airplane.

This chapter is organized as follows. There is an introduction to the flight control algorithms that will be tested on this new UAV in section one. In section two, the SkyTeam’s equipment is introduced, describing the UAVs and their avionics. At the end of the chapter, the experimental flight tests are explained, giving relevance to the achieved results.

1.1 Introduction to the Non-linear Adaptive Dynamic Control Allocation

During flight, an aircraft can encounter some failures, which are a critical point in modern aviation. A crucial aspect is to maintain aircraft control safely while failure is happening. The failures have different origins: harsh meteorological conditions can cause them, and in that case, the failures are determined by external conditions. Otherwise, something can happen inside the plane’s hardware or software. The last is the case of internal failures.

To overcome possible emergency situations, the aircraft can rely on its flight control architecture that for a classical airliner is divided in primary flight controls (ailerons, elevators and rudder), high-lift devices (flap and slats) and others (airbrakers, thrust reverser etc..). However, even if all these surfaces contribute to the generation of forces and moments, not all of them are actively used by the pilot to steer the aircraft, due to

limitations in current control technologies. Therefore, both software and hardware must be accurately designed to manage aircraft failures, providing a safe and stable flight as long as needed. To reach that goal, it is possible to exploit the control redundancy naturally present on modern aircraft using a Dynamic Control Allocation (DCA) mechanism that automatically redistributes the control commands to the effectors as well as modifies certain reference trajectories to maintain stability of the aircraft under multiple actuator failures [1]. The strength of this novel design lies in the fact that coupling between aerodynamic effectors and body forces are not neglected, and that aerodynamic surfaces can be operated independently. In this way, it is possible to dramatically expand the actuator configurations enabling a specific maneuver. Most importantly, the management of the control redundancy making it possible for the aircraft to respond to a variety of failures by reconfiguring the actuators it already has. If, for example, during a clockwise coordinated turn there is a failure of the right aileron, the autopilot would first allocate most of the control to the left aileron while gradually deflecting the right flap. At steady state, the manoeuvre is performed without degradation of performances (in terms of trajectory tracking) but with a different control configuration. Following the same reasoning, not only flaps, but also slats, airbrakes, thrust vectoring etc. can be used to steer the aircraft if properly managed. The control architecture also includes an adaptive loop for stable tracking of airspeed, flight path, and turn rate reference trajectories in nominal conditions (no actuator failures) to provide robustness to model parameter uncertainty.

To validate the results of this research, the SkyTeam has designed and customized different aircraft models that will be shown in the next section. The customization process involves differential asymmetric deflections of all control surfaces as well as primary flight control system augmentation by adding ad-hoc control effectors, as canards or ruddervators.

Before doing an experimental flight test, there are numerous and complicated steps. The process starts with the creation of physical models of the aircraft. The integration of the controller with the flight computer follows, and after there is the creation of customized sensors. Finally, the Team performs tests to check hardware and software capabilities. At the end of this process, the experimental flight test can be performed.

Considering now the flight simulation and control design aspects, Baggi works on the development of a non-linear 6 DOF flight simulator. In this way, it can support the build-out of guidance, navigation, and control algorithms, manual and automatic flight control systems, as well as the evaluations of handling qualities and control system performances. Figure 1.1 shows the flight simulator structure: the pilot or the flight control system generates the input signals of the controller.

Performing a computational fluid dynamics analysis of the aircraft model geometry allows us to find the aerodynamic coefficients, such as aerodynamic and control derivatives. The integration of forces and moment in the equation of motion follows, and the outputs are the aircraft states. The environmental model makes the simulations more realistic, considering the wind effect. The NASA DRYDEN is used for this purpose.

The starting point for the autopilot design is the aircraft plant, Figure 1.2. The autopilot is made of several parts: Guidance, Navigation, and Control. Every component handles different aspects. More specifically:

- Guidance computes the trajectory that the aircraft has to maintain to track the

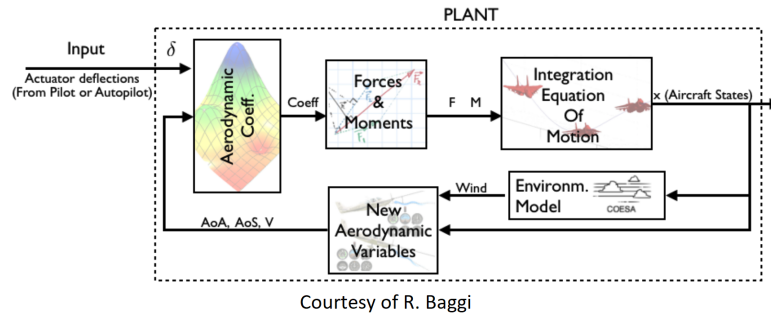


Figure 1.1. Flight simulator schematics [2]

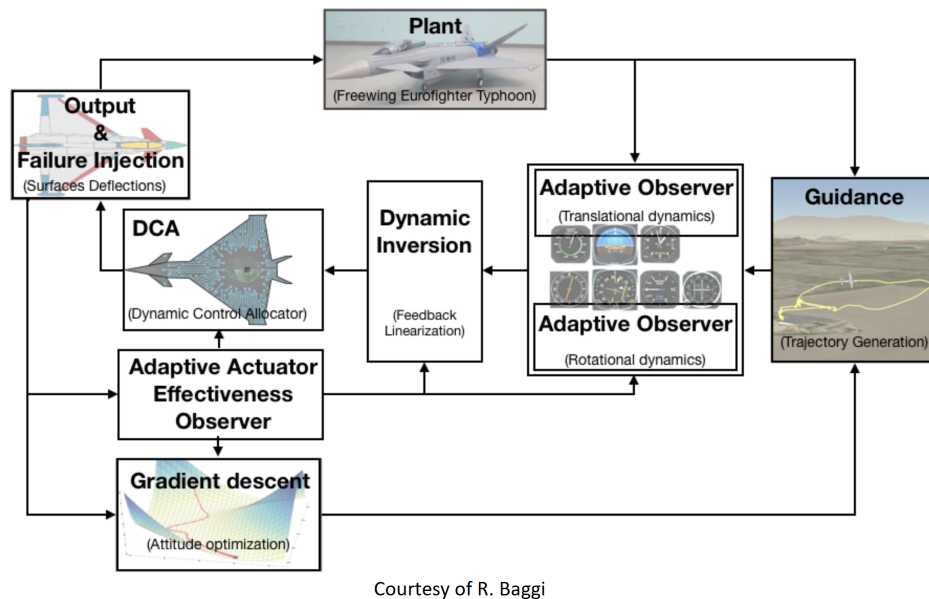


Figure 1.2. Non-linear adaptive Dynamic Control Allocation Autopilot scheme [2]

desired flight path and turn rate. It calculates them, starting from a set of reference signals as flight path and turn rate.

- Navigation determines the vehicle location and velocity at a given time, using a set of instruments, sensors, and algorithms.
- Control is the set of algorithms that create steering controls in order to track the reference signals.

Baggi et al. [1] developed the control algorithm for the UAVs. Its structure is showed in Figure 1.2. The algorithm is robust against actuator failures and uncertainties of model parameters thanks to the Adaptive part of the controller and the Dynamic Control

Allocator (DCA). Looking at the scheme, one can see:

- Two adaptive observers that make the control robust to aerodynamic coefficient uncertainties up to 40%.
- Dynamic Inversion block computes forces and moments to control the aircraft.
- DCA selects a particular combination of surface deflections to generate forces and moments computed by the Dynamic Inversion block. The deflections are estimated by solving simultaneously an optimization problem (gradient descent) using different cost functions.
- Actuator Effectiveness Observer measures the surface deflections. It also estimates forces and moments generated by that deflections. In this way, it is possible to determine if there is a failure in the actuation when comparing the values obtained with the output of the Dynamic Inversion block.
- The DCA automatically distributes the control among all the working actuators left, if there are one or more actuators failures.

1.2 Equipment used by the UCR SkyTeam

During the years of his research activity, the Team has used some different radio-controlled (RC) aircraft available on the market. The group made much customization, especially in the avionics, hardware, optimization, and integration software. That was fundamental to perform simulation and test their new control system.

1.2.1 Radio-controlled aircraft

The UCR SkyTeam’s RC aircraft are:

- Freewing Eurofighter Typhoon: this aircraft has a 90 mm electric brushless ducted fan with 12 blades that produce about 4 kg of thrust. It is possible to apply the thrust vectoring. The wingspan is 0.96 m, the length is 1.4 m, and its weight is about 3.05 kg. It is made of EPS foam. It is a model of a fighter jet, and it can perform acrobatic flights. It has many control surfaces, like the canards, ailerons, and the rudder. The original model has a classic tail configuration, like the real jet. However, the group decided to design a V-Tail to increase the number of control redundancies, as shown in Figure 1.3. The “Malignani SkyTeam”, that is the italian division of the research project, customized the tail. Using the 3D printing they were able to install the two section of the tail.

The aerodynamic performances of this aircraft were investigated at the wind tunnel facility “AeroTunnel - Galleria del Vento” in Gorizia last summer. In this way, the results from the CFD analysis were validated. Unfortunately, this aircraft has still never flown in an experimental test due to the high speed required at the landing. The Team pilot does not have experience with high performances radio-controlled aircraft.



Figure 1.3. Freewing Eurofighter Typhoon [2]



Figure 1.4. Freewing Yak 130 [2]



Figure 1.5. Hobbyking Bixler3

- Freewing Yak 130: it has a 70 mm electric brushless ducted fan similar to the Eurofighter’s one, but its power is about 3 kg, and it cannot do the thrust vectoring. The wingspan is 0.92 m, and the length is 1.05 m. Its original weight was about 1.95 kg, and the EPO foam is employed for the structure. Like the Eurofighter, this plane can do acrobatic flights. The control surfaces are ailerons, elevator, rudder, and flaps. The main feature of this model is the elevator: it is split into two parts, and every one has its servo-control. In this way, the researchers decided to implement the control algorithm to roll the aircraft also using the elevator.

This airplane flew some times, reaching more than 90 mph. In the last test we performed, a problem occurred, and it lost the transmitter signal. In that condition, the pilot could not retake control, and unfortunately, it crashed.

Figure 1.4 shows the aircraft equipped with all the avionics before a flight test: one can see the Pitot tube on the top fuselage, and in the rear part, there are some bolts. They are used to maintain the center of gravity in the right position after that all the avionics is installed on the aircraft changing the original weight distribution. In fact, the new weight is 2.35 kg.

- Hobbyking Bixler3: if compared to the two previous aircraft, it is the low performances UAV of the Team, but at the same time, it is probably more reliable and more comfortable to fly for the Team pilot. The control surfaces on the plane are ailerons, flaps, elevator, and rudder. The research group tested different tails: the commercial configuration with rudder and elevator, and the V-Tail, where the usual control surfaces work as ruddervator. It has a wingspan of 1.55 m, and it does not have an EDF fan, but instead, it employs a propeller. Its top speed is lower than the Yak 130, and also during the cruise, it moves slower than the others. For this reason, if the customized control algorithm does not work, the pilot has enough time to change the control to the factory settings, and land in a safe way.

Figure 1.5 shows the drone just before the take-off during an experimental flight test. In that case, the tail had the conventional configuration. One can see the two cameras mounted on the plane: the one in the rear part, just before the tail, is essential to control the right control surfaces movement during the flight. On the top of the wing the antenna is located. Before the wing, inside the fuselage, all the remaining avionics is located.

1.2.2 Avionics

The different aircraft are equipped with:

- Pixhawk Cube: it is the brain of all the Team’s RC models. It is an open-hardware project that provides low-cost and high-end autopilot. Different versions of the control algorithm were uploaded on it and tested. Its processors are a 32-bit ARM Cortex M45 core, and a 32-bit failsafe coprocessor. The latter works if a problem occurs. It provides many sensors like three redundant Inertial Measurement Units (gyros, compass, and accelerometers). It is interconnected with other avionics, and during the flight, it records all the flight data, so it works like a “black box”. After an experimental flight test, it is possible to extract and analyze all the data.

- Here 2 GPS: it works in communication with the Pixhawk, and it gives him the position of the aircraft with centimeter-level accuracy.
- Readytosky 3DR Radio Telemetry Kit: it provides a telemetry connection between the ground station and the autopilot.
- RFD900+ Telemetry: it provides long-range telemetry. It is ideally designed for Pixhawk applications.
- FrSky Taranis Q X7 2.4 GHz 16CH Transmitter: it is a radio transmitter with sixteen channels. The high number of channels gives the possibility to use additional switches needed to perform the experimental flight tests. The pilot controls the aircraft from the ground with it.
- FrSky Taranis Compatible Receiver X8R 8-Channel: it accesses to all the sixteen channels by using the Sbus line with Sbus supported servers. It also has eight standard servo outputs.
- Pitot tube: used to measure the velocity magnitude. It is mounted in the front of the airplane, and its pressure signal goes to a pressure transducer. Through a particular communication protocol, the data signal goes to the Pixhawk.
- Admiral 2200 mAh 3S 11.1V 35C Lipo Battery: it is characterized by low internal resistance and superior reliability and performance.

1.3 Experimental flight test results

Experimental flight tests are fundamental to evaluate the behavior of the control algorithm in presence of different failures. Both Yak 130 and Bixler3 flew in the experimental flights. However, the second aircraft has been subjected to much more customization and testing. Thanks to its low weight and big wing, it flies at minor speed than the Yak 130, and if something happens, there is enough time to recover the aircraft and land it safely. For these reasons, it is the perfect trainer plane where they can test complex flight control algorithms, without worrying too much about crashing it.

In the course of the flight, the pilot can switch between different fly modes: the “basic” with the factory default settings, the stabilized mode, and the autopilot. When the autopilot mode is enabled, the pilot does not control the aircraft. Baggi developed the stabilized mode and the autopilot in his doctoral research. The tested autopilot acts on the roll, and it is based on:

- A non-linear adaptive control that regulates the roll dynamics.
- A non-linear observer of the roll dynamics which adapts online the aerodynamics effectiveness of both flap and ailerons.

In order to demonstrate that autopilot can control the aircraft roll despite the failures in the primary control surface (ailerons), different failures were injected into the Bixler3

during the experimental flights. The first case scenario was a failure injected into the system, reducing the output of ailerons of 50% and 100%. The adaptive algorithm “feels” that something is not working correctly and automatically deploys flaps to keep the aircraft safe. When the ailerons work at 50% of their extension, the controller moves the flaps. Figure 1.6 shows that situation: on the low left graph, one can see the desired roll angle for the maneuver (blue) and the actual roll angle of the airplane (yellow). They are very close, which means the controller is doing well in his task, moving the flaps to help the aircraft follow the trajectory. Furthermore, the Dynamic Control Allocator controls and maintains safe the vehicle also during the total failure of the ailerons, and the aircraft performs the coordinated turn (Figure 1.7). Finally, this test is significant to show that the autopilot can keep controlling the aircraft automatically using flaps instead of ailerons when a failure in the system occurs.

Later, mechanical failure was simulated. In that instance, the surface is stuck in its neutral position, and the encoders can still read the angular position of the surface, which is fed back to the controller. The test showed that despite the failures in the primary control surface, the autopilot controls the aircraft moving flaps.

Also, an aerodynamic failure was replicated. Eliminating the PWM signal from the ailerons, in such a way that the encoders think that the surface is moving even if it is not. In this case, the adaptive observer identifies the problem and uses flaps to control the aircraft. In this case, the Actuator Effectiveness Observer determines that the commanded deflections are not effective, so the autopilot starts moving the flaps. Also, in this case, the airplane followed the prescribed trajectory.

All these experimental tests demonstrated the reliability of the flight controller based on the non-linear adaptive dynamic control allocation. The dynamic allocator can select the control surfaces to keep the aircraft stable and safe when a failure occurs.

The experimental flight tests indirectly provide trustworthiness about the aerodynamic and control derivatives obtained using XFLR5. This CFD tool was used to perform the aerodynamic characterization of the UAVs in aerodynamic and control derivatives. These aerodynamic coefficients represent one of the control algorithm’s inputs. Experimental tests show that the algorithm works adequately, and it means that the CFD values are correctly estimated. This software will be employed late to calculate the aerodynamic and control derivatives of the new drone.

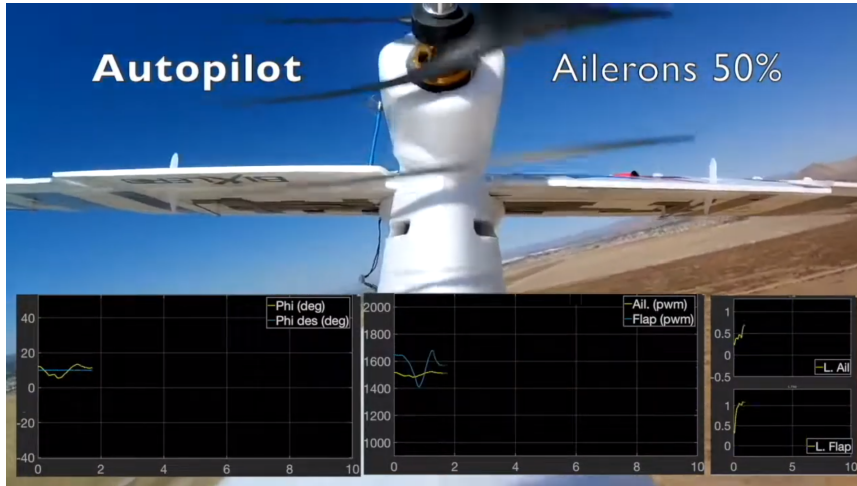


Figure 1.6. Experimental flight test: ailerons at 50% [2]

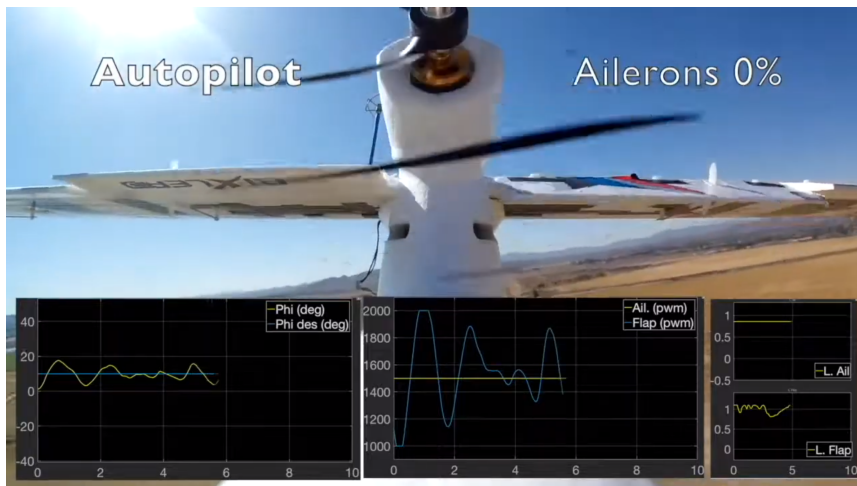


Figure 1.7. Experimental flight test: ailerons at 0% [2]

Chapter 2

Design of the new small UAV

The present chapter is about the design of the new unmanned aerial vehicle (UAV) of the team. The need and the reasons that lead us to decided to conceive a new plane instead of buying one and its repercussions of the development of the new control system are treated in the first section. In the second part, all the requirements are listed and motivated. A preliminary investigation is conducted, knowing all the specifications of the new UAV in the third section. Along the fourth and fifth sections, the geometries of wing and tail are respectively calculated. In the sixth part, the control surfaces are classified and modeled for the new plane. Finally, in the last section, the inertial properties are found.

2.1 Reasons that lead to a new UAV

During the research activity, the Team thought it was helpful to test its new flight control system on an aircraft model with the geometry similar to the civil aircraft's one used for commercial flights all over the World. A possibility was to buy an RC model of a civil aircraft available on the store. On the one hand, it was a more straightforward solution for testing the flight controller on something already built and designed. On the other point of view, it could be challenging to have accurate information about the wing shape and the airfoils distribution. The manufacturers do not provide features about the different sections of the wing, and the 3D scanning was not a chance. If the wing shape is not defined well, the CFD simulation for determining the aerodynamic and control derivatives are not accurate. This uncertainty directly affects the proper functioning of the flight control system because those derivatives are an input of the control algorithm. At the same time, it was challenging to find a model with the desired control surfaces and the wanted ability to work in different ways. This kind of controller expects that a flap can work as an aileron or an aileron as a flap. Finally, the price of this UAV ranges from a few hundred dollars to thousands of dollars.

All these reasons lead us to decide to design a radio-controlled aircraft, whose shape was similar to all the commercial flight used in the continental flights and to test it using an ad-hoc flight simulator. That represents the first step of a control design process. The advantages of this decision are:

- Clear knowledge about the airfoils used for wing and tail, which impact the reliability of the CFD simulations.
- Opportunity to properly design the control surfaces in the required way by the flight controller.
- Possibility to test and customize different configurations without worry about accidents.

2.2 Small UAV requirements

In the preliminary design phase, the Team decided which aircraft category the UAV has to represent. Also, considering a future possibility to build and test it in an experimental flight test, other decisions were taken:

- The UAV geometry, considering wing, fuselage, and wing-tail distance, has to be representative of the civil jet aircraft that works on the medium distance continental flights, ranging from 2000 to 4000 nautical miles.
- The wingspan b_{uav} must be 1.8 m.
- The cruise speed is $V_c = 20$ m/s.
- A single 15% thickness airfoil used along the wingspan, and there is not any twist angle.
- The airplane weight has to be in the range from 3 ÷ 4 kg.
- The actuator lines must be less than sixteen.
- The equilibrium angle of attack must range in $0^\circ < \alpha_{eq} < 3^\circ$ with an elevator deflection contained in $-5^\circ < \delta_{e,eq} < 5^\circ$.

The wingspan choice of 1.8 m is fundamental to guarantee that, under the same conditions of speed, altitude, and high lift devices in nominal condition, the aircraft can fly at minor cruise speed. Indeed, considering the force equilibrium in the vertical direction of a plane flying in cruise, one can find that lift is equal to weight:

$$L = W \implies \frac{1}{2}\rho V^2 S C_L = W \implies V \propto \sqrt{\frac{1}{S}}$$

Increases the wingspan, means an increase in the wing surface so it can fly at a lower speed. The team pilot has already demonstrated to be an excellent pilot of radio-controlled aircraft flying at low-range speed, like the Bixler3. For this reason, we decide to choose the speed of the new drone in the same speed range, to let him be comfortable. Some accidents happened during the Yak flight tests, which has a cruise speed higher than the Bixler. Due to the high speed, it was impossible to restart the system and choose the flight computer's factory settings. Instead, during the Bixler's flight tests, it was possible

to switch to the original firmware to avoid accidents thanks to the slower speed of the aircraft.

However, the selection of the cruise speed has consequences on the airfoil choice for the wing. The chosen range is on the opposite side of the real operating condition of a civil jet airliner. The latest fly at high subsonic flow in the proximity of the transonic region, where the compressibility effects appear, and the airfoils have a shape to contain the wave resistance. Instead, the Team new plane will fly at low speed and elevation, so low to moderate Reynolds and Mach numbers close to zero. Different airfoils designed for this flow condition will be analyzed to guarantee good aerodynamic performances.

The chosen airfoil has to be 15% thick, a technical requirement to use the Bixler3's servo controls again. We decided to select the same servos used on the Bixler to decrease future costs to assembly the drone. Too thin airfoil will not work adequately, limiting the positioning of the servos inside the wing, so they could be used only in a small portion of the wingspan, where the chord is long enough, and the airfoil is sufficiently thick. In fact, due to the wing aspect ratio, the airfoil dimensions along the tip is decreasing. When the chord decreases, the thick drops. If the thickness is less than 15%, the control surfaces should be used only in a small portion of the wing, impeding the installation of the ailerons close to the wingtip.

Assuming a future assembly of the new plane, the Team chose to design a wing with only an airfoil and without twist angle, because that will simplify the construction and building in the future. Also, the Team thought it would be possible to move the avionics from the Bixler3 to the new plane. In this way, the operating costs will be lower than buying new hardware, but at the same time, the total number of channels for commanding the aircraft will be the same as the Bixler3, sixteen. There are still twelve channels if one considers two channels used to control the engines and two other to move the landing gear. Starting from the fuselage and moving to the wingtip, the flight control surfaces are internal flap, external flap, and aileron at the trailing edge. At the leading edge, there is the slat. The single control surface requires one control line. So, considering all the wing, there are still four available channels. In the future, the airbrakes will be studied and developed on the drone requiring two lines free for that purpose. Thus, there are only two available channels to move the servos. The conventional configuration of the tail has a rudder and elevator. The vertical rudder requires one servo. If the horizontal tail employs the same mechanism of the YAK 130, where the two control surfaces may move in a differentially way, three servos are required. This solution is not possible because there are only two command channels available. For solving it, the Team considered designing a V-Tail, which requests only two communication channels. It is made of two fins collocated at 45° respect the horizontal plane, and the effectiveness of its control surfaces, called ruddervators, is the same in every direction.

2.3 Preliminary investigation

Following the first requirement previously imposed, research individuated which airliners are mostly used in the 2000-4000 nautical miles range. Table 1 lists some airplane characteristics like range, wingspan (b), wing surface (S), aspect ratio ($A.R.$), taper ratio (λ),

and sweep angle (Λ) at 25% of the chord. Figure 2.1 clarifies the meaning of L_s and L_{wt} . D_f is the mean fuselage diameter since some aircraft have not perfectly cylindrical. A cylindrical fuselage will ease the construction of the UAV in the future. Finally, it is important to say that the wing surface also includes the surface under the fuselage.

Table 2.1. Medium-range aircraft geometry [4], [5], [6]

Aircraft	Range [NM]	b [m]	S m^2	AR [-]	λ [-]	Λ [°]	L_s [m]	$L_{w,t}$ [m]	D_f [m]
A220-100	2950	35.10	112.30	10.97	-	-	-	-	-
CS300	2950	35.10	112.30	10.97	-	-	-	17.65	-
A318	3080	34.10	112.40	9.50	0.235	25.00	6.67	-	3.96
A319-100	3600	35.80	112.60	9.39	0.240	25.00	6.82	18.86	3.96
A319 neo	3750	35.80	112.30	9.39	0.240	25.00	6.82	-	3.96
A320-200	4000	34.10	122.60	9.48	0.240	25.00	7.07	18.14	3.96
A321-200	4000	34.10	122.60	9.48	0.240	25.00	7.07	20.10	3.96
B737-200	2500	28.35	91.04	8.83	0.266	25.00	4.95	15.75	4.01
B737-300	2270	28.90	91.50	9.17	0.240	25.00	5.07	16.70	3.89
B737-400	2060	28.90	91.50	9.17	0.240	25.00	5.23	18.38	3.89
B737-500	2375	28.90	91.50	9.17	0.240	25.00	5.13	16.67	3.89
B737-600NG	3235	34.32	124.60	9.44	0.278	25.00	4.94	15.87	3.89
B737-700NG	3010	34.32	124.60	9.44	0.278	25.00	4.94	18.20	3.89
B737-800NG	2935	34.32	124.60	9.44	0.278	25.00	4.94	17.33	3.89
B737-900NG	2950	34.32	124.60	9.44	0.280	25.00	4.94	20.26	3.89
B737-MAX7	3800	35.90	127.00	10.15	0.220	25.03	5.13	-	3.89
B737-MAX8	3620	35.90	127.00	10.15	0.220	25.03	5.13	-	3.89
B737-MAX9	3595	35.90	127.00	10.15	0.220	25.03	5.13	-	3.89
E195	2300	28.72	92.53	8.30	0.280	22.60	5.20	15.27	3.18

2.4 UAV wing geometry

Table 2.2. Medium-range aircraft: mean geometric values

\bar{b} [m]	\bar{S} [m ²]	\bar{AR} [-]	$\bar{\lambda}$ [-]	$\bar{\Lambda}$ [°]	\bar{L}_s [m]	\bar{L}_{wt} [m]	\bar{D}_f [m]
33.31	114.47	9.56	0.25	24.86	5.60	17.66	3.86

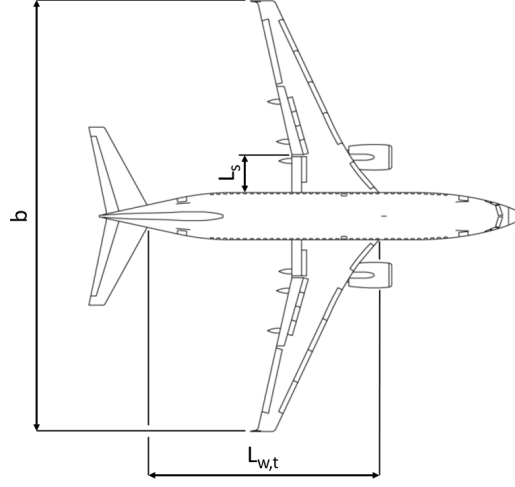


Figure 2.1. Sketch of B737-700 NG

Table 2.2 collects aircraft mean characteristics useful to the UAV sizing process. In particular aspect ratio and taper ratio are defined in this way:

$$AR = \frac{b^2}{S} \quad (2.1)$$

$$\lambda = \frac{c_t}{c_r} \quad (2.2)$$

Where c_t and c_r are respectively the chord at the wing tip and root. Assuming a trapezoidal wing, a half wing surface can be found using the following relationship:

$$\frac{S}{2} = \frac{b(c_r + c_t)}{4} \quad (2.3)$$

Indicating with the subscript uav the generic dimension of the new UAV, its geometric properties may be individuated using some proportions. The segment length at zero sweep angle at the trailing edge of the wing may be calculated using the following relationship:

$$\bar{b} : \bar{L}_s = b_{uav} : L_{s,uav} \quad (2.4)$$

In the same way, for the fuselage diameter applies:

$$\bar{b} : \bar{D}_f = b_{uav} : D_{f,uav} \quad (2.5)$$

Processing the previous relationships, substituting the mean geometric values listed in Table 2.2, you get:

$$S_{uav} = \frac{b_{uav}}{AR} \quad (2.6)$$

$$c_{r,uav} = \frac{2 \cdot S_{uav}}{b_{uav} \cdot (1 + \lambda)} \quad (2.7)$$

$$c_{t,uav} = \bar{\lambda} \cdot c_{r,uav} \quad (2.8)$$

$$L_{s,uav} = \frac{\bar{L}_s \cdot b_{uav}}{\bar{b}} \quad (2.9)$$

$$D_{f,uav} = \frac{\bar{D}_f \cdot b_{uav}}{\bar{b}} \quad (2.10)$$

All the geometric quantities of the UAV are listed in Table 2.3.

Table 2.3. UAV's geometry

b_{uav} [m]	S_{uav} [m ²]	AR_{uav} [-]	λ_{uav} [-]	Λ_{uav} [°]	$c_{r,uav}$ [m]	$c_{t,uav}$ [m]	$L_{s,uav}$ [m]	$D_{f,uav}$ [m]	i_w [°]	L_f [m]
1.80	0.33	9.56	0.25	24.86	0.300	0.075	0.303	0.20	2	1.9

The wing incidence i_w respect the XY -plane of the fuselage (Figure 2.5) is selected at 2°. The fuselage length is 1.9 m. A rectangular shape was designed for the part of the wing that goes under the fuselage, assuming the future UAV manufacturing. This solution will allow an easy assembly of the wing structure to the body. The width is supposed to be 0.1 m from the symmetry plane along each side. It is important to note that the root chord and so the tip chord had been calculated considering a trapezoidal wing. Figure 2.1 shows that the wing is not trapezoidal because there is a segment with zero sweep angle at the trailing edge close to the fuselage. This characteristic is common to all the investigated aircraft. This difference can affect the wing surface. For evaluating that effect, the wing was drawn in Solidworks with the following inputs: b_{uav} , $c_{r,uav}$, $c_{t,uav}$, Λ_{uav} , and $L_{s,uav}$. Using the Solidworks tool, it was possible to evaluate the wing surface with that inputs, which was 0.32 m². The relative difference respect S_{uav} was less than 3%, and for this reason, the wing geometry was not changed.

2.5 UAV V-Tail

Some information about tail geometry, airfoil, and distance wing-tail will be provided. It is essential to consider that this is only a preliminary investigation of the possible tail geometry. Later, other analysis will determine whether the initial guess was right or not, considering the requirements of static longitudinal stability and equilibrium.

The conventional civil airliners investigated earlier have tail made by a vertical fin, whose control surface is the rudder, and a horizontal stabilizer, whose control surface is the elevator. In the V-tail configuration, one can see the twin sections with a specific dihedral angle, without any vertical section. The V-Tail is employed by different aircraft like the Lockheed F-117 Nighthawk and the Beechcraft Bonanza. The control surfaces, also called ruddervators, can work as:

- Equilibrator when the rotation of both surfaces is for positive or negative angles at the same time.
- Rudder when the surfaces move differentially. For example, if the right surface goes down (positive rotation), the left one goes up (negative rotation).

The V-Tail has some advantages, such as reducing the total wetted area and less weight than the conventional configuration because it has fewer parts and components, less interference between empennages and fuselage that means a minimal reduction in drag, and less downwash effect. On the other side, it has some disadvantages. For example, the possibility to encounter the Dutch roll is high, and it transmits more torsional loads on the fuselage to produce the same control force of a conventional tail. Finally, during a yaw rotation, the adverse yaw-roll coupling can manifest.

The airfoil employed for the UAV’s tail is the NACA 0010. It is 10% wide, and it was decided to install the servo outside the structure. Some relations exist to design a V-Tail starting from the standard tail dimensions. Drela [7] developed a method that finds the dihedral angle using the ratio between the vertical and horizontal surfaces. After that, the sum of the vertical and horizontal surface is projected to obtain the fin surfaces. However, this procedure was not followed. Instead, knowing the geometries of some vertical tails of the aircraft already available at the laboratory, we thought their mean value could be used to design an initial guess tail geometry. These values are listed in Table 2.4. Later, during the longitudinal stability study, it will be verified if the tail geometry is right to ensure the UAV stability condition. The same procedure explained previously for the wing (2.4), was used to define the distance between tail and wing along the longitudinal axis. Starting from the following relation:

$$\bar{b} : \overline{L_{wt}} = b_{uav} : L_{wt,uav} \quad (2.11)$$

The distance tail-wing in the UAV is defined:

$$L_{wt,uav} = \frac{\overline{L_{wt}} \cdot b_{uav}}{\bar{b}} \quad (2.12)$$

Finally, the vertical position along the Z -axis was chosen at 0.12 m from the origin. The first guess of the tail geometry is showed in Table 2.4.

Table 2.4. Tail geometry

$c_{r,t}$ [m]	$c_{t,t}$ [m]	b_t [m]	λ_t [-]	Λ_t [°]	$L_{wt,uav}$ [m]	z_t [m]
0.234	0.079	0.248	0.340	44.84	0.954	0.12

2.6 Control surfaces

Controllability represents, along with the stability, a fundamental requirement for a safe flight. The controllability is the process that allows the pilot to change the aircraft flight condition from a first equilibrium condition to a new trimmed condition. The pilot commands the vehicle using the control surfaces and the throttle. An aircraft reaches the equilibrium or trimmed condition when the sum of the forces along every axis is zero, and the sum of the moment about each axis is zero. When the equilibrium condition is affected by any disturbance, if the vehicle is stable, it shows the capacity to return to the original trimmed condition without any pilot command. The stability requirements will be discussed later.

The flight control system depends on the aircraft type considered, but it can be divided into two main groups: primary and secondary control surfaces. When a control surface is deflected, the camber changes, and so the aerodynamic forces vary. Primary surfaces are aileron, elevator, and rudder. They are respectively used for lateral, longitudinal, and directional control, but they also provide lateral, longitudinal, and directional trim [8].

The ailerons are located at the wing trailing edge, and they move in the opposite direction. They are usually installed far from the fuselage to have a sufficient arm to roll the aircraft about the longitudinal axis. For example, the vehicle rolls on the right when the right aileron goes upward, and the left one moves downward. On the right-wing, there is a decrease in lift caused by the camber reduction. Instead, on the left-wing, the camber increases and so the lift too. The lift difference causes the rotation of the vehicle about the X-axis. At the same time, the wing that produces more lift is subjected to more drag. This differential drag is responsible for the adverse yaw, which is more noticeable at low airspeeds.

The elevator is the horizontal control surface of the tail. It acts on the longitudinal movement of the aircraft about the lateral axis, changing the aircraft pitch attitude. A positive deflection of the elevator causes an increase of the horizontal tail camber, so its lift increases. Finally, it produces a negative pitching moment about the Y-axis that moves the nose down. This pitching moment refers to the center of gravity (CG) position, and the distance between CG and tail affects its strength.

The rudder is the movable control surface of the vertical tail, and it controls the aircraft movements about its vertical axis: it is used for directional control. When the rudder is turned into the airflow, a force is produced in the opposite direction. For example, if the rudder moves on the left, the tail moves to the right, yawing the airplane nose to the left.

Secondary surfaces are the high lift devices (flaps and slats), airbrakes, and trim tabs used to improve the performance characteristics of the aircraft. Flaps increase both wing lift coefficient and drag at the take-off and landing. They stay at the inboard of the wing, close to the fuselage, in order to leave more moment arm for the roll control to the aileron. The airbrakes or spoilers are deployed on the top surface of the wing to increase drag and reduce lift. A differential raise of the spoilers allows the control of the roll dynamic on some aircraft. Unlike the ailerons, the differential movement of the airbrakes does not create adverse yaw. However, spoilers will not be studied in this work. Sometimes a control surface that is both primary and secondary. It is the case of the flaperons, which

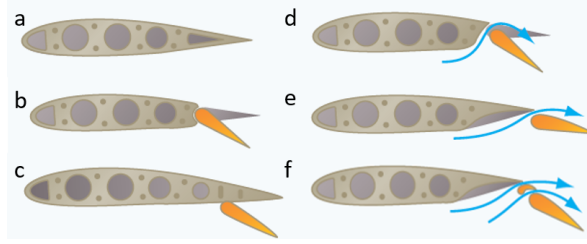


Figure 2.2. Different types of flap [3]

mix flaps and ailerons properties. This solution will be realized in the new UAV. The control algorithm expects that flaps can work as ailerons, and vice-versa.

On the airliners, different mechanisms have been implemented along the time. Figure 2.2 shows some solutions used for the high lift devices at the trailing edge: plain flap (b), split-flap (c), slotted flap (d), fowler flap (e), and slotted fowler flap (f). At the leading edge, slats have been widely implemented. The most common solution consists of moveable segments that can move forward. Considering the future construction of the UAV, in order to ease the wing realization, the solution adopted for flaps and ailerons is the plain mechanism, because it allows the "flaperon behavior." Moreover, it is the cheapest and most straightforward solution in all the different mechanisms: the control surface is hinged at the wing trailing edge. For these reasons, this solution will be used for all the control surfaces, given its advantages.

The control surfaces on the new UAV wing are internal flap, external flap, ailerons, and slat. On the tail, there are the ruddervators. Two classical parameters used in the definition of the high lift devices are the ratios between the chord of the control surface and the chord of the wing, and the ratio of their span. They are:

$$r_1 = \frac{c_s}{c} \quad r_2 = \frac{b_s}{b}$$

The first ratio quantifies how much chord is covered by the control surface. Its typical values are in the interval from 0.17 to 0.35 [8]. The chosen value is 0.20% for the slat, and 0.25% for all other control surfaces of the wing and tail. Instead, b_s/b is the ratio between the control surface length in the Y -axis direction and the semi wingspan. For the ruddervator, the only difference is that b is the semi span of the tail. Table 2.5 shows the control surface geometry. Even if flaps can work as ailerons, and vice-versa, it was decided to follow the standard nomenclature, so instead of calling them like flaperon, their names are internal flap, external flap, and aileron.

Table 2.5. Geometry of the control surfaces

	c_s/c [-]	b_s/b [-]	Max δ_{pos} [°]	Max δ_{neg} [°]
Internal flap	0.25	0.22	+40	-30
External flap	0.25	0.30	+40	-30
Aileron	0.25	0.27	+30	-30
Slat	0.20	0.80	+25	-
Ruddervator	0.25	0.88	+25	-25

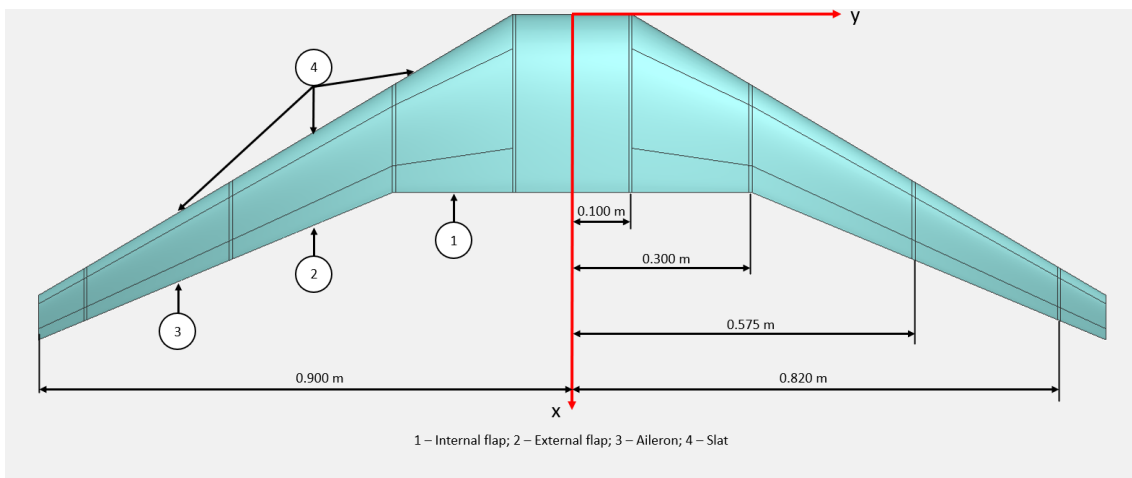


Figure 2.3. Top view of the wing

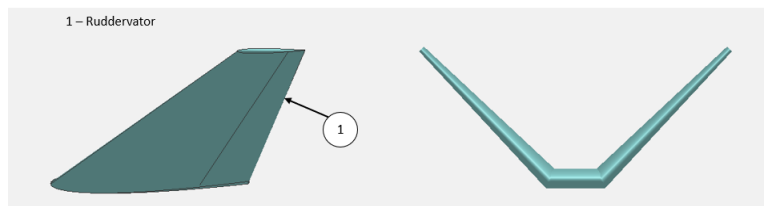


Figure 2.4. Lateral and front views of the V-Tail

2.7 Inertial properties

Knowing the weights of the SkyTeam’s RC aircraft, it was decided to impose a maximum weight for the UAV of around $3 \div 4$ kg. It is essential to know the mass distribution on the body, and so the position of the center of gravity to study the longitudinal stability of the vehicle. Also, the inertial properties influence the UAV flight dynamics, and the control algorithm needs to know these inertial properties to work. In fact, the non-linear

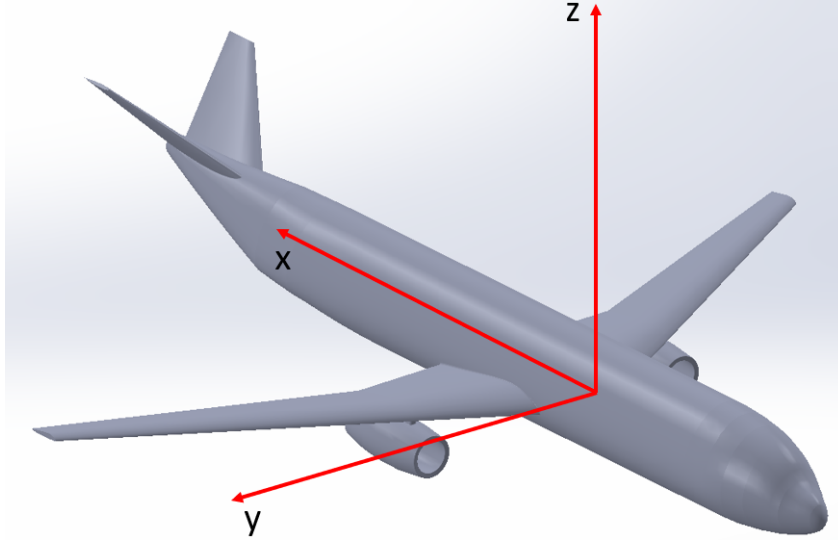


Figure 2.5. Plane reference system

aircraft model is the basis of the control algorithm. In the Flat-Earth model, the 6-DoF Equations in Body axes are [9]:

$$\dot{U} = RV - QW - g_D \sin \theta + (X_A + X_T)/m \quad (2.13)$$

$$\dot{V} = -RU + PW + g_D \sin \phi \cos \theta + (Y_A + Y_T)/m \quad (2.14)$$

$$\dot{W} = QU - PV + g_D \cos \phi \cos \theta + (Z_A + Z_T)/m \quad (2.15)$$

$$\Gamma \dot{P} = J_{xz} [J_x - J_y + J_z] PQ - [J_z (J_z - J_y) + J_{xz}^2] QR + J_z \ell + J_{xz} n \quad (2.16)$$

$$J_y \dot{Q} = (J_z - J_x) PR - J_{xz} (P^2 - R^2) + m \quad (2.17)$$

$$\Gamma \dot{R} = [(J_x - J_y) J_x + J_{xz}^2] PQ - J_{xz} [J_x - J_y + J_z] QR + J_{xz} \ell + J_x n \quad (2.18)$$

Where $[U \ V \ Q]^T$ are the absolute velocity components, $\omega = [P \ Q \ R]^T$ is the angular velocity, $\Phi = [\phi \ \theta \ \psi]^T$ are the Euler angles, g_D is the gravity term in wind axes, $[\ell \ m \ n]^T$ are the aerodynamic moments, $[X_A \ Y_A \ Z_A]^T$ are the components of the aerodynamic forces, $[X_T \ Y_T \ Z_T]^T$ are the thrust force component, and $\Gamma = J_x J_z - J_{xz}^2$.

Unlike the procedures which are followed in the "real size" aircraft design like Torenbeek, in this case, it is not necessary to use an empirical formula to evaluate, for example, the weight of the single element or the UAV weight at the beginning and the end of the flight. There is not any fuel consumption, and so any variation of the weight during the flight. It is not necessary to consider the center of gravity movement and how it affects the stability of the aircraft. Some elements will be moved from the other vehicles, so it was possible to use a scale to check their weights. For other components, web research

provided their weights. The single part position was established considering the fuselage and wing shapes, and the distribution of the weights over the different planes.

The reference system (Figure 2.5) used to define the weight distribution over the aircraft has the origin of the axis coincident with the leading edge of the wing. The X -axis represents the longitudinal axis of the fuselage, and the Y -axis would come out on the right of the hypothetical pilot. The XZ -plane is the symmetrical plane of the aircraft.

The concentrated mass hypothesis is employed to define the center of gravity position and the inertial moments of the airplane. Defining m_i the mass of the element i , and x_i , y_i , z_i its coordinates, the following formula allow the calculation of the center of gravity:

$$X_{cg} = \frac{\sum_{i=1}^n m_i x_i}{\sum_{i=1}^n m_i} \quad (2.19)$$

$$Y_{cg} = \frac{\sum_{i=1}^n m_i y_i}{\sum_{i=1}^n m_i} \quad (2.20)$$

$$Z_{cg} = \frac{\sum_{i=1}^n m_i z_i}{\sum_{i=1}^n m_i} \quad (2.21)$$

When the center of gravity position is determined, it is possible to calculate the inertial moments of the airplane about the baricentric reference system. The used formulas are the following:

$$J_x = \sum_{i=1}^n m_i \left[\left((y_i - Y_{cg})^2 + (z_i - Z_{cg})^2 \right) \right] \quad (2.22)$$

$$J_y = \sum_{i=1}^n m_i \left[\left((x_i - X_{cg})^2 + (z_i - Z_{cg})^2 \right) \right] \quad (2.23)$$

$$J_z = \sum_{i=1}^n m_i \left[\left((x_i - X_{cg})^2 + (y_i - Y_{cg})^2 \right) \right] \quad (2.24)$$

$$J_{xy} = \sum_{i=1}^n m_i \left[(x_i - X_{cg})(y_i - Y_{cg}) \right] \quad (2.25)$$

$$J_{xz} = \sum_{i=1}^n m_i \left[(x_i - X_{cg})(z_i - Z_{cg}) \right] \quad (2.26)$$

$$J_{yz} = \sum_{i=1}^n m_i \left[(y_i - Y_{cg})(z_i - Z_{cg}) \right] \quad (2.27)$$

Table 2.6 shows the weight and the location of each component in the UAV. Table 2.7 reports its inertial properties.

Table 2.6. UAV's weights distribution

Element	Weight [kg]	x_i [m]	y_i [m]	z_i [m]
Wing	0.500	0.20	0	0
Servo internal flap (R)	0.015	0.22	0.20	0
Servo internal flap (L)	0.015	0.22	-0.20	0
Servo external flap (R)	0.015	0.30	0.44	0
Servo external flap (L)	0.015	0.30	-0.44	0
Servo aileron right (R)	0.015	0.42	0.69	0
Servo aileron (R)	0.015	0.42	-0.69	0
Servo slat (L)	0.015	0.25	0.44	0
Servo slat (R)	0.015	0.25	-0.44	0
Nose landing gear	0.050	-0.40	0	-0.10
Main landing gear (R)	0.050	0.45	0.08	-0.10
Main landing gear (L)	0.050	0.45	-0.08	-0.10
Fan (R)	0.216	0.21	0.30	-0.05
Fan (L)	0.216	0.21	-0.30	-0.05
Battery	0.741	-0.23	0	0
Pixhawk	0.076	-0.30	0	0
Front camera	0.100	-0.75	0	0
Rear camera	0.100	0.95	0	0.12
Pitot tube	0.015	-0.60	0	0
ESC	0.064	0.45	0	0
GPS	0.049	0.60	0	0
Telemetry	0.068	0.55	0	0
Radio	0.015	0.70	0	0
Fuselage	0.750	0.19	0	0
Tail	0.350	1.07	0	0.17
Servo tail (R)	0.015	1.10	0.11	0.21
Servo tail (L)	0.015	1.10	-0.11	0.21

Table 2.7. UAV's inertial properties

m_{tot} [kg]	X_{cg} [m]	Y_{cg} [m]	Z_{cg} [m]	J_x [kg · m ²]	J_y [kg · m ²]	J_z [kg · m ²]	J_{xy} [kg · m ²]	J_{xz} [kg · m ²]	J_{yz} [kg · m ²]
3.560	0.205	0	0.012	0.0820	0.6632	0.7152	0	0.0665	0

Chapter 3

Two dimensional aerodynamic

The two dimensional aerodynamic is the object of this chapter. In the first section, the UAV is classified in terms of Mach and Reynolds numbers, comparing them with real-size aircraft. After that, the airfoils aerodynamic is introduced in section three, and the laminar separation bubble is explained in section four since it may manifest itself in the individuated UAV's Reynolds. In the fourth section, the turbulent boundary layer variables are explained because they will be used in the 2D CFD. In the fifth part, starting from the governing equations of the fluid dynamics, the incompressible Navier-Stokes and the Poisson equations are found. In the last paragraph, the numerical solutions of the governing equation are discussed. The RANS model $k - kl - \omega$ employed in ANSYS Fluent is presented, and later a brief discussion about the discretization and the solver is provided.

3.1 Problem identification

Knowing the UAV's geometry, its cruise speed, and the altitude at which it will fly, it is possible to calculate some fundamental fluid dynamics parameters, like Mach and Reynolds numbers. Considering that the pilot steers the UAV from the ground without using any video devices, it can be said the aircraft will fly at low altitudes, and that will be assumed to be under a hundred meters. Thus, the atmospheric data are the following constants:

- $T = 288.15 \text{ K}$
- $p = 101325 \text{ Pa}$
- $\rho = 1.225 \text{ kg/m}^3$
- $\nu = 1.461 \cdot 10^{-5} \text{ m}^2/\text{s}^2$

Other important parameters are the cruise speed and the length scale of the problem. They are respectively:

- $V_c = 20 \text{ m/s}$
- $L = MAC = 0.201 \text{ m}$

The problem's length scale is the mean aerodynamic chord of the wing, which is representative of all the wing since it was decided to consider a wing made of a unique airfoil. With all these data, it is possible to calculate the previously mentioned parameters. The Mach number is the ratio between the speed of an object V to the ambient speed of sound c , and for an ideal gas, it becomes:

$$M = \frac{V}{c} = \frac{V}{\sqrt{\frac{\gamma p}{\rho}}} \quad (3.1)$$

Where gamma is the heat capacity ratio, which is 1.4 for the air in standard condition. Thus, the Mach for the given problem is:

$$M_{uav} = 0.06 \quad (3.2)$$

So the flow is considered incompressible. Instead, for the real-sized aircraft, the cruise Mach number is about 0.75 – 0.85, so the regime is transonic, totally different from the one individuate for the UAV. The compressible effects appear on the wing surface on the suction side at Mach cruise, with a rapidly drag increment. The airfoils have an opportune shape to delay the compressible effects like the shock waves. The supercritical airfoils are usually employed in this flow regime because they can retard the Mach drag rise. Considering now the Reynolds number, it is defined as it follows:

$$Re = \frac{\rho V L}{\mu} = \frac{V L}{\nu} \quad (3.3)$$

This parameter governs the fluid dynamic of viscous flows and quantifies the relative importance of the inertial forces (fluid momentum) compared to the viscous effects. According to its values, the fluid flow can be laminar, transitional, or turbulent. Considering the Reynolds of the UAV, the value is:

$$Re_{uav} = 2.88 \cdot 10^5 \quad (3.4)$$

The founded value falls in the numerical set of model airplanes, as Figure 3.1 shows. It also shows a vast scale range, where Reynolds starts at 10^2 for the insects and increases more than 10^9 for the large water-immersed vehicle. Looking at that graph, it is visible that the aerodynamic of the UAV will be different from the aerodynamic of the jet transports, which operate at Reynolds numbers spanning from 10^7 to more than 10^8 . This difference means that the aerodynamic design of UAV must consider the different fluid dynamics phenomena that occur. It cannot only be scaled down from larger airplanes, but instead, the shape of the airfoil depends on the size and the speed of the aircraft. This dependency is known as scale effect [10].

3.2 Fundamental of airfoil aerodynamics

An airfoil is a section of the wing that can be obtained by cutting a plane parallel to the wing's symmetry plane. Airfoils data are often called infinite wing data, that are

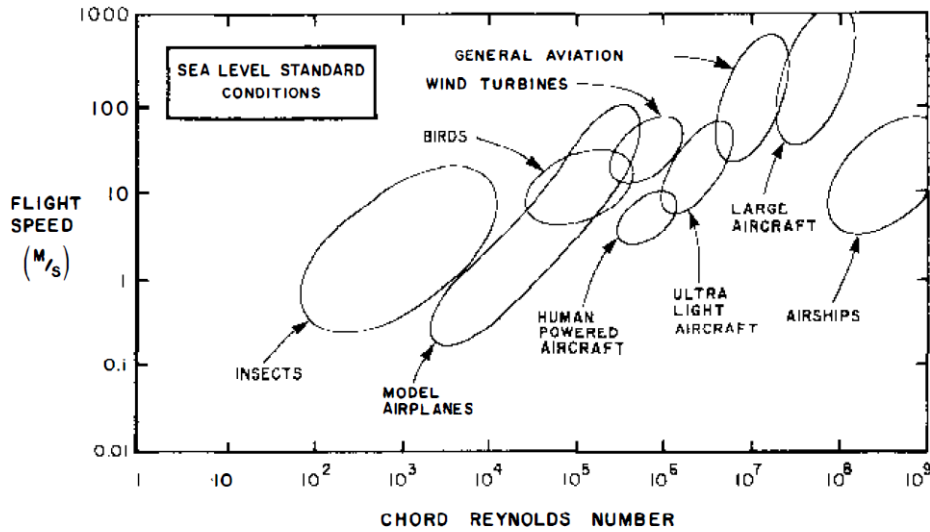


Figure 3.1. Flight Reynolds number spectrum [10]

somewhat different from those of a finite wing. When an airfoil is immersed in a fluid flow, the boundary layer rises on the airfoil surface. In that thin-wall region, the viscous effects are dominant over the inertial ones. The fluid speed at the wall is zero, and this condition is usually known as no-slip condition. Along the perpendicular direction of the wall, the speed increases reaching the undisturbed speed flow at some distance from the wall, usually indicated with δ . The boundary layer thickness δ depends on the Reynolds number, and so on, the x coordinate on the airfoil. Conventionally, the end of the boundary layer in the perpendicular direction is located where the speed reaches 99% of the external speed.

The Reynolds number directly affects the envelope of the fluid inside the boundary layer. If the Reynolds number is less than the critical value, the fluid flow over the airfoil is laminar at the beginning, followed by a transitional region where the disturbances arise. Then, there is the turbulent region. The transitional region starts in correspondence of the coordinate where the critical Reynolds number is reached. For a flat plate, the theoretical value is $5.0 \cdot 10^5$, but the experimental value ranges in between $3.5 \cdot 10^5 \div 10^6$. The difference is due to the multiplicity of factors that affect the transition, like the wall rugosity, free stream turbulence, vibrations of the body, and others. Instead, if the Reynolds number is higher than the critical Reynolds, the fluid flow is entirely turbulent inside the boundary layer.

Considering an airfoil at AoA different from the zero-lift angle of attack, the surface with a lower pressure can be individuated. That is called suction surface, and the flow reaches a condition for which the relative pressure is negative, so the local pressure on the surface is less than the far-field static pressure. The suction peak corresponds to the minimum pressure coefficient, and so to the maximum fluid speed over the airfoil. After that, the flow encounters an adverse pressure ratio, and the pressure recovers to a higher value, less to the far-field static pressure because there are viscous effects. However,

considering the speed profile, when the velocity components parallel to the wall manifests a vertical tangent, so $dU/dx = 0$, the separation occurs.

When a fluid flow invests an airfoil, a pressure distribution acts along the normal direction to the wall and frictional effects in the parallel direction of the surface. The integration of these effects over the airfoil surface provides the total aerodynamic force, which can be projected along the normal and parallel direction to the flow speed, providing lift and drag. Some coefficients are used to analyze the performance of the airfoils:

$$C_l = \frac{L}{qc} \quad C_d = \frac{D}{qc} \quad C_m = \frac{M}{qc^2} \quad (3.5)$$

In the equation (3.5), $q = 0.5\rho V^2$ represents the dynamic pressure of the flow and c is the chord.

3.3 Laminar separation bubble

The airfoil choice is taken considering that its goal is to produce lift with the lowest drag possible to reduce the consumption. A classical parameter used to choose the airfoil is the lift-to-drag ratio, and its maximum value indicates the airfoil effectiveness [10]:

$$E = \frac{C_l}{C_d} \quad (3.6)$$

The Reynolds number affects airfoil effectiveness since the coefficients are dependent on the Reynolds itself. Figure 3.2 shows the trend. The UAV's wing works at Reynolds

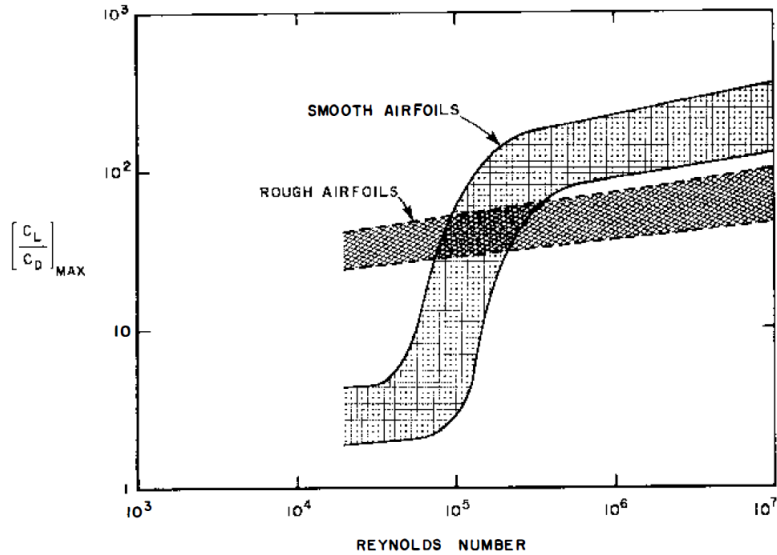


Figure 3.2. Effectiveness variation with the Reynolds number [11]

of about $3 \cdot 10^5$, with different aerodynamics than the one of the real-size aircraft. The distinction stands in the different amplitude of the inertial and viscous effects:

- High Reynolds, more than 10^6 : the flow in the boundary layer encounters the onset of the adverse pressure gradient after the transition from laminar to turbulent. Otherwise, the transition takes place right after the suction peak.
- Lower Reynolds number range: at the onset of the adverse pressure gradient, the flow may still be laminar.

At high Reynolds, the turbulent layer can face the adverse pressure gradient better than laminar, because it has a higher quantity of kinetic energy than the laminar case. So the separation from the airfoil is delayed. At lower values, the laminar layer has not yet been manifested to the transition when the pressure recovery starts. At small angles of attack, the adverse pressure gradient is gentle, but as soon as the AoA increases, it becomes more intense, and so laminar separation happens. This flow phenomenon is three-dimensional in practical situations, and the separation zone is more complicated than the 2D representation. However, the 2D schematization helps understand the basic principles of the laminar separation bubble (LSB). Figure 3.3 shows the flow field close

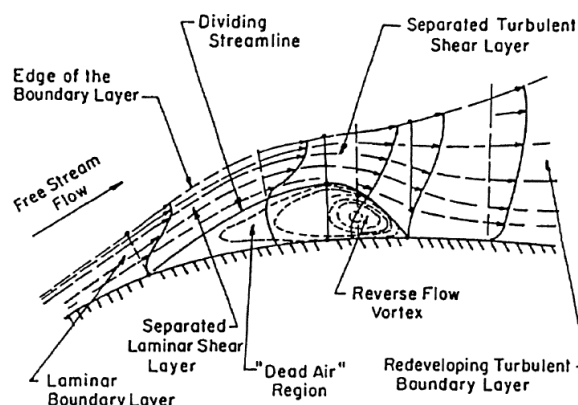


Figure 3.3. Laminar separation bubble [12]

to the laminar separation bubble. When the laminar boundary layer tears away from the airfoil surface, it moves at almost constant separation angle, rising from the surface. The separated boundary layer then mixes with the freestream, generating a shear layer characterized by high instability. This instability may lead to the transition to turbulent, and if it happens close enough to the separation point, it will lead the boundary layer to re-attach to the surface. When the transition occurs, the dividing streamline quickly re-attaches to the wall. Under that streamline, the reversed flow region is divided into two more regions. Very close to the separation point, there is the "dead-air-region" where fluid moves very slowly. Moving down the center of the reverse flow vortex is located, which moves faster than the first region, and it lies near the reattachment point. The wall pressure stays constant within the separated region near the separation point, while a sharp pressure gradient matches the vortex region close to the reattachment point [13].

Different laminar bubbles arise, and their size depends on the airfoil shape and its Reynolds. The LSB can be divided into short and long bubble:

- The short bubble typically manifests at Reynolds higher than $3 \cdot 10^5$, and it covers a few percent of the airfoil chord. It does not cause relevant alteration of the pressure, and it can be considered as the transition-forcing mechanism from laminar to turbulent. However, when the angle of attack increases, the short bubble increases its size. When the adverse pressure gradient becomes strong enough, a periodic shedding starts from the separation [13]
- At lower Reynolds, the long bubble is located on the airfoil. In the Reynolds range from $0.7 \cdot 10^5 \div 2 \cdot 10^5$, the laminar separation bubble covers up to 20/30%, changing the curvature of the external flow. In particular, when the angle of attack increases, the bubble moves close to the leading edge, and so the camber is increased, and the airfoil produces more lift than the expected value [14].

All these aspects directly affect the design and the studies for low to moderate Reynolds airfoils.

3.4 Turbulent boundary layer

The turbulent boundary layer over the reattachment reorganizes itself to form an approximately standard turbulent profile. The difference between laminar and turbulent boundary layer is evident in the speed profile along the normal direction to the surface (Figure 3.4), which leads to different viscous wall stresses. In the case of the turbulent boundary layer, the gradient velocity at the wall is more significant than the laminar case, so the shear stress is larger. Furthermore, the turbulent profile has more kinetic energy on average close to the wall than the laminar case, which allows the flow to contrast higher adverse pressure gradient, delaying the boundary layer separation.

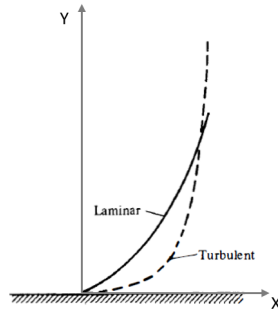


Figure 3.4. Velocity profile inside the boundary layer [15]

Considering a two-dimensional case, the total shear stress $\tau(y)$ is the sum of the viscous stress and the Reynolds stress [16]:

$$\tau(y) = \mu \frac{d\bar{U}}{dy} - \rho \overline{u'v'} \quad (3.7)$$

Where \bar{U} is the characteristic speed of the fluid, u' and v' are the turbulent fluctuations. At the wall, the no-slip condition is verified, and so the Reynolds stresses are zero. Then, the wall shear stress is caused totally from the viscous contribution:

$$\tau_w \equiv \mu \left(\frac{d\bar{U}}{dy} \right)_{y=0} \quad (3.8)$$

Thus, the viscous stress dominates at the wall and with the viscosity, they are influential parameters. These quantities are useful to define appropriate velocity and length scales to describe the near-wall region. They are the friction velocity u_τ and the viscous lengthscale δ_ν , which are expressed by the following relationships:

$$u_\tau = \sqrt{\frac{\tau_w}{\rho}} \quad (3.9)$$

$$\delta_\nu = \nu \sqrt{\frac{\rho}{\tau_w}} = \frac{\nu}{u_\tau} \quad (3.10)$$

Finally, the distance from the wall is measured using the wall units:

$$y^+ = \frac{y}{\delta_\nu} = \frac{u_\tau y}{\nu} \quad (3.11)$$

Using the y^+ , it is possible to identify the region of the inner turbulent layer (Figure 3.5). Its value is essential to correctly solve a turbulence model during the computational fluid dynamics analysis. Each model requires a different value of y^+ , so its choice will be fundamental to correctly solve the boundary layer.

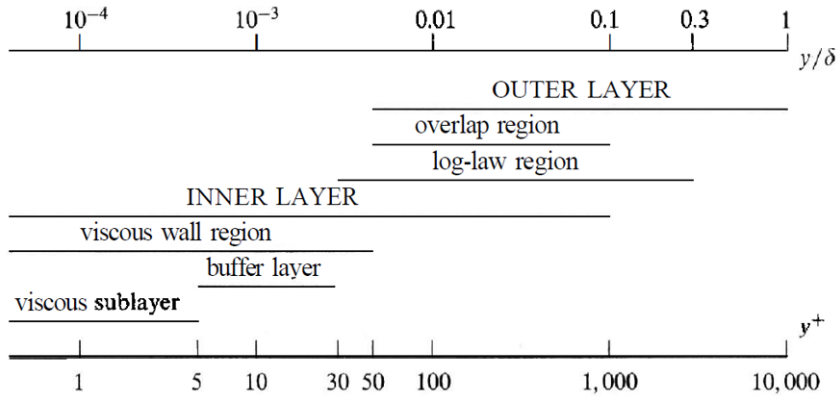


Figure 3.5. Different wall regions in th turbulent boundary layer [17]

3.5 Governing equations of fluid dynamics

The fundamental governing equations of fluid dynamics are the mathematical statements of three fundamental physical principles. They are:

1. Mass is conserved.
2. Newton's second law: $\vec{F} = m \cdot a$.
3. Energy is conserved.

Consider now the following assumptions:

- The Knudsen number has to be:

$$Kn = \frac{\lambda}{L} \ll 1$$

It represents the ratio of the molecular mean free path length to a representative length scale of the problem. When it is much less than one it means that the fluid is considered as a continuum.

- The chemical composition is constant, so the fluid is not chemically reacting.
- The fluid is Newtonian. It implies a linear relation between the stress tensor and the symmetric part of the deformation tensor. The mathematical relation in the compact form is the following:

$$\tau_{ij} = \mu \left(\frac{\partial u_i}{\partial x_j} + \frac{\partial u_j}{\partial x_i} \right) + \lambda \frac{\partial u_k}{\partial x_k} \delta_{ij}$$

Where δ_{ij} is the Kronecker's delta:

$$\delta_{ij} = \begin{cases} 0, & \text{if } i \neq j \\ 1, & \text{if } i = j \end{cases}$$

- It is assumed the Stokes' hypothesis, which relates the bulk viscosity (λ) and the dynamic viscosity (μ). They are also known as the first and second coefficient of viscosity. The relation is:

$$\lambda + \frac{2}{3}\mu = 0$$

- The fluid follows the Fourier' Law, which means the conduction part of the heat flux vector is linearly dependent on the temperature gradient:

$$q_i = -k \frac{\partial T}{\partial x_i}$$

Where k is the thermal conductivity.

- The radiation is neglected.
- The body forces are neglected.

Under the previously hypotheses, the governing equations of fluid dynamics are continuity (3.12), momentum (3.13), and energy equation (3.14). They describe in general an unsteady, compressible, viscous, and three-dimensional flow. The momentum equations are usually called as Navier-Stokes equations. They are:

$$\frac{\partial \rho}{\partial t} + \frac{\partial(\rho u_j)}{\partial x_j} = 0 \quad (3.12)$$

$$\frac{\partial(\rho u_i)}{\partial t} + \frac{\partial(\rho u_i u_j)}{\partial x_j} + \frac{\partial p}{\partial x_i} - \frac{\partial \tau_{ij}}{\partial x_j} = 0 \quad (3.13)$$

$$\frac{\partial(\rho E)}{\partial t} + \frac{\partial(\rho H u_j)}{\partial x_j} - \frac{\partial(\tau_{ij} u_i)}{\partial x_j} + \frac{\partial(q_j)}{\partial x_j} = 0 \quad (3.14)$$

In the governing equations of fluid dynamics, ρ is the flow density, $\vec{V} = (u, v, w)$, p is the static pressure, τ_{ij} is the stress tensor, E is the total energy given by the sum of the internal and kinetic energy, and H is the total enthalpy which is:

$$H = e + \frac{p}{\rho} + \frac{u_i^2}{2} \quad (3.15)$$

However, there are five equations total: two scalar equations (3.12), (3.14) and the momentum balance (3.13) that is projected in the three directions of the reference system. Counting the unknowns in the equations, they are seven, so two more than the equations available. It is necessary to use two more relation to close the system. The first equation is the perfect law gas. The relation (3.15) is the link for the thermodynamics variables, which implies that the specific heats are constant.

The calculated Mach number for the UAV is 0.06. When the Mach is less than 0.3, the flow is considered as incompressible, which means the density does not change in space and time. In this case, the energy equation is decoupled from the others. The equation (3.12) and (3.13) become in the differential form:

$$\frac{\partial u_i}{\partial x_i} = 0 \quad (3.16)$$

$$\frac{\partial u_i}{\partial t} + u_j \frac{\partial u_i}{\partial x_j} = -\frac{1}{\rho} \frac{\partial p}{\partial x_i} + \nu \frac{\partial^2 u_i}{\partial x_j \partial x_j} \quad (3.17)$$

The equation (3.16) shows that the velocity field is solenoidal in case of incompressible flow. The system of equations, (3.16) and (3.17), is defined as self-contained, and there are four equations for the four dependent variables u, v, w , and p . The continuity and momentum equations are the only ones necessary to solve the problem. The assumption of incompressible flow, where ρ is constant in space and in time, makes the energy equation

completely decoupled from the analysis. If the heat transfer is involved, the energy equation can be used to calculate the temperature field, after that the velocity and pressure fields are obtained. Moreover, the pressure ends up being a thermodynamic parameter, but its evolution is such that the velocity field is solenoidal. Applying the divergence to the momentum equation and using the continuity condition, it obtains the Poisson equation for the pressure. In the vectorial form it is:

$$\nabla^2 p + \rho \left[(\vec{V} \cdot \nabla u)_x + (\vec{V} \cdot \nabla v)_y + (\vec{V} \cdot \nabla w)_z \right] = 0 \quad (3.18)$$

Finally, the incompressible problem is described by the Navier-Stokes equations (momentum balance) and the Poisson equation for the pressure. The velocity field is two dimensional for the airfoils, and so the system of equation is made of 3 equations for 3 unknowns: u , v , and p .

3.6 Numerical solution of the Navier-Stokes equations

3.6.1 State of art: different computational tools

Computational fluid dynamics (CFD) develops algorithms and solvers to study and simulate fluids flow. However, nowadays, no one has solved and found a general solution in closed form for the equations system (3.12),(3.13), (3.14), but different numerical methods exist. The most computationally expensive numerical tool is the Direct Numerical Simulation (DNS), which does not use any approximations and solves all the motion scales. When the Reynolds number increases, the computer requirements increases also. Due to the high computationally cost, this tool is not a standard in engineering design. However, researchers widely use it because it allows numerical experiments that are difficult to realize in a laboratory. Another tool is the Large Eddy Simulation (LES), which considers only the spatial and temporal scale larger than a limit value. The flow quantities are decomposed into small and large scale contribution by a spatial filter. So, the large scales' contributions are explicitly calculated, and the effects of the small scale on the large one are described using a model. For example, the flow velocity $u_i(\vec{x}, t)$ is decomposed into the sum of a resolved component $\hat{U}(\vec{x}, t)$ and a subgrid-scale component $u'_i(\vec{x}, t)$:

$$u_i(\vec{x}, t) = \hat{U}(\vec{x}, t) + u'_i(\vec{x}, t)$$

The use of filter reduces the computationally cost, which is lower than the DNS. Finally, the most used numerical tool in the industrial sector is the RANS model. They provide reliable results at the lowest computational time compared to the DNS and LES [18]. RANS means Reynolds Averaged Navier-Stokes. They are based on Reynolds decomposition, which expects a instant value can be decomposed in a sum of the mean (time-averaged) and fluctuating value.

3.6.2 RANS $k - \epsilon - \omega$ model

Because of their limited computational requests, RANS methods are the more efficient and feasible CFD simulation tool for engineering applications involving the laminar separation

bubble [19]. In the RANS decomposition, velocity and pressure are:

$$u_i(\vec{x}, t) = \overline{U}_i(\vec{x}) + u'_i(\vec{x}, t) \quad (3.19)$$

$$p_i(\vec{x}, t) = \overline{P}(\vec{x}) + p'(\vec{x}, t) \quad (3.20)$$

Substituting (3.19) and (3.20) in the continuity (3.16) and Navier-Stokes (3.17) equations, they are:

$$\frac{\partial U_i}{\partial x_i} = 0 \quad (3.21)$$

$$\frac{\partial U_i}{\partial t} + U_j \frac{\partial U_i}{\partial x_j} = -\frac{1}{\rho} \frac{\partial P}{\partial x_i} + \nu \frac{\partial^2 U_i}{\partial x_j \partial x_j} - \frac{\partial \overline{u'_i u'_j}}{\partial x_j} \quad (3.22)$$

The equation (3.22) is called Reynolds equations, and the term $-\rho \overline{u'_i u'_j}$ is the Reynolds stress tensor. It is usually interpreted as turbulent stress, so it represents the mean flux of momentum caused by the turbulent fluctuations, but it is a consequence of the averaging process. This tensor is symmetric, and so it introduces six more unknowns. The most common methods to close the problem are based on the Turbulent Viscosity Hypothesis (TVH) proposed by Boussinesq in 1877. It is a linear relationship between the Reynolds stress tensor and the strain rate tensor:

$$\overline{\rho u'_i u'_j} - \frac{1}{3} \overline{\rho u'_k u'_k} \delta_{ij} = -2\mu_t \overline{S_{ij}} \quad (3.23)$$

Through this assumption, the Reynolds equations have the same form of the Navier-Stokes equations. The TVH relationship implies that the anisotropy tensor of the Reynolds stresses is aligned with the strain rate tensor. This assumption does not have general validity, and, specifically, the TVH theory is not valid when the flow has strong swirl or significant curvature. The eddy viscosity is a flow property ($\mu_t = \mu_t(\vec{x}, t)$), and all the effects of the fluctuating velocity field are modeled with it. It is necessary to evaluate the eddy viscosity to close the Reynolds equations. Over the years, different models were developed like the Spalart–Allmaras, the $k - \epsilon$, and the $k - \omega$. However, these widely used turbulence models expect a fully turbulent flow over a body, and they were not designed to predict transition. Therefore, the transitional results founded with those models should not be expected to agree with the real transition process [20]. For these reasons, the fully turbulent models are not recommended for study low Reynolds numbers where the flowfield can be laminar or transitional, but a transitional model is recommended. Modeling the transition improves the accuracy of the solution for low and moderate Reynolds numbers if compared to a fully turbulent model [21].

The transitional model implemented in ANSYS Fluent is the $k - kl - \omega$ developed by D.K. Walters and D. Cokljat [22]. The basis of this model is the two-equation low-Reynolds $k - \omega$ shear stress transition (*SST*) eddy viscosity model, where two equations model the turbulent kinetic energy and the specific dissipation rate. Instead, the transitional model has one more transport equation for representing the pretransitional velocity fluctuations, which trigger the transition in the boundary layer. Thus, the model transport equations

are solved for the turbulent kinetic energy k_T , the laminar kinetic energy k_L , associated to the pre-transitional fluctuations, and the scale-determining variable ω :

$$\begin{aligned} \frac{Dk_T}{Dt} = & \underbrace{P_{k_T}}_{\text{production}} + \underbrace{(R_{BP} + R_{NAT})}_{\text{bypass and natural transition}} - \underbrace{\omega k_T}_{\text{destruction}} - \underbrace{D_T}_{\text{anisotropic dissipation}} + \\ & \underbrace{\frac{\partial}{\partial x_j} \left[\left(\nu + \frac{\alpha_T}{\sigma_k} \right) \frac{\partial k_T}{\partial x_j} \right]}_{\text{diffusion}} \end{aligned} \quad (3.24)$$

$$\frac{Dk_L}{Dt} = \underbrace{P_{k_L}}_{\text{production}} - \underbrace{(R_{BP} + R_{NAT})}_{\text{bypass and natural transition}} - \underbrace{D_L}_{\text{anisotropic dissipation}} + \underbrace{\frac{\partial}{\partial x_j} \left[\nu \frac{\partial k_L}{\partial x_j} \right]}_{\text{diffusion}} \quad (3.25)$$

$$\begin{aligned} \frac{D\omega}{Dt} = & \underbrace{C_{\omega 1} \frac{\omega}{K_T} P_{k_T}}_{\text{production}} + \underbrace{\left(\frac{C_{\omega R}}{f_w} - 1 \right) \frac{\omega}{k_T} (R_{PB} + R_{NAT})}_{\text{bypass and natural transition}} - \underbrace{C_{\omega 2} \omega^2}_{\text{destruction}} + \\ & + \underbrace{C_{\omega 3} f_w \alpha_T f_w^2 \frac{\sqrt{k_T}}{d^3}}_{\text{boundary layer wake correction}} + \underbrace{\frac{\partial}{\partial x_j} \left[\left(\nu + \frac{\alpha_T}{\sigma_\omega} \right) \frac{\partial \omega}{\partial x_j} \right]}_{\text{diffusion}} \end{aligned} \quad (3.26)$$

The total fluctuation kinetic energy is given by the sum:

$$k_{TOT} = k_L + k_T \quad (3.27)$$

The inverse turbulent time-scale ω is a function of the isotropic dissipation ε . In particular, it is:

$$\omega = \frac{\varepsilon}{k_T} \quad (3.28)$$

The boundary conditions are:

- At solid boundaries the no-slip condition is applied, which means:

$$k_L = k_T = 0$$

- A zero-normal-gradient is used for ω . Using η for the wall-normal direction:

$$\frac{\partial \omega}{\partial \eta} = 0$$

This model adopts an approach similar to other low Reynolds models, where increased viscous dissipation in the sublayer is incorporated in k_L and k_T .

- At flow inlets, the turbulent kinetic energy is determined using the turbulent intensity factor with the assumption of isotropic freestream turbulence.

$$Tu_\infty = \frac{\sqrt{\frac{2}{3} k_T}}{U_\infty}$$

- If the velocity inlets is far away from a solid wall, the flow at the inlet is totally outside of the boundary layer. In that case:

$$k_L = 0$$

3.6.3 Discretization

ANSYS Fluent solves the governing integral equations of the fluid dynamics implementing a finite volume solver. The control-volume-based technique works in this way:

- Division of the fluid domain into discrete control volumes.
- Discretization of the governing equations on the discrete volumes to develop algebraic equations for the discrete variables.
- Linearization of the discretized equations.
- The solution of the resulting linear equation system yields to updated values of the unknowns.

Considering a general scalar quantity ϕ , the three-dimensional transport equation in the integral form is:

$$\int_{\Omega} \frac{\partial(\rho\phi)}{\partial t} d\Omega + \int_S \rho\phi\vec{V} \cdot \vec{n}dS - \int_S \Gamma\nabla\phi \cdot \vec{n}dS = 0 \quad (3.29)$$

Where Ω is the cell volume, S is the face surface, ρ is the density, $\vec{V} = u\hat{i} + v\hat{j} + z\hat{k}$, \vec{n} is the normal vector to the surface, and Γ is the diffusion coefficient for the scalar quantity ϕ . The software stores discrete values of a scalar at the cell center, but the face values are required to solve the convection terms. They are interpolated starting from the cell center values using an upwind scheme, which may be first-order, second-order, power law, and QUICK. Instead, the diffusion terms are central-differenced and are second-order accurate. Equation (3.29) is applied to every control volume in the computational domain, and on a given element, it is discretized in this way:

$$\frac{\partial(\rho\phi)}{\partial t}\Omega + \sum_{k=1}^{N_{faces}} (\rho\phi\vec{V} \cdot \vec{n}S)_k - \sum_{k=1}^{N_{faces}} (\Gamma_{\phi}\nabla\phi \cdot \vec{n}S)_k = 0 \quad (3.30)$$

In the equations (3.29) and (3.30), the different elements are, respectively, unsteady, convective, and diffusive terms. The unsteady term appears when a transient simulation is analyzed, and temporal discretization involves the integration of every element of the differential equations over a time step. The time integration can be done using an implicit or an explicit formulation.

During the simulations, the second-order upwind scheme was used, and the different quantities at cell faces are calculated using a linear reconstruction approach. This approach allows reaching a higher-order accuracy at cell faces using a Taylor series expansion of the

cell-centered solution about the cell centroid. The face value of the scalar ϕ_s is calculated in this way:

$$\phi_s = \phi + \nabla\phi \cdot \vec{r} \quad (3.31)$$

Where ϕ and $\nabla\phi$ are the value and its gradient in the upstream cell, and \vec{r} is the displacement vector from the upstream cell centroid to the face centroid. To use the formulation (3.31), the gradients $\nabla\phi$ are needed in every cell. ANSYS Fluent provides different methods to calculate them: Green-Gauss Cell-Based, Green-Gauss Node-Based, and Least Squares Cell-Based. In the airfoils simulations, the gradients were calculated using the Least Squares Cell-Based because it is the less computationally expensive method.

The software offers different slope limiters, but everyone works to prevent spurious oscillations, which would appear in the solution. The limiter works to ensure the monotonicity of the solution, forbidden to the reconstructed linear variable on the cell faces to exceed the minimum or the maximum values of the neighboring cells.

3.6.4 Solver

Fluent implements two different numerical methods:

- The pressure-based solver for low-speed incompressible flows.
- The density-based solver mostly used for high-speed compressible flows.

However, considering the given problem, where the flow is incompressible, we will focus on the pressure-based solver. As shown previously in the section (3.4), the governing equations are the Navier-Stokes and the Poisson equation for the pressure. The pressure ends up being a thermodynamic parameter. Its evolution follows a way that the velocity field respects the solenoidal condition. The governing equations are non-linear and coupled to one another. Thus, the solving process requires iterations until the convergence is reached.

In ANSYS Fluent [23], two different pressure-based solvers are available: coupled and segregated. The main difference is that the coupled is an efficient single-step implementation, where momentum and pressure-based continuity equations are solved simultaneously. Instead, the segregated algorithm solves the momentum and the pressure correction equation separately. Compared to the coupled algorithm, it is slower to reach convergence. Thus, given the validated results for the incompressible case obtained by D. Keith Walter and Davor Cokljat [22], it was decided to study different airfoils using the same solver. The solver follows the flow chart below (Figure 3.6): it starts solving a coupled system of equations made by the momentum equations, and after it solves turbulence, energy if required, and other scalar equations. In this method, the equations are simultaneously solved in a closely coupled manner. The solution reaches convergence faster than the segregated algorithm, but it requires 1.5-2 times more memory since it saves all the unknowns from the discrete system at every iteration.

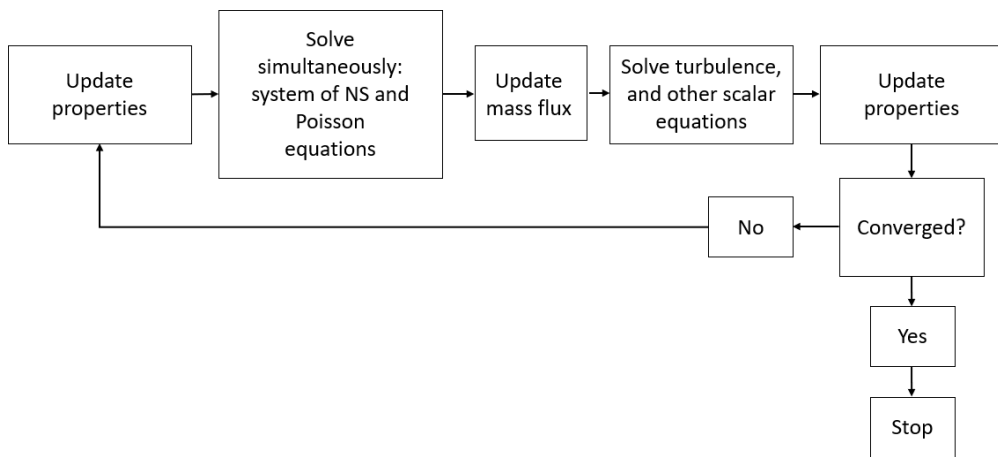


Figure 3.6. Coupled solver flow chart [23]

Chapter 4

Two dimensional CFD analysis of different airfoils

The present chapter is divided into three paragraphs. In the first one, a list of possible airfoils for the wing is individuated considering the constraints. In the second section, the computational domain and the physical parameters are set to validate the numerical solutions of a test case with the experimental results using ANSYS Fluent. Also, the LSB is shown for the case test. In the end, in the last paragraph, two airfoils are selected based on airfoil effectiveness.

4.1 Airfoils identification

Different airfoils which work in the low to moderate Reynolds region were individuated, for a total of twenty airfoils. However, considering the constraints about the airfoil thickness of 14-16%, only five low Reynolds number airfoils satisfied the requirement. The identified airfoils with their characteristics are listed in the Table. ??.

Table 4.1. Low Reynolds number airfoils

Airfoil	Thickness	at chord	Camber	at chord
Gemini	15.4%	34.2%	2.2%	37.9%
MB253515	15.0%	35.0%	2.5%	37.5%
E342	14.3%	31.8%	3.5%	22.2%
E343	14.5%	30.9%	4.0%	26.0%
E344	14.7%	29.9%	4.3%	25.0%

Gemini and MB253515 are classified as airfoils for sport planes, but they were first used for radio-controlled gliders. They are semi-symmetrical, and they are almost identical. The Eppler E342, E343, and E344 are of the flying wing airfoil's family, and they are

characterized by a “small” reflex camber near the trailing edge. This solution helps to reduce the moment coefficient of the airfoil. Since the two different airfoil families, it was decided to find the best one of each family, and later compare their performance in the wing in terms of longitudinal stability and control. The parameter used to select the airfoils is the airfoil effectiveness (3.6).

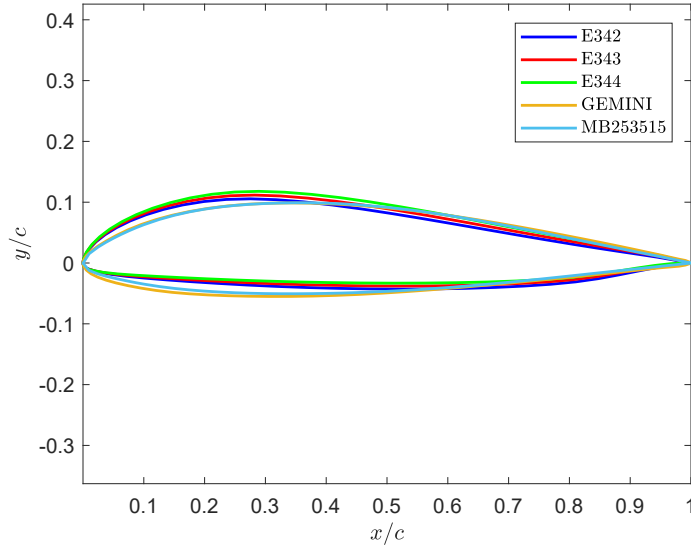


Figure 4.1. Selected airfoils

4.2 Test case

A test case was chosen to perform a two-dimensional analysis in order to:

- Validate the computational analysis in terms of mesh, model, and boundary condition comparing the results with an experimental study.
- Evaluate the presence of the laminar separation bubble on the airfoil.

The test case chosen is the study done by the UIUC on the Gemini airfoil [24], which is also one of the selected possible airfoils for the wing. The Reynolds number calculated using the mean aerodynamic chord of the wing is $Re_{uav} = 2.88 \cdot 10^5$. Instead, the experimental test was conducted at $Re_{exp} = 3.06 \cdot 10^5$. By the way, the difference is negligible, and the two Reynolds numbers are of the same magnitude.

The available results are the aerodynamic coefficients of lift and drag listed in Table 4.2, the freestream turbulence level, temperature, and pressure. Starting from the experimental Reynolds and reversing the equation (3.3), it is possible to find the fluid velocity for a one-meter chord airfoil. The velocity value is $V_{cfd} = 4.38 \text{ m/s}$. Knowing the velocity and the

angles of attack, all the velocity components are found to simulate the different angles of attack.

Table 4.2. UIUC - Aerodynamic coefficients of the Gemini airfoil

α [°]	-5.76	-4.53	-2.47	-1.29	0.76	2.07
C_l	-0.291	-0.193	-0.020	0.093	0.310	0.452
C_d	0.0146	0.0122	0.0106	0.0103	0.0103	0.0114
α [°]	3.58	5.22	6.85	8.25	9.57	11.22
C_l	0.634	0.793	0.938	1.056	1.113	1.111
C_d	0.0134	0.0136	0.0163	0.0178	0.0200	0.0351

4.2.1 Computational domain

ANSYS Fluent can handle 2D meshes, so the created domain is only two-dimensional, and it is not necessary to create a volume domain one-meter depth like in STAR-CCM+ or ANSYS CFX. The geometry was modeled using Design Modeler, a tool of ANSYS Workbench. Before importing the airfoil in the Design Modeler, the airfoils' coordinates were adequately refined. The fluid domain (Figure 4.2) was created using the Boolean operation, which subtracts the airfoil to the whole region. The airfoil leading edge is located at the reference system origin. The C-type geometry reduces the number of mesh elements compared to a rectangular domain, and so the computational cost is reduced. Its dimensions are L=25 m, and D=30 m. Boundaries are far from the airfoil, so the interference effects between boundary and body are minimized. However, instead, the boundary flow is undisturbed.

Through the velocity inlet condition, all the velocity components are assigned in x and y direction to study different angles of attack. The top and bottom edges of the volume are defined as symmetry. The pressure outlet is the boundary condition at the outlet of the volume. Finally, the no-slip condition is assigned to the airfoil surface, where the fluid's velocity is zero in the viscous problem.

Later, ANSYS ICEM CFD was used to create numerical mesh elements. This tool offers a great customizable blocking technique that allows me to design a structured mesh. Firstly, the 2D planar blocking was inserted, associating the edges to the curve of the geometry. An O-grid (Figure 4.3) was introduced around the airfoil to create the prism layer necessary to analyze the boundary layer. The O-grid was also split at the top and bottom surfaces of the airfoil to properly rotate the edge to obtain the more perpendicular possible elements to the airfoil surface. Taking advantage of the O-Grid, the wake was designed, and the C-grid around the airfoil was obtained.

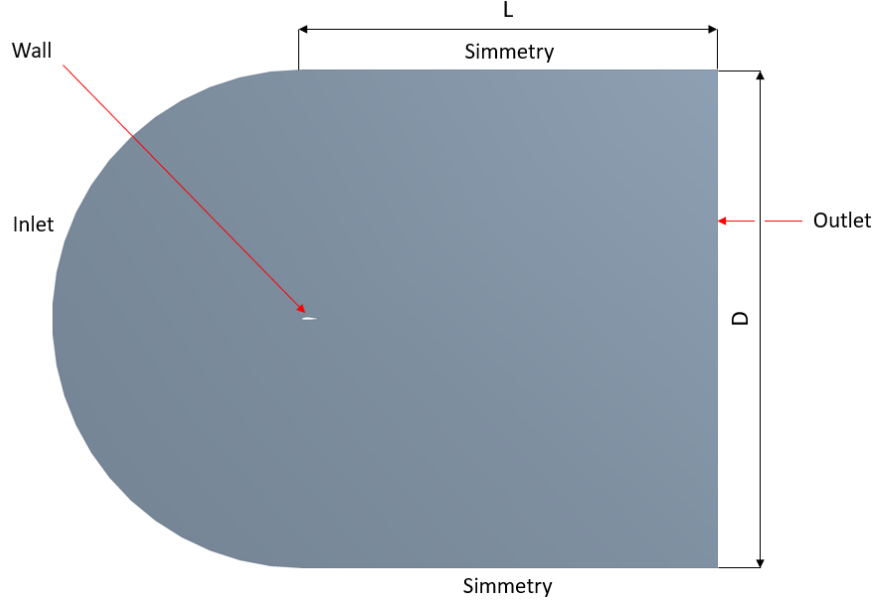


Figure 4.2. Geometry of the computational domain

The airfoil surface was divided into elements, considering that transition occurs over a short distance. Zhang [25] suggested dividing the surface so that each node should have a size of 0.003 times chord since the position of the laminar separation bubble is unknown.

The $k - kl - \omega$ model requires a height of the first cell in the boundary layer y_1 for which y^+ is one or less. To determine y_1 it is necessary to calculate the friction velocity u_τ (3.9), and later find y_1 starting from the definition of y^+ (3.11). The $k - kl - \omega$ model requires a height of the first cell in the boundary layer y_1 for which y^+ is one or less [22]. In the equation (3.9), the wall shear stress is:

$$\tau_w = \frac{1}{2} C_f \rho V^2 \quad (4.1)$$

Where the skin friction coefficient is found using the empirical relationship:

$$C_f = 0.058 \cdot Re^{-0.2} \quad (4.2)$$

Substituting the (4.1) in (3.9) the friction velocity is found. Reversing the relationship of the y^+ (3.11), y_1 is:

$$y_1 = \frac{y^+ \cdot \mu}{\rho \cdot u_\tau} \quad (4.3)$$

Where $y^+ = 1$. Finally, the height of the first cell inside the boundary layer is found and its value is:

$$y_1 = 6.90 \cdot 10^{-5} m \quad (4.4)$$

The thickness of the boundary layer was also estimated using the relationship:

$$\delta(x) = \frac{0.37 \cdot x}{Re^{1/5}} \quad (4.5)$$

This value provides an indication of the boundary layer thickness over a flap plate, but it can be used as an indication to model the boundary layer over the airfoil. Assuming that $x = L = 1 \text{ m}$, the boundary layer thickness is $\delta = 0.0297 \text{ m}$. This value was used as a first guess in ICEM CFD to design the boundary layer height.

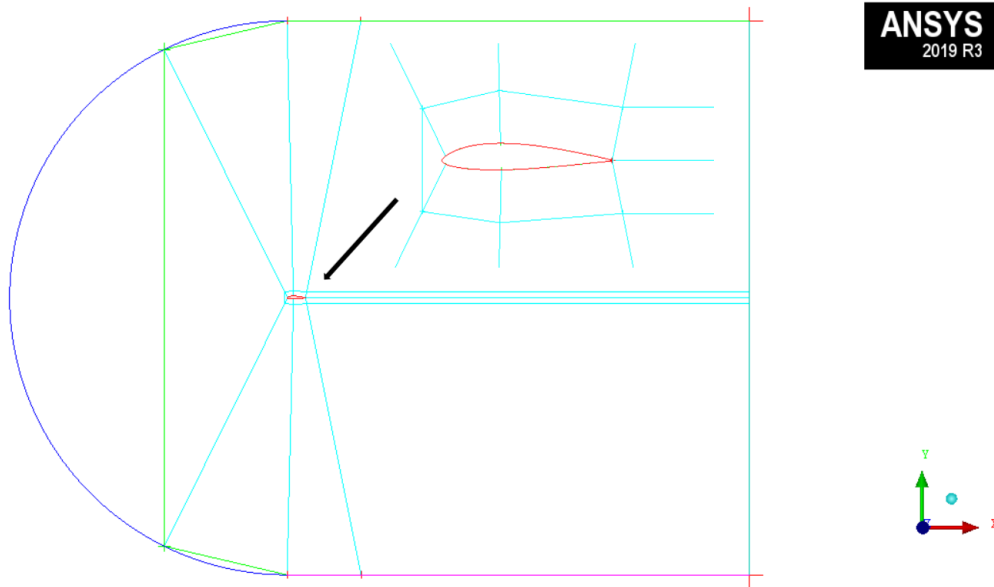


Figure 4.3. ICEM CFD - Blocking strategy and O-grid around the airfoil

Different mesh configurations were studied in the CFD simulations (Table 4.3), and the mesh independence study was done to prove that the solution is independent of the mesh resolution. A total number of three different mesh configurations were analyzed, changing the number and the bias factor of the elements in the normal direction at the airfoil surface, inside the boundary layer, and increasing the number of nodes in the near body wake. For simplicity, the different mesh will be identified using the number of nodes. Figure 4.4 shows an example of mesh around the airfoil, and Figure 4.5 shows the mesh near the leading edge and over the suction surface. The mesh was done trying to have the single mesh's vertical edges closer to the perpendicular condition to the wall to reduce numerical errors in the evaluation of the gradients.

4.2.2 Computational and physical parameters

Reminding that the goal of the present chapter is to individuate the UAV's airfoil that will work in a nominal cruise condition and determine the stability and control derivatives in the linear region, it was decided to study the airfoils only for low-medium angles of attack. Thus, it is possible to use the RANS instead of the URANS [26]. The wing will be studied using XFLR5, a numerical tool developed for low Reynolds airfoils based on panel methods, which provides reliable results in the linear region since it does not consider the viscous effect. Thus, it cannot be used in the region close to the stall. Furthermore, it is

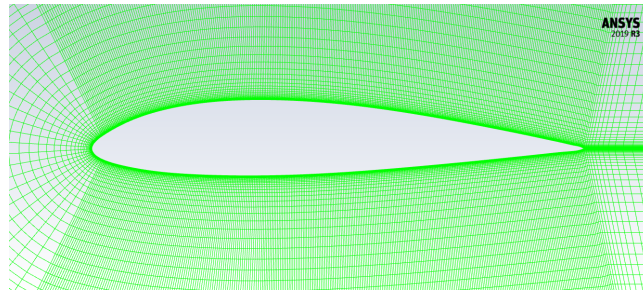


Figure 4.4. Mesh around the airfoil

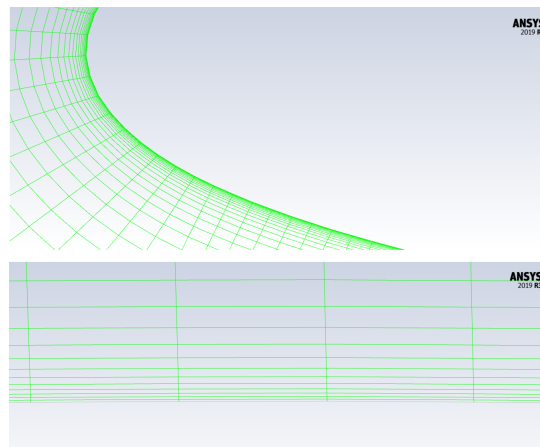


Figure 4.5. Mesh details: leading edge (top) - suction surface (bottom)

unnecessary to study the stall of the airfoil since its computational cost is quite relevant considering the transitional model, and XFRLR5 does not provide any information about the stall.

Table 4.3. Mesh configurations

Type	Number of nodes
Coarse	24012
Medium	59960
Fine	131670

Table 4.4. Angles of attack

α [°]	-4.53	-2.47	-1.29	0.76	2.07	3.58	5.22	6.85	8.25
--------------	-------	-------	-------	------	------	------	------	------	------

Table 4.5. Inlet boundary conditions

Velocity	
V_{cfd} [m/s]	4.38
V_x [m/s]	$V_{cfd} \cdot \cos(\alpha)$
V_y [m/s]	$V_{cfd} \cdot \sin(\alpha)$
Turbulence	
Tu_∞ [%]	0.1
k_L [m^2/s^2]	0
μ_T/μ [-]	10

Table 4.6. Outlet boundary conditions

Pressure	
Prevent reverse flow	On

Table 4.7. Solver and solution methods

Solver	
Type	Pressure-based
Time	Steady
2D Space	Planar
Pressure-Velocity coupling	Coupled
Spatial discretization	
Pressure	Second Order
Momentum	Second Order Upwind
Turbulent Kinetic Energy	Second Order Upwind
Laminar Kinetic Energy	Second Order Upwind
Specific Dissipation Rate	Second Order Upwind
Pseudo Transient Explicit Relaxation Factors	
Pressure	0.5
Momentum	0.5
Density	1
Body Forces	0.75
Turbulent Kinetic Energy	0.75
Specific Dissipation Rate	0.75
Turbulent Viscosity	1
Residuals	
V_x	10^{-6}
V_y	10^{-6}
k_L	10^{-6}
k_T	10^{-6}
ω	10^{-6}
Solution Initialization	Hybrid
Maximum iterations	4000

4.2.3 Results

It was decided to compare the CFD results with the experimental results using the root mean square:

$$RMS(C) = \sqrt{\frac{\sum_{i=1}^N (C_{cfd,i} - C_{exp,i})^2}{N}} \quad (4.6)$$

Where C is the generic aerodynamic coefficient, i is the index relative to the angle of attack, $N = 9$ is the total number of the angles of attack, $C_{cfd,i}$ is the results obtained from ANSYS Fluent, and $C_{exp,i}$ is the experimental coefficient. Thus, it is possible to compare different simulations using a unique parameter characteristic of the single simulation.

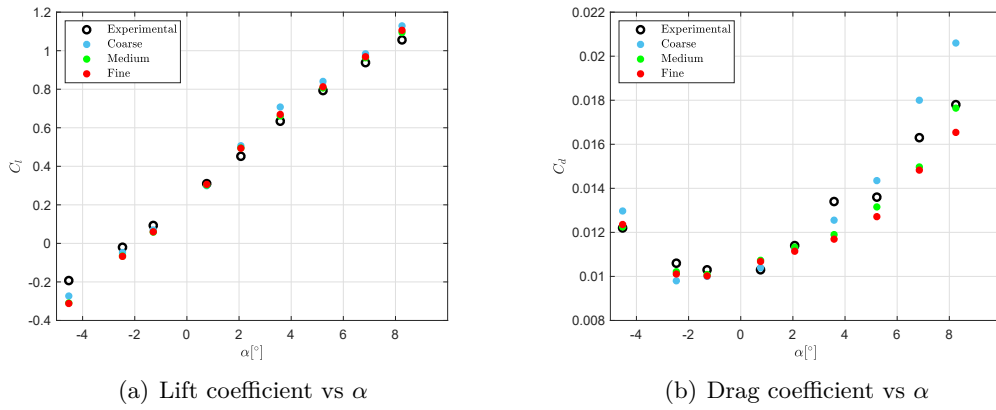


Figure 4.6. Numerical vs experimental results

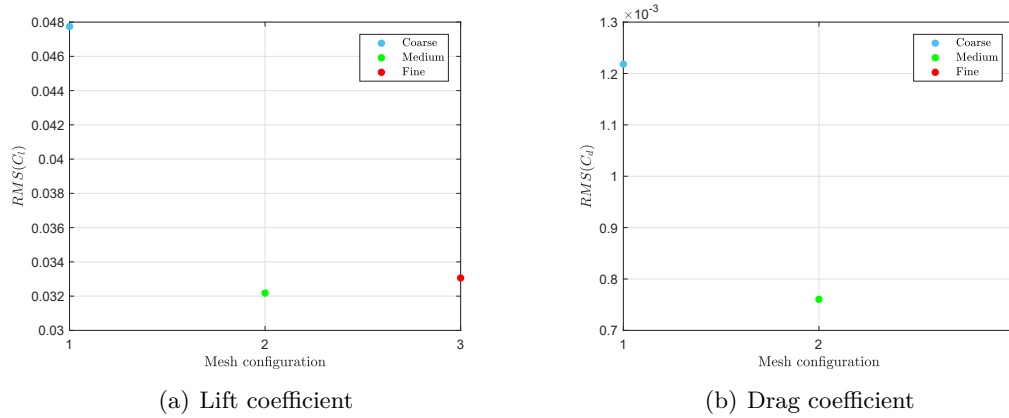


Figure 4.7. Root mean square for different mesh

The aerodynamic coefficients are reported in Figure 4.6. All the simulations seem to provide reliable results if compared to the experimental results, and looking at the Figure 4.7, the root mean square decreases when the mesh is refined. In particular, the lift coefficient, after the decrease between coarse mesh and medium mesh, reaches a linear trend, considering the more refined configurations, medium and fine. The drag coefficient's behavior is the same as the first one, but there is an RMS increase in the passage from medium to fine. However, the two RMS are of the same magnitude, and the linear trend can be individuated.

The y^+ calculated by the solver can indicate if the mesh is sufficiently refined to solve the boundary layer. The transitional model $k - kl - \omega$ requires a $y^+ = 1$ or less, so using the computed velocity components, FLUENT can check if that condition is satisfied. Table 4.8, 4.9, and 4.10 show the minimum and maximum y^+ over the airfoil surface for the different mesh. The coarser mesh satisfies the condition only at $\alpha = 0.76^\circ$, so the refinement was necessary to solve the boundary layer correctly. Instead, medium and fine mesh have a y^+ of about one or less for a high range of angle of attack.

In the computational simulation, the discretization of the domain, so of the equations, with a turbulence model to close the equation system, affect the results, which will never be completely identical to the experimental results. For these reasons, the discrepancy was expected, but we can say that the computational analyses provide results according to the experimental ones.

Finally, considering the root mean square and the elapsed time to complete the simulations for all the angle of attack, it was decided to use the medium mesh configuration to study the other airfoils. The simulation requires about 2.5 hours for the medium-mesh for all the AoAs. Instead, the more refined mesh spends about 4 hours. The used processor is a quad-core Intel Core i7 6700HQ/2.6 GHz with 16 GB RAM.

Table 4.8. Calculated y^+ - Coarse mesh

α [°]	Minimum y^+	Maximum y^+
-4.53	0.0055	1.5289
-2.47	0.0119	1.3188
-1.29	0.0284	1.1682
0.76	0.0088	0.9729
2.07	0.0152	1.0974
3.58	0.0106	1.2876
5.22	0.0144	1.3459
6.85	0.0510	1.6972
8.25	0.0303	1.8212

Table 4.9. Calculated y^+ - Medium mesh

α [°]	Minimum y^+	Maximum y^+
-4.53	0.0055	1.1884
-2.47	0.0134	0.9871
-1.29	0.0087	0.8868
0.76	0.0079	0.6967
2.07	0.0066	0.8265
3.58	0.0088	0.9679
5.22	0.0140	1.0368
6.85	0.0140	1.2929
8.25	0.0111	1.4146

Table 4.10. Calculated y^+ - Fine mesh

α [°]	Minimum y^+	Maximum y^+
-4.53	0.0030	1.1843
-2.47	0.0104	0.9819
-1.29	0.0059	0.8718
0.76	0.0100	0.7086
2.07	0.0095	0.8141
3.58	0.0042	0.9430
5.22	0.0173	0.9874
6.85	0.0030	1.2811
8.25	0.0057	1.4131

4.2.4 CFD results: GEMINI airfoil at $\alpha = 0.76^\circ$

Since the objective of this investigation is to find the best airfoil in terms of effectiveness, it was decided to analyze the CFD result only for the angle of attack of 0.76° , for which the simulation provided results in good agreement with the experimental ones, and investigate if the laminar separation bubble is present or not.

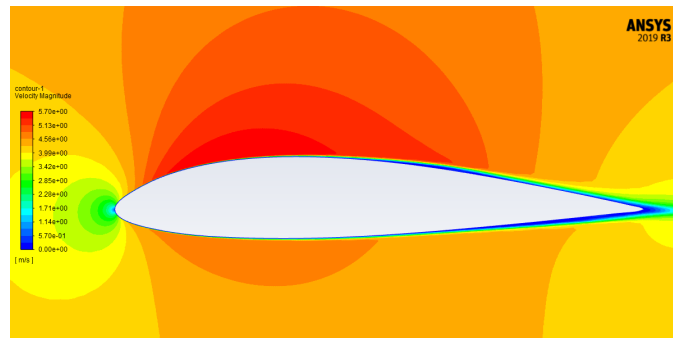


Figure 4.8. Velocity contour

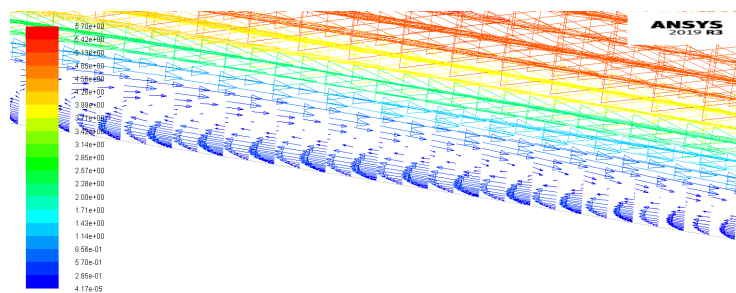


Figure 4.9. Velocity vectors on the upper surface

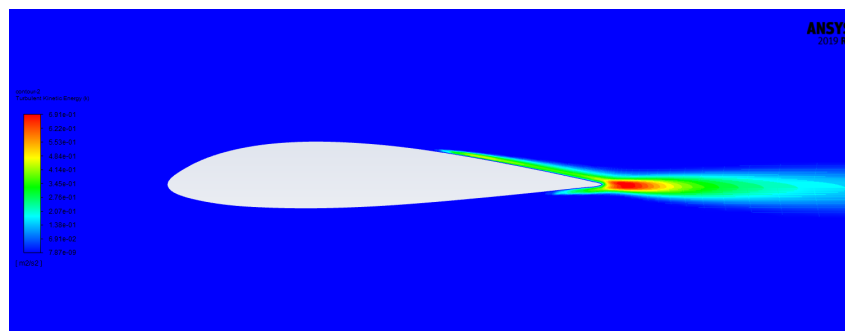


Figure 4.10. Turbulent kinetic energy

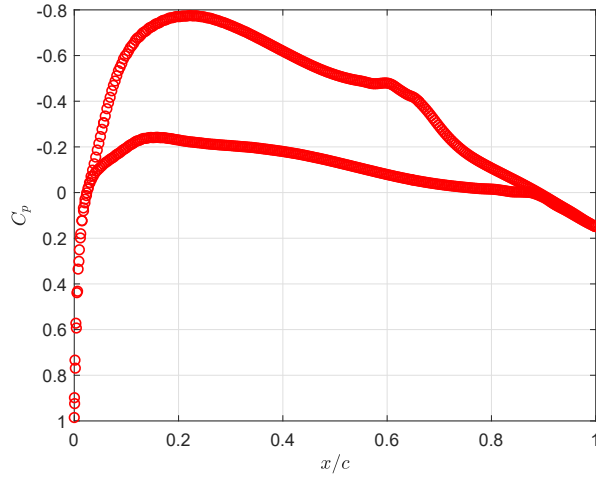


Figure 4.11. Pressure coefficient

In the analyzed case at $\alpha = 0.76^\circ$, the velocity contour (Figure 4.8) shows that there is a thick region of low speed on the upper surface at about $x/c = 0.6$. The velocity vectors in Figure 4.9 indicate a vortex over the airfoil in that area. This area is linked with an increase in the turbulent kinetic energy (Figure 4.10). Considering also the pressure coefficient in Figure 4.11, it shows a small portion on the upper surface at almost constant pressure around $x/c = 0.6$. Thus, in this region, the LSB induces the transition from laminar to the turbulent boundary layer.

4.3 Airfoils selection

The different airfoils listed in Table 4.1 were analyzed using the medium mesh and the same solver configuration, which provided results in agreement with experimental values for the Gemini airfoil. The parameters of the simulations are listed in Tables 4.4, 4.5, 4.6, and 4.7. The only difference is the adding of the zero AoA.

Figure 4.12 and 4.13 show the results of lift, drag, and the moment coefficient about the 0.25% of the chord. All the coefficients are evaluated in the function of the angle of attack.

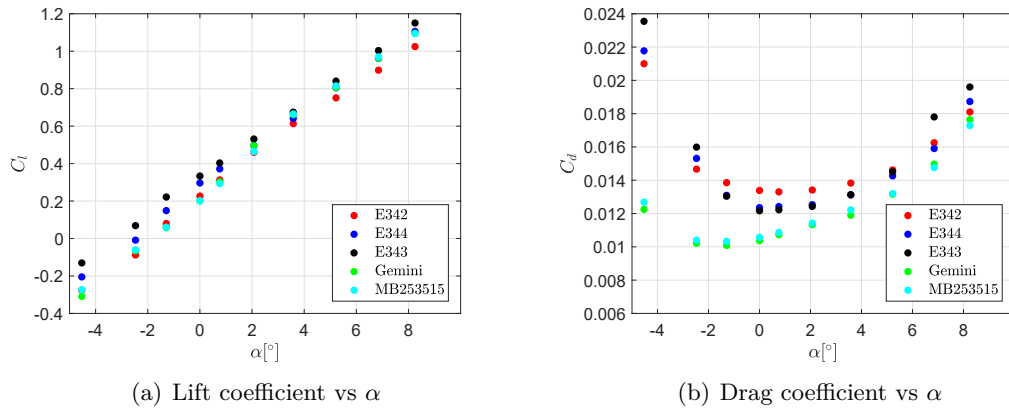


Figure 4.12. CFD results

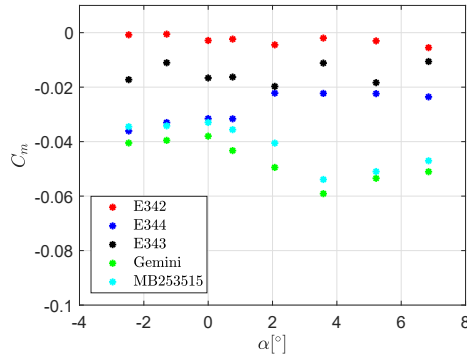


Figure 4.13. Moment coefficient vs α

Table 4.11. Airfoil effectiveness

α [°]	E342	E343	E344	Gemini	MB253515
0	16.9	27.4	24.0	19.3	19.1
0.76	23.5	33.0	29.9	28.2	27.0
2.07	34.3	42.8	39.6	43.7	40.6
3.58	44.3	51.4	48.9	55.6	54.4

Figure 4.12 (a) shows that the lift coefficients developed by the different airfoils are of the same magnitude as expected since the air similar and developed for low to moderate Reynolds numbers. However, Figure 4.12 (b) and 4.13 highlight the differences between the two considered families of airfoils. Looking at the drag coefficient, the semi-symmetrical airfoils, Gemini and MB253515, exhibit lower drag than the other airfoils of the flying wing’s family. Considering now the moment coefficient in Figure 4.13, even if the differences are contained, the reflection effect of the trailing edge causes a reduction of the coefficient for the airfoil of the flying wing’s family compared to the semi-symmetrical.

Table 4.11 lists the different airfoils’ effectiveness in the range of $0^\circ \div 4^\circ$, an interval that contains the angle of attack associated with the steady flight condition of the UAV. For the two different types of airfoils, the ones with the higher values of effectiveness are found: in particular, they are Eppler E343 and Gemini.

However, the effectiveness is not the only parameter to consider for the airfoil’s choice for the wing, but it was used to reduce the number of airfoils to analyze in the next step. It is essential to regard the aircraft performance in terms of longitudinal stability and control (i.e., trimmed angle of attack, deflection of the ruddervator). For these reasons, it was decided to study the longitudinal stability of the aircraft in two different wing configuration: the first made by the E343, and the second one designed with the Gemini.

Chapter 5

Validation of the XFLR5's results

XFLR5 is an open-source software to analyze airfoils, wings, and planes at low Reynolds numbers [27]. It implements the same algorithm of XFOIL to analyze the airfoil. The wing analysis capabilities are achieved using the Lifting Line Theory (LLT), the Vortex Lattice Method (VLM), and the 3D panel method. All of these numerical methods solve Laplace's equation. Thus, XFLR5 is a potential flow method with the advantage of shorter computation time than the RANS: methods like the Navier-Stokes flow solvers take days to set up the CFD grids and hours to converge on a single solution. Instead, the potential flow methods require hours setting up and minutes to compute all the solutions and may be used to generate an aerodynamic database in the linear region [28].

The organization of this chapter is the following. In the first section, the theory of Laplace's equation is explained briefly, since it represents VLM's basis. The implementation of this numerical method in XFLR5 is explained in the second section. In the third part, an experimental investigation is done on a different SkyTeam's UAV. Later, the numerical results are compared with the numerical one of XFLR5 in section five. At the end of the chapter, the numerical grid to use for studying the new UAV is identified.

5.1 Laplace's equation

The governing equations of the fluid dynamics have already been analyzed previously. In particular, a description of them was given in Chapter 3. However, in fluid dynamics, different methods exist to simplify the problem and solve it within some approximations. Starting from the governing fluid dynamics equations (3.12),(3.13), (3.14), if the following hypotheses are verified, the Euler's equations are obtained. In particular, assuming the absence of heat sources in the fluid volume, considering an inviscid fluid without thermal conductivity, the Euler's equations are:

$$\frac{\partial \rho}{\partial t} + \nabla \cdot (\rho \vec{V}) = 0 \quad (5.1)$$

$$\frac{\partial(\rho \vec{V})}{\partial t} + \nabla \cdot (\rho \vec{V} \vec{V} + p \vec{I}) = 0 \quad (5.2)$$

$$\frac{\partial(\rho E)}{\partial t} + \nabla \cdot [(\rho E + p)\vec{V}] = 0 \quad (5.3)$$

Where \vec{I} represents the identity matrix that provides the pressure components along with the three directions in a three-dimensional problem. If the fluid is incompressible, the equation (5.1) expresses the solenoidal condition of the fluid flow:

$$\nabla \cdot \vec{V} = 0 \quad (5.4)$$

Under the assumption of irrotational fluid, which means the fluid particles translate without any rotation, the vorticity is zero in every point of the fluid domain. The vorticity is defined as the rotor of the velocity vector:

$$\vec{\omega} = \nabla \times \vec{V} = 0 \quad (5.5)$$

This condition leads to the existence of a scalar function ϕ , which is called velocity potential. It is defined as:

$$\vec{V} = \nabla \phi \quad (5.6)$$

Substituting the velocity potential in equation (5.4), Laplace's equation is defined:

$$\nabla^2 \phi = 0 \quad (5.7)$$

Substituting the potential in the Navier-Stokes equations provides the Bernoulli's equation for unsteady flow. For incompressible flow, the energy equation is decoupled from mass balance and Navier-Stokes equations. Thus, for an incompressible and irrotational fluid, the problem is to find two scalar quantities: pressure and velocity potential. So the procedure is to solve Laplace's equation firstly, determining ϕ , and so the velocity. Found ϕ , the pressure is determined through Bernoulli's equation. The solution of Laplace's equation depends only on the instantaneous boundary conditions. In terms of potential flow, they may be:

- Dirichlet type, where the velocity potential is assigned at specific locations:

$$\phi = \phi_0$$

- Neumann type, where the gradient of the potential is known on a surface, so it is the velocity vector. Indicating with \vec{n} the normal direction to a wall, and with \vec{V}_w the velocity vector at the wall, this condition is:

$$\frac{\partial \phi}{\partial \vec{n}} = \nabla \phi \cdot \vec{n} = \vec{V}_w \cdot \vec{n}$$

Supposing that ϕ_1 and ϕ_2 are two generic solutions of Laplace's equations, which means:

$$\nabla^2 \phi_1 = 0 \quad \nabla^2 \phi_2 = 0 \quad (5.8)$$

Then any linear combination of ϕ_1 and ϕ_2 is a solution to the problem:

$$\mu_1 \nabla^2 \phi_1 + \mu_2 \nabla^2 \phi_2 = 0 \quad (5.9)$$

For solving the problem, the algorithm divides the lifting surface in N elementary surfaces where are located different elementary solutions. They are the point source, the doublet, and the vortex line. Every one of them is a solution of Laplace's equation. The global solution of the problem is found as a linear combination of elementary solutions. Furthermore, on each panel, the boundary condition is applied. The flow over every elementary surface must follow the tangent condition:

$$\nabla\phi \cdot \vec{n} = \vec{V} \cdot \vec{n} = 0 \quad (5.10)$$

Finally, there are N equations for N variables, and the problem is reduced to solve a linear system of equations.

5.2 Vortex Lattice Method in XFLR5

The Vortex Lattice Method (VLM) is the only numerical method available in XFLR5 that allows studying the UAV, which is comprehensive of a swept wing and tail. The fundamental hypotheses of this method are:

- Incompressible, inviscid, and irrotational fluid flow.
- Thin lifting surfaces.
- Small angles of attack.

Under the previous assumptions, the velocity vector may be seen as:

$$\vec{V} = \vec{V}_\infty + \nabla\varphi \quad (5.11)$$

In the VLM, the wing is split into a lattice of quadrilateral elements collocated on the mean chamber line. This model involves the distribution of vortices on each element, and with that, it models the perturbation generated by the lifting surface. The vortex configurations may be of two different types, so two different VLMS can be used in XFLR5. They are:

- VLM1, where a horseshoe vortex is placed on each elementary panel at the panel quarter chord. Considering the single panel, the front part of the vortex models the lifting properties, and the two semi-infinite vortices that propagate in the parallel direction to the symmetry axis of the wing model the wake. The control point, where the boundary condition is imposed, is located at the three-quarter of the chord.
- VLM2 does not employ horseshoe vortices on every panel, but the horseshoe vortices are located only at the trailing edge of the wing for representing the wake. Instead, the elements over the wing are modeled using quad vortices, also called ring vortices. The strength of the trailing vortex is equal to the strength of the trailing edge ring, and in this way, the wake is without any force. Also, in this case, the tangential flow condition is imposed at the three-quarter of the chord at the control point.

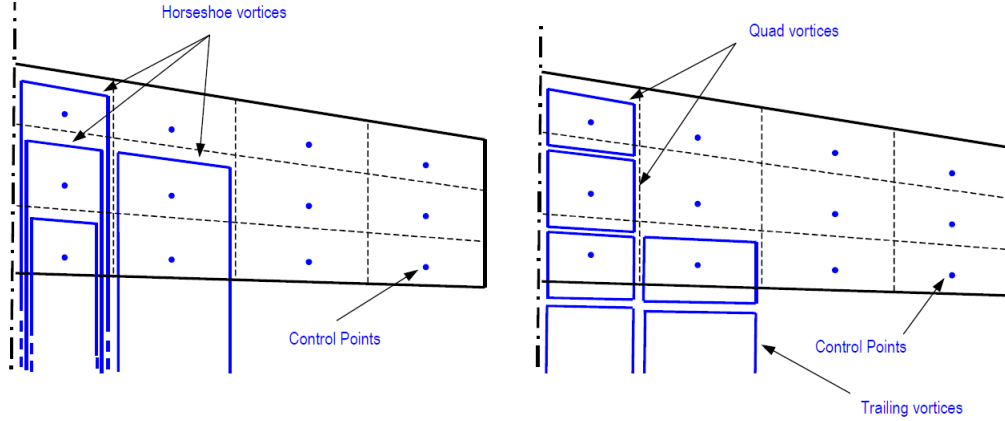


Figure 5.1. VLM1 (left) - VLM2 (right) [29]

The perturbation velocity is determined at the control point i , by the sum of all the horseshoe's contributions. The velocity on the control point of the i panel is defined as:

$$\vec{V}_i = \vec{V}_\infty + \nabla\varphi_i \quad (5.12)$$

In a three-dimensional problem the velocity has three components along \hat{i} , \hat{j} , and \hat{k} . Considering the angle of attack α , and the sideslip angle β , they are:

$$\vec{V}_\infty = V_\infty \cdot (\cos \alpha \cos \beta, -\sin \beta, \sin \alpha \cos \beta) \quad (5.13)$$

The effects of the j panel on the i panel, is represented by the aerodynamic influence coefficient w_{ij} , which is a $N \times N$ matrix. Thus, the perturbation velocity at the control point i is:

$$\nabla\varphi_i = \sum_{j=1}^N w_{ij} \Gamma_j \quad (5.14)$$

Γ_j is the unknown vortex strength. The boundary condition at every control point is the flow tangency condition:

$$\vec{V}_i \cdot \vec{n}_i = \left(\vec{V}_\infty + \sum_{j=1}^N w_{ij} \Gamma_j \right) \cdot \vec{n}_i = 0 \quad (5.15)$$

By defining the following terms:

$$b_i = \vec{V}_\infty \cdot \vec{n}_i = V_\infty (-\cos \alpha \cos \beta, \sin \beta, -\sin \alpha \cos \beta) \cdot \vec{n}_i \quad (5.16)$$

$$a_{ij} = w_{ij} \cdot \vec{n}_i \quad (5.17)$$

The system of equations (5.15) may be arranged in a matricial form:

$$\begin{bmatrix} a_{11} & \dots & a_{1N} \\ \vdots & \ddots & \dots \\ a_{N1} & \dots & a_{NN} \end{bmatrix} \begin{Bmatrix} \Gamma_1 \\ \vdots \\ \Gamma_N \end{Bmatrix} = \begin{Bmatrix} b_1 \\ \vdots \\ b_N \end{Bmatrix} \quad (5.18)$$

The unknowns of the problem are the vortex strengths, which are found solving the linear system using either the near field or the far field method. The first one integrates the pressure forces on the panels, and its results are less representative than the second method, which determines lift and drag starting from the balance of the momentum on a far field plane downstream of the body. This control surface is called Trefftz plane. XFLR5 implements the latter, and the lift on the wing is the lift calculated in the Trefftz plane using Kutta-Joukowski’s theorem [29].

XFLR5 employs the wind axis to calculate the aerodynamic coefficient. In this tool, the velocity is maintained constant the XZ -symmetry plane along the X -axis, and the body’s geometry is tilted around the axis to study different AoAs and sideslip angles.

Since the VLM solves Laplace’s equation, which omits the viscosity, all the unknowns of the problem are supposed to be independent by this air’s property. Thus, VLM provides reliable results where the viscosity is negligible and at low angles of attack, where the flow separations are limited to portions of the wing close to the trailing edge. Furthermore, the lift distribution calculation, the induced angles, and the induced drag are both inviscid and linear, so they are independent of the aircraft’s speed and viscosity [29].

5.3 Experimental analysis at the wind tunnel

The customized Freewing Eurofighter Typhon with the V-Tail was examined at the wind-tunnel facility of Aero-Tunnel in Gorizia, Italy, to validate some numerical results obtained in XFLR5. The Eurofighter was tested at the speed of 17 m/s . Considering the standard conditions of pressure and temperature, and the mean aerodynamic chord of 0.2625 m , its Reynolds number (3.3) is:

$$Re_{exp} = 3.04 \cdot 10^5 \quad (5.19)$$

In this way, the Eurofighter was investigated at a Reynolds number of the same magnitude of the new UAV’s Reynolds. However, it is essential to say that in XFLR5, the velocity effect using the VLM method does not appear. Nevertheless, this analysis was done to verify the capabilities of XFLR5 to provide some aerodynamic performances in low to moderate Reynolds numbers.

The wind tunnel is the facility where researchers conduct experimental aerodynamic tests, simulating the aerodynamic condition on a scaled or real-size model. These facilities may be classified on the speed regime inside the test section. Using the Mach number, they are divided into:

- Subsonic - $M < 0.8$
- Transonic - $0.8 < M < 1.2$
- Supersonic - $1.2 < M < 5$
- Hypersonic - $M > 5$

The design of a wind tunnel is affected by the flow regime at which it works. For example, in a subsonic wind tunnel, the test section has the smallest cross-area of the tunnel.

Instead, for a supersonic tunnel, the nozzle’s throat has the smallest cross-area, and the test section dimensions are chosen to reach the desired Mach number. For the small UAV’s application under investigation in this work, the flow regime is incompressible since the Mach is about 0.06. Thus, considering the subsonic wind tunnels, they may be divided into:

- Open return tunnel or Eiffel wind tunnel.
- Closed return tunnel, also called Prandtl wind tunnel.

The first one draws air from the surrounding environment on which the wind tunnel is located. Instead, in a closed return tunnel, the air re-circulates inside the conduct.

During the experimental analyses, the forces and moments are measured using the apposite instrumentation. After that, the dynamic similitude allows the transfer of the problem’s coefficient from the model to the real application. A model has dynamic similitude with the real problem if they share geometric, dynamic, and kinematic similarities. In the aerodynamic field, for incompressible flows, the similitude is expressed by the Reynolds number. It means that the experiments may be done at different conditions, but if the Reynolds number is the same, they provide the same adimensional results, which are the aerodynamic coefficients.

Aero-Tunnel employs a closed return tunnel, and its length is 102 meters. There are two test sections (TS) with different dimensions where the model can be located (Figure 5.2). Indicating with H the height, W the width, and L the length of the test section, the dimensions of the two test sections are:

- TS n°1: $H=2.4$ m, $W=2.4$ m, $L=5.0$ m
- TS n°2: $H=2.4$ m, $W=7.0$ m, $L=10$ m

The first test section is the one employed for the Eurofighter investigation. The velocity is measured inside the test section with some Pitot tubes. The model may be located on different types of support, which connect it to the six-axis dynamometric balance. The signals from the Pitot and the balance are sent to the acquisition system. The second test section, since the larger dimension, may be used for environmental studies. The maximum achievable speed in the test section is 45 m/s, but it may be increased at 70 m/s. This velocity is reached thanks to the eight fans. They are located at the end of the divergent segment of the conduct immediately downstream of the test section. If an accident occurs, a protective net avoids the injection of parts in the fans. This net is located at the end of the test section. Figure 5.3 shows a detail of the Eurofighter in the test section mounted on the three-points support, which is jointed to the dynamometric balance. The Eurofighter’s lift, drag and moment coefficients obtained for sideslip angle zero are listed in Table 5.2.

5.4 Aerodynamic coefficients

5.4.1 Drag coefficient

One of the VLM hypotheses is the inviscid fluid, so friction drag and pressure drag are both zero, but it provides the value of the lift induced drag. In general, XFLR5 solves

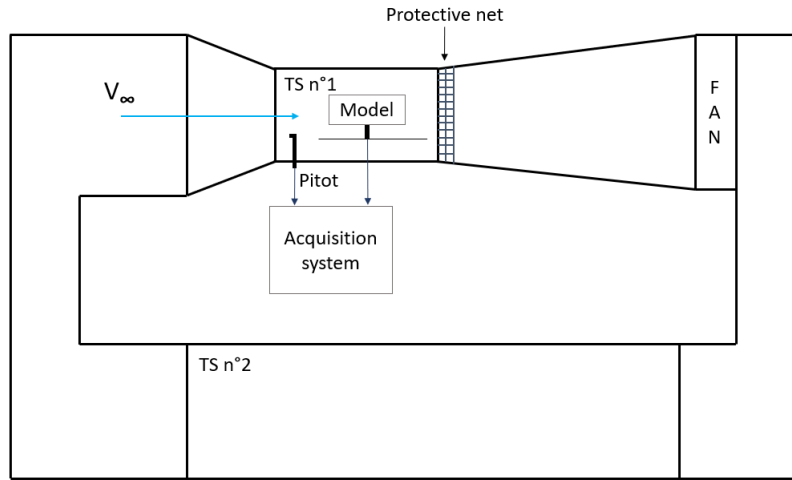


Figure 5.2. Wing tunnel schematization

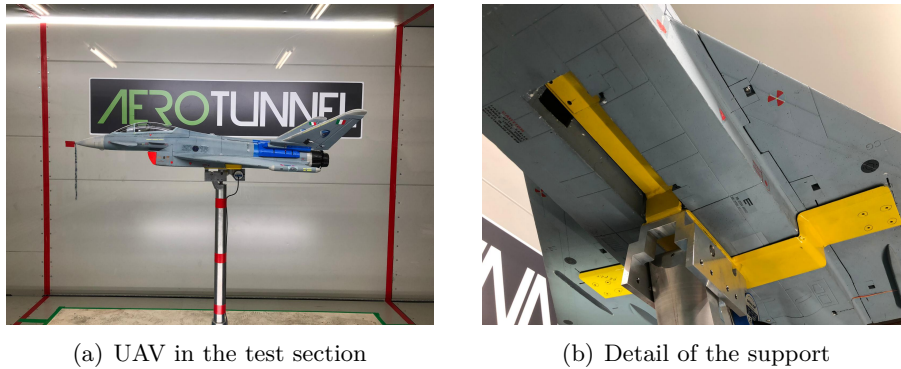


Figure 5.3. Customized Freewing Eurofighter Typhoon inside the TS n°1

the inviscid problem, providing the aerodynamic coefficients. After, if the viscous flow is enabled, it interpolates the two-dimensional results obtained in the airfoils analysis with Xfoil to estimate the parasite drag. However, it may indicate the general trend of the coefficient, but this method is not based on any physical aspect. Also, the values of drag are underestimated (Figure 5.4). In conclusion, the drag values obtained in the viscous analysis in XFLR5 will not be considered late, and the analysis will focus only on the other coefficients.

5.4.2 Lift and moment coefficients

The experimental results of $C_L(\alpha)$ and $C_M(\alpha)$ determined in the wind tunnel tests are compared with the numerical simulation results obtained in XFLR5. The analysis performed in XFLR5 do not consider the fuselage, but only wing, tail, and canard (Figure

Table 5.1. Experimental results

α [°]	C_L	C_D	C_M
-5.77	-0.2741	0.0785	0.0662
-3.72	-0.1594	0.0494	0.0549
-1.80	-0.0612	0.0365	0.0419
0.36	0.0524	0.0352	0.0189
2.58	0.1564	0.0451	0.0025
4.35	0.2449	0.0631	-0.0132
6.31	0.3303	0.0953	-0.0310
8.24	0.4658	0.1528	-0.0532
10.24	0.5549	0.2183	-0.0745
12.27	0.6317	0.2966	-0.0944
14.16	0.7119	0.3909	-0.1133
16.35	0.7398	0.4762	-0.1295

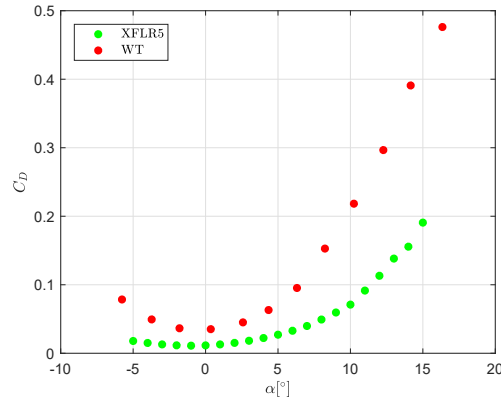


Figure 5.4. Drag coefficient

5.5). Different meshes were created using the internal tool of XFLR5 in order to find the configuration with the best agreement to the experimental coefficient. XFLR5 allows three different arrangements of the mesh along the X -axis and Y -axis. In particular, the elements may be distributed uniformly, cosine spaced, and sine spaced. For each configuration, the mesh was refined to perform the mesh independence study. The so found results are compared with the experimental values, and through the root mean square, the configuration with the minimum RMS is chosen. In this way, the optimal mesh arrangement and the density of panels for a square meter for wing and tail are defined to study the new UAV. Since XFLR5 implements two different VLMs, this study aims to evaluate also the difference in the results and time elapsed between VLM1 and VLM2.

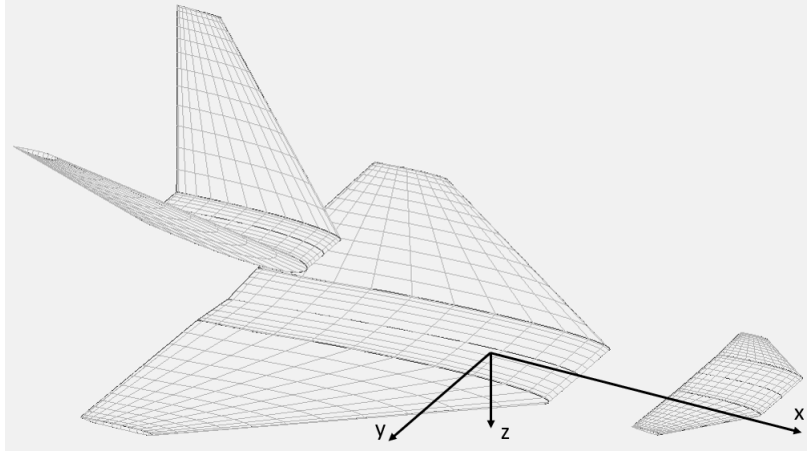


Figure 5.5. Eurofighter model in XFLR5

Some recommendations were followed to design different panels distributions [29]:

- The distribution must be consistent with the geometry of the wing.
- The mesh density must be increased at geometrical breakpoints, like the tip of the wing.
- The cosine spaced distribution is preferred in the chordwise direction since it provides higher density at the leading and trailing edges.

Although the uniform distribution is not suggested and does not follow some of the previous indications, it was decided to evaluate the behavior of the numerical method in such a case. Thus, the investigated cases are:

- Distribution *A*: panels distributed uniform on wing, tail, and canard.
- Distribution *B*: cosine type distribution chordwise, and minus sine distribution along the span for wing, tail, and canard.
- Distribution *C*: cosine type distribution chordwise, minus sine distribution along the span for the wing, and uniform distribution for the tail.

Ten different mesh were compared for every configuration. Between the different configurations, the refine factors are the same. Thus, the different configurations can be compared with the same number of elements.

The mesh refinement causes an increase in the time elapsed to complete the numerical simulation. Table 5.3 collects the time for every simulation performed, comparing the time requested by the two different VLMs. It shows that the time for the VLM is relatively limited to a few seconds, and only for the tenth mesh is about some minutes. However, it will be shown later that the results is independent by the mesh at the fifth mesh, so a solution is found in less than a second for every angle of attack. Finally, the time is

Table 5.2. Mesh analyzed

Mesh	1	2	3	4	5	6	7	8	9	10
Elements	48	192	432	672	960	1080	1482	1980	3360	10032

Table 5.3. Time elapsed

Mesh	Elements	A		B		C	
		VLM1 <i>t</i> [s]	VLM2 <i>t</i> [s]	VLM1 <i>t</i> [s]	VLM2 <i>t</i> [s]	VLM1 <i>t</i> [s]	VLM2 <i>t</i> [s]
1	48	0.402	0.416	0.315	0.308	0.305	0.301
2	192	0.597	0.426	0.420	0.301	0.514	0.301
3	432	0.983	0.588	0.941	0.559	0.968	0.537
4	672	1.837	0.552	1.778	0.785	1.661	0.523
5	960	3.388	1.020	3.169	0.937	3.171	0.978
6	1080	4.054	1.214	4.122	1.176	3.987	1.147
7	1482	7.767	2.242	7.811	2.186	7.812	2.166
8	1980	14.301	4.428	14.040	4.392	14.265	4.386
9	3360	47.624	18.892	47.439	19.650	47.207	19.439
10	10032	851.264	530.801	842.616	515.442	800.386	482.43

affected by the machine used for the simulation. In this case, the used processor is a quad-core Intel Core i7 6700HQ/2.6 GHz with 16 GB RAM.

For every distribution (A, B, C), the *RMS* between two successive mesh, the second one $i + 1$ more refined than the first one i , is evaluated. In this way, it is possible to know when the solution does not change even if the mesh is refined more and more. The used parameter is:

$$RMS(C_K)_{mesh} = \sqrt{\frac{\sum_{i=1}^N (C_{K \text{ mesh},i} - C_{K \text{ mesh},i+1})^2}{N}} \quad (5.20)$$

In the definition (5.20), C_K may be the lift or moment coefficient of the Eurofighter, N is the total number of point computed for the polar. From the study of $RMS(C_K)_{mesh}$, it is possible to find at which mesh the variation of the solution is negligible, so the convergence is reached. Figures 5.6, 5.7, and 5.8 show the trend of the (5.20) calculated for each distribution of the elements when the mesh is refined. In a few refinements, the solutions for the lift and moment coefficients, calculated with the two VLMs, reach the convergence, and the *RMS* has a linear trend close to zero. With these considerations, it

was decided to use the fifth mesh, and to compare its results with the experimental ones.

Figures 5.9, 5.10, and 5.11 report the numerical results for the Mesh 5 for all of three distributions compared to the experiments. Since the results are very close, it was decided to report three different graphs for each aerodynamic coefficient. To evaluate the discrepancy between numerical and experimental results the root mean square is employed again:

$$RMS(C_K)_j = \sqrt{\frac{\sum_{i=1}^N (C_{K\ XF,i} - C_{K\ WT,i})^2}{N}} \quad (5.21)$$

Where C_K may be the lift coefficient C_L , and the moment coefficient C_M of the Eurofighter, and j represents the generic distribution A , B , or C . The subscript XF indicates a coefficient obtained in XFLR5, and WT is the results from the wind tunnel. The aerodynamic coefficients are evaluated at the attack angles used during the experimental investigation, and they are limited to the linear region of the curves ($-3.72^\circ < \alpha < 6.31^\circ$). Thus, $N = 6$. Figure 5.12 reports the RMS for the aerodynamic coefficients. The numerical results are very close to the experimental results for both C_L and C_M , and the differences between the different configurations are minimal.

Although the uniform spaced elements could have caused numerical instabilities, no one was observed, and both the VLMs provided accurate results. However, since the uniform spacing could have numerical problems in other aircraft configurations, it will not be considered for future analyses. Even if the differences are minimal, the "B" distribution with cosine spacing in the chordwise direction, and minus sine along the span, seems to be more accurate. So it will be used to analyze the small UAV. Finally, both the VLMs work well but the VLM2 is generally faster than the other one.

The VLM has limitations in drag estimation. However, it provides a faster solution to the Navier-Stokes RANS, especially when it is necessary to proceed to the characterization of a vehicle with so many control surfaces and find all the associated aerodynamic and control derivative.

5.5 Numerical grid

The previous study individuated Mesh 5 as the optimal to determine the aerodynamic coefficients of the Eurofighter in the linear region for small angles of attack, where the Reynolds effect does not influence the aerodynamic of the aircraft. However, the geometry of this aircraft is different from the UAV that is designed during this thesis. Knowing the geometry of Eurofighter's wing, tail, and the number of elements, the density of elements per square meter is calculated. They are wing's panels, p_w , and tail's panels, p_t :

$$p_w = 890 \text{ panels}/m^2 \quad (5.22)$$

$$p_t = 833 \text{ panels}/m^2 \quad (5.23)$$

This value represents the minimum density of elements per square meter that has to be achieved in the study of the new UAV.

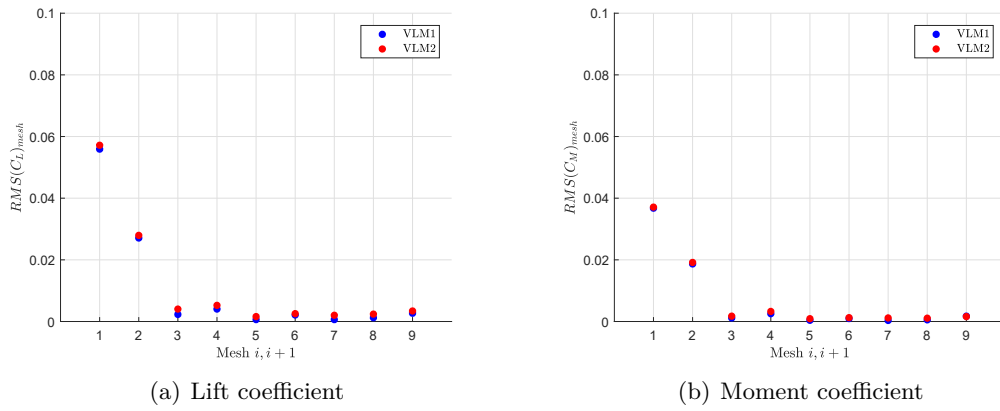


Figure 5.6. Distribution A – $RMS(C_K)_{mesh}$

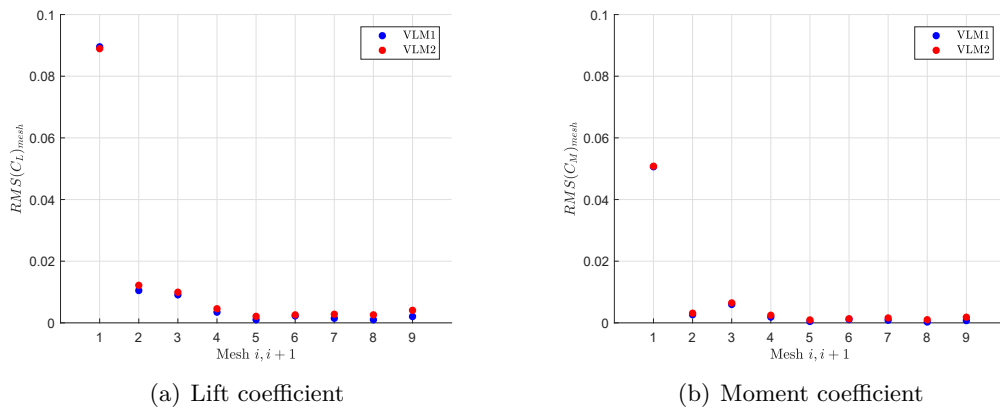


Figure 5.7. Distribution B – $RMS(C_K)_{mesh}$

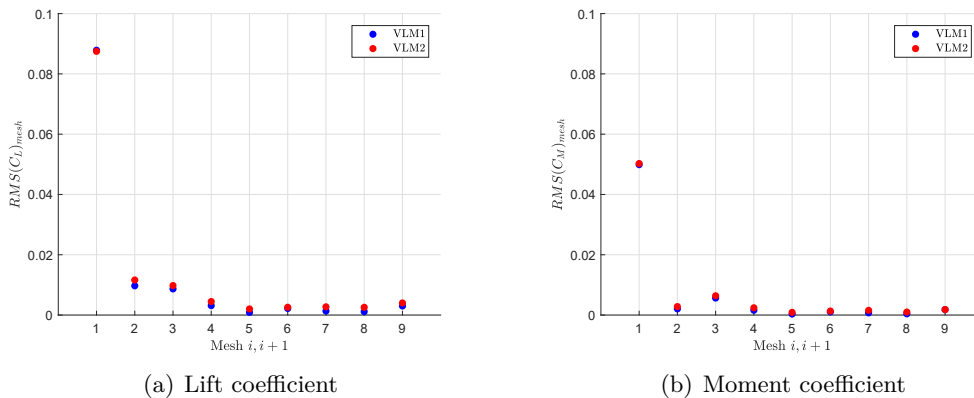


Figure 5.8. Distribution C – $RMS(C_K)_{mesh}$

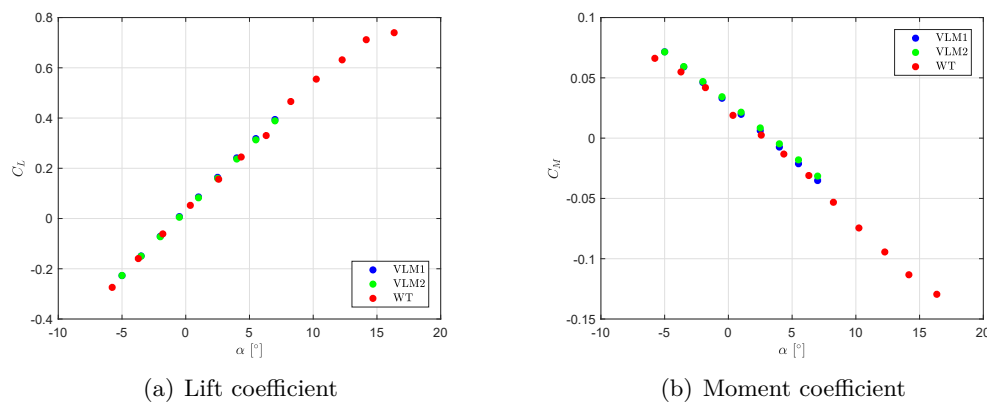


Figure 5.9. Distribution A, Mesh 5 - Aerodynamic coefficients

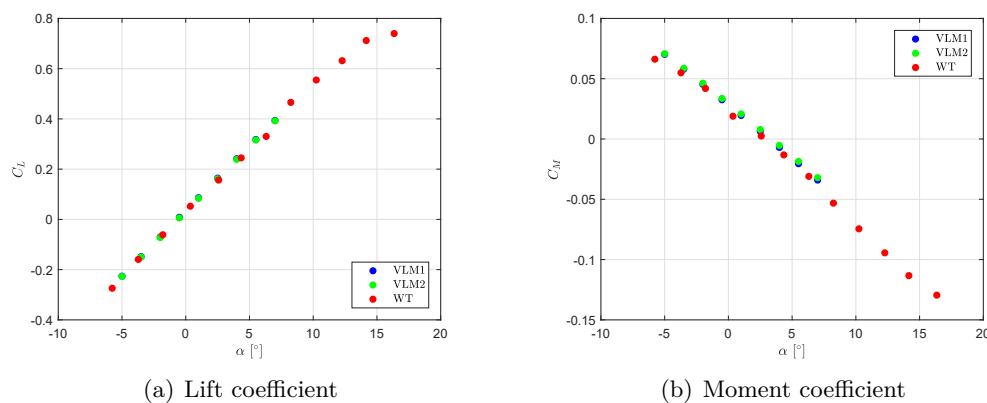


Figure 5.10. Distribution B, Mesh 5 - Aerodynamic coefficients

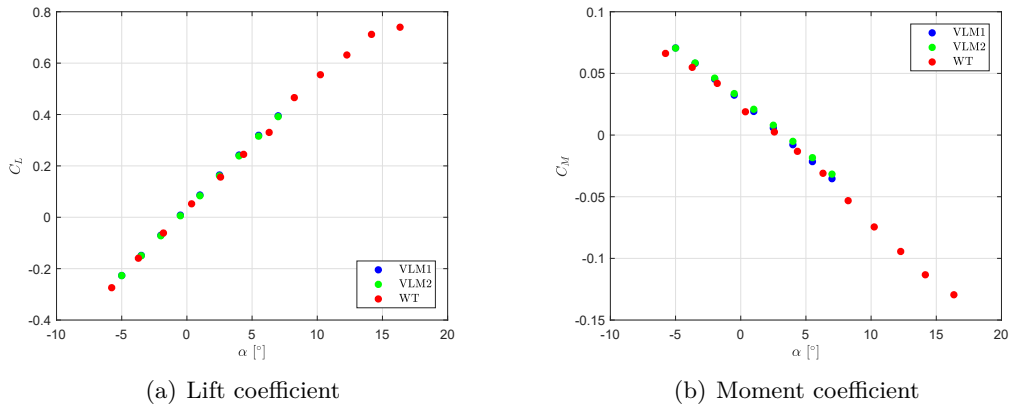


Figure 5.11. Distribution C, Mesh 5 - Aerodynamic coefficients

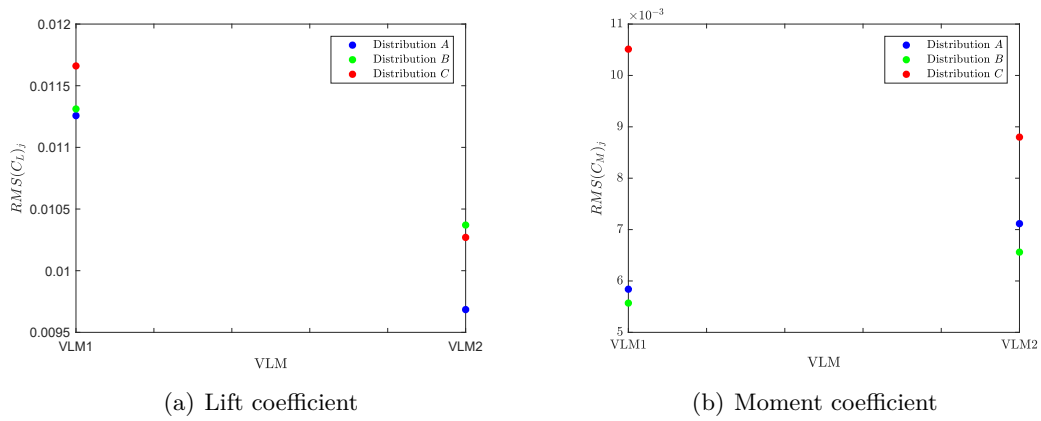


Figure 5.12. Mesh 5 - $RMS(C_K)_j$

Chapter 6

Aerodynamic characterization of the UAV

The aerodynamic characterization of the UAV is necessary for the future work of the control engineer. It is essential to indicate the reference system on the UAV, which allows us to define the positive forces directions and moment rotations of pitching moment M , rolling moment L , and yawing moment N . Figure 6.1 shows the body reference system used to study the UAV. This UAV configuration is called "clean", and it represents the UAV without any control surfaces deflected at zero angles of attack and sideslip. Its aerodynamic coefficients are indicated with the subscript *clean* when the finite-difference method is applied to calculate the derivatives. In the next sections, the positive rotation of a control surface is intended when the surface's trailing edge moves downward.

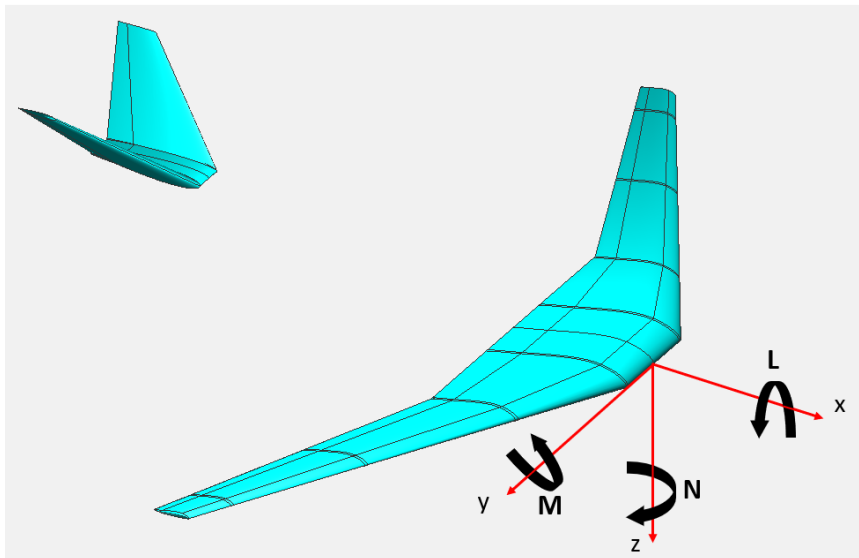


Figure 6.1. UAV's reference system

Firstly, thanks to the theory of longitudinal aerodynamic, it is possible to verify if the aircraft is static stable longitudinally. This aircraft's property is connected to the aircraft geometry and weights distribution, so this examination will certify if the previous design work was done correctly, or if changes are needed. Furthermore, the airfoil has to be chosen, considering its influence on the minimum angle of attack and elevator deflection. This investigation will provide the UAV's aerodynamic coefficient $C_{L\alpha}$, $C_{M\alpha}$, and the longitudinal control derivatives $C_{L\delta}$, $C_{M\delta}$ generated by the elevator deflection for both the wing configurations. In the end, the airfoil choice is taken, considering which one of the two wings can fly at the minimum angle of attack with the minimum elevator deflection.

The second section's objective is to evaluate the UAV's lateral aerodynamic, so the vehicle is not maintained in its symmetry plane. It involves forces along the Y -axis and moments about the X and Z axes. Finally, the control derivatives will show the effects of flaps, ailerons, slats, and ruddervator on the vehicle's dynamics. All the derivatives are evaluated at $\alpha = 0^\circ$ since their values represent the general characteristics of the vehicle. However, the Appendix collects all the numerical results obtained in the present work of thesis, and the derivatives evaluated for different angles of attack.

6.1 Longitudinal aerodynamic

In this section, the vehicle's longitudinal static stability is evaluated. In this case, the sideslip angle β is zero, and the problem is simplified, considering the rotations of the vehicle only about the Y -axis. Two wings are considered: one made by the Eppler E343 and the other one by the Gemini airfoil. The airfoil that will guarantee the minimum angle of attack in the range $0^\circ < \alpha_{eq} < 4^\circ$, and the minimum deflection of the elevator included in $-5^\circ < \delta_{e,eq} < 5^\circ$ will be used for the UAV's wing.

This section is split into three sections: the first one explains the theoretical background of longitudinal static stability. The middle section regards the longitudinal control of the flight vehicle and the elevator's effects on the flight. In the last part, all the aerodynamic coefficient regarding the longitudinal control are calculated using XFLR5 and a finite-difference method.

6.1.1 Static stability

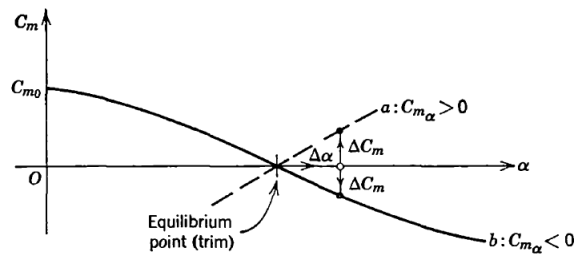


Figure 6.2. Moment coefficient with respect to angle of attack [30]

A vehicle in symmetric steady flight which flies at the equilibrium point, α_{eq} , is characterized by zero pitching moment C_M . An external disturb, like a wind gust or turbulence, may occur, causing a variation of the moment coefficient ΔC_M . When it happens, there may be two different behaviors:

- Curve (a), where the airplane suffers an increase in its α , so:

$$C_{M\alpha} = \frac{\partial C_M}{\partial \alpha} > 0 \quad (6.1)$$

- Curve (b), the flight vehicle produces forces and moments to restore the starting trimmed condition, without any command by the pilot. In this case:

$$C_{M\alpha} < 0 \quad (6.2)$$

The property $C_{M\alpha} < 0$ is called static longitudinal stability. However, this condition is neither necessary nor sufficient for stability [31], but it is a fundamental practical design criterion. The pitching moment about the Y -axis can be written in this way:

$$C_M = C_{M0} + C_{M\alpha} \cdot \alpha \quad (6.3)$$

Thus, the fundamental requirements to flight in a trim condition are:

$$C_{M0} > 0 \quad C_{M\alpha} < 0 \quad (6.4)$$

In general, the choice of the CG location is taken in order to ensure a negative $C_{M\alpha}$. Thus, it is important to achieve $C_{M0} > 0$. The moment coefficient of the wing is affected by the airfoil's moment coefficient. The airfoils individuated previously for the UAV's wing are both with positive camber, so their C_{M0} are negatives. Airplanes are designed with devices to satisfy the condition $C_{M0} > 0$. For this purpose, the swept-back wing associated with a twist angle and the tail with a negative angle of attack can be used [31]. However, the twist angle was not considered in this project since it would introduce realization problems during the manufacturing process. Instead, the incidence of the V-Tail is $i_t = -1^\circ$.

$C_{M\alpha}$ depends on the relative position between the center of gravity x_{cg} and neutral point x_n of the aircraft:

$$C_{M\alpha} = C_{L\alpha} \frac{x_{cg} - x_n}{c} \quad (6.5)$$

Where the second term is the reverse of the static margin, which is defined as:

$$K_n = \frac{x_n - x_{cg}}{c} \quad (6.6)$$

The criterion to be satisfied is $C_{M\alpha} < 0$, then K_n must be > 0 , which means the center of gravity must be forward of the neutral point like Figure 6.3 shows. The more forward is the center of gravity, the greater the static stability. In general, for a conventional aircraft, the center of gravity moves during the flight since the fuel is consumed. The relative position between CG and NP has to be checked at minimum and maximum weight. Instead, the CG's position for an electric UAV does not change during the flight, so the static margin is a constant.

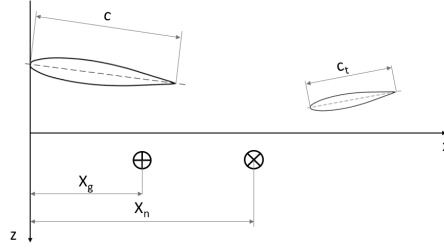


Figure 6.3. Positions of CG and NP

6.1.2 Background theory of longitudinal control

The equations of the vehicle's equilibrium may be opportunely managed to obtain the following relationships in the case of linear lift and moment about the center of gravity [31]:

$$\begin{cases} C_L = C_L|_{\delta_e=0} + C_{L\delta} \cdot \delta_e \\ C_M = C_M|_{\delta_e=0} + C_{M\delta} \cdot \delta_e \end{cases} \quad (6.7)$$

In the system of equations, δ_e is the elevator deflection. In a conventional tail, the elevator is the mobile part connected to the horizontal stabilizer. In a V-Tail configuration, the ruddervator, which can work like an elevator, is connected to a stabilizer. However, in both cases, the positive elevator rotation is achieved when it moves downward, and its deflection is indicated with δ_e . The elevator provides aerodynamic longitudinal control: when it moves, there are changes in the lift and moment coefficients.

The equations (6.7) shows that the aircraft's linear aerodynamic coefficients may be seen like a sum of different contributes. There is a part which is not affected by the elevator deflection:

$$C_L|_{\delta_e=0} = C_{L0} + C_{L\alpha} \cdot \alpha \quad (6.8)$$

$$C_M|_{\delta_e=0} = C_{M0}|_{\alpha=0} + C_{M\alpha} \cdot \alpha \quad (6.9)$$

C_{L0} is the lift coefficient developed by the aircraft during steady horizontal flight, which is different from zero since the wing is not made by a symmetry airfoil. $C_{L\alpha}$ is the aircraft's lift slope, which is positive in the linear region:

$$C_{L\alpha} = \frac{\partial C_L}{\partial \alpha} \quad (6.10)$$

In the other equation, C_{M0} is the moment coefficient at zero angle of attack, and $C_{M\alpha}$ was already defined in (6.1). The elevator effects in the equations (6.7) are supposed to be linear in δ_e . They are defined as:

$$C_{L\delta} = \frac{\partial C_L}{\partial \delta_e} > 0 \quad (6.11)$$

$$C_{M\delta} = \frac{\partial C_M}{\partial \delta_e} < 0 \quad (6.12)$$

The latter is called elevator power and it is negative since for a positive deflection of the elevator, the lift increases on the tail, and so it provides a pitching down moment.

In an equilibrium flight condition, the lift and moment coefficients are:

$$C_L = C_{L,eq} \quad C_M = 0 \quad (6.13)$$

Furthermore, in this condition the angle of attack and the elevator deflection of the aircraft are:

$$\alpha = \alpha_{eq} \quad \delta_e = \delta_{e,eq} \quad (6.14)$$

Since the equilibrium condition is supposed to be horizontal steady flight, the lift coefficient is determined from the force equilibrium in the vertical direction $L = W$:

$$C_{L,eq} = \frac{W}{\frac{1}{2}\rho V^2 S} \quad (6.15)$$

Thus, the system of equations (6.7) becomes:

$$\begin{cases} C_{L,eq} = C_{L0} + C_{L\alpha_{eq}} \cdot \alpha_{eq} + C_{L\delta} \cdot \delta_{e,eq} \\ C_{M0} + C_{M\alpha} \cdot \alpha_{eq} + C_{M\delta} \cdot \delta_{e,eq} = 0 \end{cases} \quad (6.16)$$

From the latest equations, it is possible to calculate α_{eq} and $\delta_{e,eq}$. After some mathematical operations, they are:

$$\alpha_{eq} = \frac{C_{L,eq} - C_{L0} + \frac{C_{L\delta}}{C_{M\delta}} C_{M0}}{\frac{C_{M\delta} C_{L\alpha} - C_{M\alpha} C_{L\delta}}{C_{M\delta}}} \quad (6.17)$$

$$\delta_{e,eq} = \frac{-C_{M0} - C_{M\alpha} \cdot \alpha_{eq}}{C_{M\delta}} \quad (6.18)$$

6.1.3 Longitudinal control of the UAV

Numerical grid

Figure 6.4 shows the numerical grid used in XFLR5 to calculate the aerodynamic coefficients. The mesh elements were collocated using the distribution individuated in the Chapter 4. In this case, the panel densities over wing ($p_{w,uav}$) and tail ($p_{t,uav}$) are:

$$p_{w,uav} = 1023 \text{ panels}/m^2 \quad p_{t,uav} = 1110 \text{ panels}/m^2 \quad (6.19)$$

If compared to the densities found at (5.22) and (5.23), they are larger, so the minimum condition is satisfied.

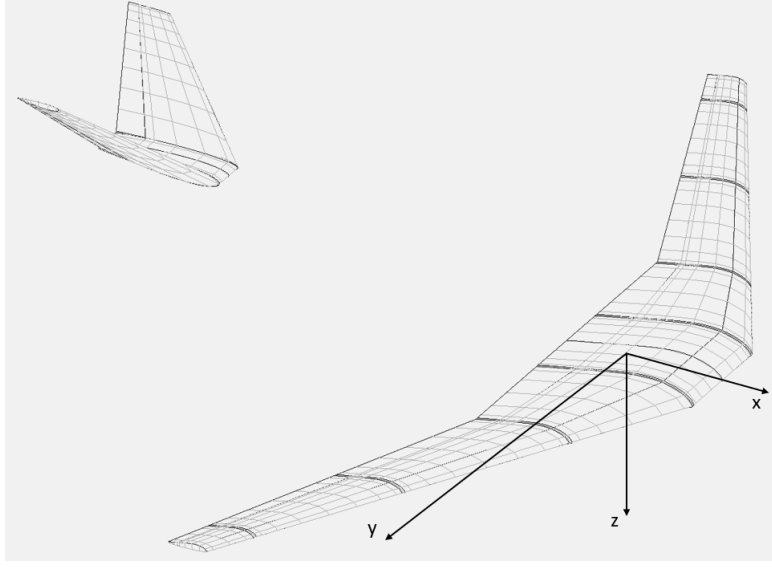


Figure 6.4. Mesh used in XFLR5 to study the UAV

Discretization with finite-difference method

In the hypothesis of small angles, and so to consider the UAV in the linear region, it is possible to determine $C_{L\alpha}$, $C_{M\alpha}$, $C_{L\delta}$, $C_{M\delta}$, α_{eq} , and $\delta_{e,eq}$ using a finite difference scheme. Thus, the derivative are defined in the following way:

$$C_{L\alpha} = \frac{C_L(\alpha = 1^\circ, \delta_e = 0^\circ) - C_{L,clean}}{\Delta\alpha} \quad (6.20)$$

$$C_{M\alpha} = \frac{C_M(\alpha = 1^\circ, \delta_e = 0^\circ) - C_{M,clean}}{\Delta\alpha} \quad (6.21)$$

$$C_{L\delta} = \frac{C_L(\alpha = 0^\circ, \delta_e = 1^\circ) - C_{L,clean}}{\Delta\delta_e} \quad (6.22)$$

$$C_{M\delta} = \frac{C_M(\alpha = 0^\circ, \delta_e = 1^\circ) - C_{M,clean}}{\Delta\delta_e} \quad (6.23)$$

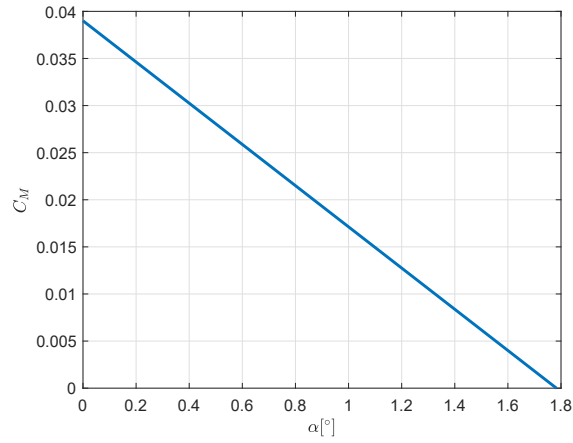
Where $\Delta\alpha$ and $\Delta\delta_e$ are respectively the unit variations of α and δ_e expressed in radians.

Results

Table 6.1 lists the obtained results. Both the airfoils satisfy the requirement in α_{eq} , where the two calculated angles are almost identical, and $\delta_{e,eq}$. However, the Gemini does not satisfy the condition $C_{M0} > 0$, but this coefficient is negative. For this reason, it requires a larger elevator deflection than the Eppler E343. The latter respects both the conditions $C_{M0} > 0$ and $C_{M\alpha} < 0$ (Figure 6.5), and its α_{eq} and $\delta_{e,eq}$ are in the desired range. It will be used for the wing.

Table 6.1. Results for the two wings

Wing airfoil	Eppler E343	Gemini
C_{L0} [1/rad]	0.299	0.300
C_{M0} [1/rad]	0.039	0.014
$C_L(\alpha = 1^\circ, \delta_e = 0^\circ)$ [1/rad]	0.388	0.389
$C_M(\alpha = 1^\circ, \delta_e = 0^\circ)$ [1/rad]	0.004	-0.020
$C_L(\alpha = 0^\circ, \delta_e = 1^\circ)$ [1/rad]	0.305	0.307
$C_M(\alpha = 0^\circ, \delta_e = 1^\circ)$ [1/rad]	0.011	-0.014
$C_{L\alpha}$ [1/rad]	5.099	5.099
$C_{M\alpha}$ [1/rad]	-2.005	-1.948
$C_{L\delta}$ [1/rad]	0.344	0.401
$C_{M\delta}$ [1/rad]	-1.588	-1.604
α_{eq} [°]	1.783	1.853
$\delta_{e,eq}$ [°]	-0.834	-1.750

Figure 6.5. $C_{M\alpha}$ for the wing made of E343 airfoil

6.2 Lateral aerodynamic

In the previous section, the longitudinal aerodynamic of the UAV was analyzed considering $C_{L\alpha}$, $C_{M\alpha}$, and the elevator's effects on the longitudinal stability. Now, the vehicle's lateral dynamic is analyzed considering the sideslip angle β . Thus, the derivatives investigated are $C_{y\beta}$, $C_{l\beta}$, and $C_{n\beta}$.

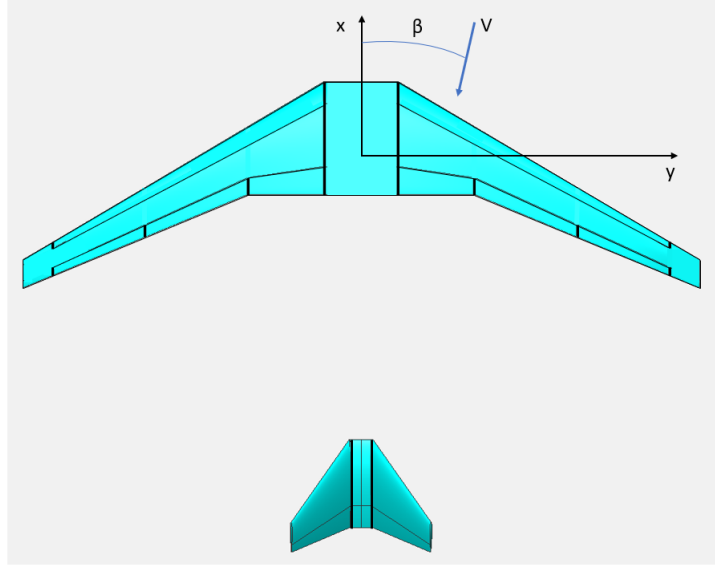


Figure 6.6. Sideslip angle $\beta > 0$

Figure 6.6 shows a positive rotation for the sideslip angle, and the velocity is outside of the symmetry plane. The derivatives for the generic coefficient C_k are calculated considering a unit variation of sideslip angle. They are evaluated at $\alpha = 0^\circ$, so this indication will be omitted.

$$C_{k\beta} = \frac{\partial C_k}{\partial \beta} = \frac{C_k(\beta = 1^\circ) - C_{k, \text{clean}}}{\Delta \beta} \quad (6.24)$$

Where $\Delta \beta$ is the unit variation of sideslip angle expressed in radians. The calculated derivatives are listed in Table 6.2.

Table 6.2. Sideslip derivatives

Derivative	Expected sign	Value [1/rad]
$C_{y\beta}$	< 0	-0.206
$C_{l\beta}$	< 0	-0.059
$C_{n\beta}$	> 0	0.109

$$C_{y\beta} = \frac{\partial C_y}{\partial \beta} \quad (6.25)$$

The first derivative is the variation of sideforce along the Y -axis for a positive sideslip angle. The main contributions come from tail and fuselage. The wing contribution is smaller than the first two. However, the body is not simulated in XFLR5, so the found value represents only the tail effect. Furthermore, it is a damping derivative: when there is a sideslip angle, a force rises on the aircraft which tends to reduce the sideslip angle. Finally, this derivative has low effect on the dynamics of the vehicle.

$$C_{l\beta} = \frac{\partial C_l}{\partial \beta} \quad (6.26)$$

The dihedral effect $C_{l\beta}$ is affected by different contributions: in first place the wing, with its dihedral angle, aspect ratio and sweep, the fuselage, not considered in XFLR5, and tail. The calculated value in XFLR5 is due only by sweep angle, tip vortexes, and tail. The dihedral effect is a damping derivative and it is more important than the first one.

$$C_{n\beta} = \frac{\partial C_n}{\partial \beta} \quad (6.27)$$

The yaw stiffness derivative $C_{n\beta}$ is also known as directional stability. Its positive value implies that if a perturbation in β occurs, the UAV will produce a restoring yawing moment that tends to reduce the sideslip angle. In this case, the main contributions are given by fuselage and tail. Also in this case, the body's effect is neglected.

6.3 Control derivatives

The concepts of control effectors and control deflections can be helpful to indicate the different ways to work of the control surfaces. The control effectors are all the external devices that can be used to change forces and moments acting on the plane. For example, a command given by the pilot is a control effector.

Considering a positive roll (δ_a^a) command given by the pilot, it is the control effector acting on the airplane's control surfaces. The subscript indicates that the control surface is usually employed as ailerons. Instead, the superscript indicates that it moves asymmetrically. At the pilot's command, the asymmetric deflections of the ailerons correspond. Each deflection is a control deflection, and they can be denoted by using the convention proposed in [1]:

$$\delta_{ra} \quad \delta_{la} \quad (6.28)$$

Where r and l indicate the physical position of the control surface respect the UAV's symmetry plane, and a indicates the primary control effector which the surface is usually used for during the flight, in this example ailerons. Assuming a control effectors given by the pilot of $\delta_a^a = +2^\circ$, the control deflections on the aileron's surfaces are:

$$\delta_{ra} = +2^\circ \quad \delta_{la} = -2^\circ \quad (6.29)$$

In such a case, the control effector is:

$$\delta_a^a = \frac{\delta_{ra} - \delta_{la}}{2} = 2^\circ \quad (6.30)$$

However, the ailerons might work as flaps. In that case, the control effector is indicated with δ_a^f . The subscript a indicates the nominal operation condition of the control surface (ailerons), and the superscript f means that they are working as flaps rather than as ailerons. Thus, the control effector is:

$$\delta_a^f = \frac{\delta_{ra} + \delta_{la}}{2} \quad (6.31)$$

The relationships (6.30) and (6.31) can be written in the matricial form:

$$\begin{Bmatrix} \delta_a^a \\ \delta_a^f \end{Bmatrix} = \begin{bmatrix} 1/2 & -1/2 \\ 1/2 & 1/2 \end{bmatrix} \begin{Bmatrix} \delta_{ra} \\ \delta_{la} \end{Bmatrix} \quad (6.32)$$

The relationship (6.32) shows the link between control effectors $\{\delta_a^a \ \delta_a^f\}^T$, and control deflections $\{\delta_{ra} \ \delta_{la}\}^T$, which is given by an invertible matrix. Using the Figure 6.7, the UAV's control effectors are:

$$\begin{aligned} \delta_a^a &= \frac{\delta_{ra} - \delta_{la}}{2} & \delta_a^f &= \frac{\delta_{ra} + \delta_{la}}{2} \\ \delta_{f1}^a &= \frac{\delta_{rf1} - \delta_{lf1}}{2} & \delta_{f1}^f &= \frac{\delta_{rf1} + \delta_{lf1}}{2} \\ \delta_{f2}^a &= \frac{\delta_{rf2} - \delta_{lf2}}{2} & \delta_{f2}^f &= \frac{\delta_{rf2} + \delta_{lf2}}{2} \\ \delta_t^a &= \frac{\delta_{lt} - \delta_{rt}}{2} & \delta_t^e &= \frac{\delta_{rt} + \delta_{lt}}{2} \\ \delta_s^s &= \frac{\delta_{llef} + \delta_{rlef}}{2} \end{aligned}$$

In every case, the following finite-difference scheme is employed to calculate the control derivatives:

$$C_{k(\delta_{cs})} = \frac{\partial C_k}{\partial \delta_{cs}} = \frac{C_k(\delta_{cs} = 1^\circ) - C_{k, clean}}{\Delta \delta_{cs}} \quad (6.33)$$

The derivatives for the generic coefficient C_k are calculated considering a unit deflection of the control surface δ_{cs} , and $\Delta \delta_{cs}$ is the unit variation expressed in radians. The values $C_k(\delta_{cs} = 1^\circ)$ and $C_{k, clean}$ are given by XFLR5. All the next figures show larger positive deflections of the control surfaces to provide a clear view.

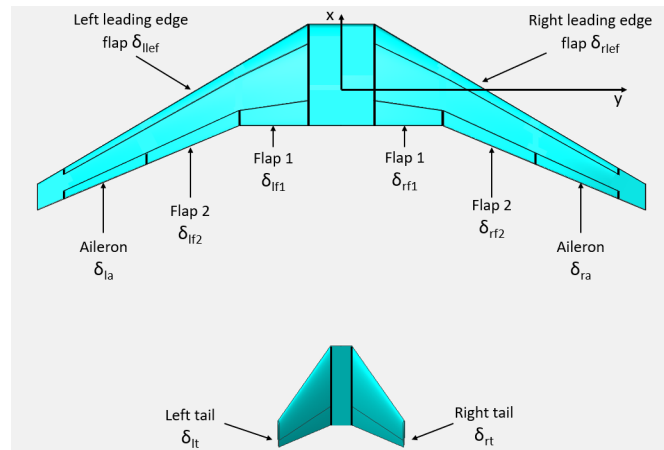


Figure 6.7. Control surfaces definition

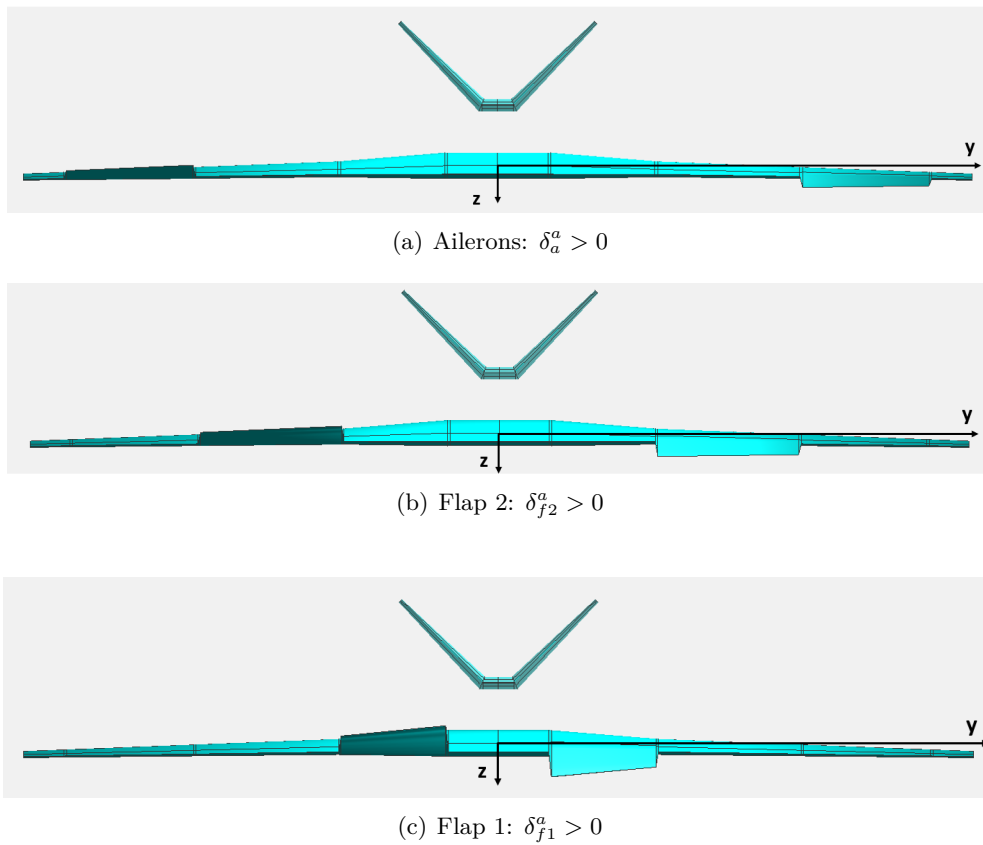
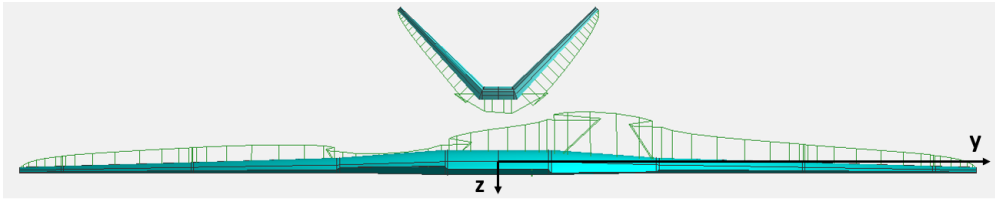


Figure 6.8. Positive aileron deflections

Table 6.3. Derivatives due to ailerons deflections

Derivative	Expected sign	Value [1/rad]
$C_{y(\delta_a^a)}$	< 0	0.008
$C_{y(\delta_{f2}^a)}$	< 0	0.021
$C_{y(\delta_{f1}^a)}$	< 0	0.049
$C_{l(\delta_a^a)}$	< 0	-0.170
$C_{l(\delta_{f2}^a)}$	< 0	-0.183
$C_{l(\delta_{f1}^a)}$	< 0	-0.081
$C_{n(\delta_a^a)}$	> 0	-0.003
$C_{n(\delta_{f2}^a)}$	> 0	-0.010
$C_{n(\delta_{f1}^a)}$	> 0	-0.022

Figure 6.9. Lift distribution: $\delta_{f1}^a > 0$

6.3.1 Ailerons deflections

The derivatives C_y and C_n are less important than the main effect of the ailerons, expressed by the derivative C_l . The positive roll is in the clockwise direction from the view behind the UAV (Figure 6.8). When the right control surface moves downward, it is subjected to an increase in lift, while the left one's lift decreases. This differential lift causes the vehicle to roll in the counterclockwise direction, in the opposite direction than the reference system. In general, the differential lift is associated with a drag differential between the two semi span wings, which is responsible for a positive nose-right yawing moment. This phenomenon is known as aileron-adverse yaw: the yawing moment acts clockwise about the Z -axis, considering that ailerons undergo a positive deflection when the airplane needs to start a turning to the left. Instead, the results obtained in XFLR5 indicates that the derivatives C_y and C_n are opposite than the expected signs. In the case of deflections of the ailerons, the results are close to zero, and so they are negligible. They increase in the cases of flap-one and flap-two working as ailerons. It may be imputed to the downwash effect on the tail. In the case of flap-one works like an aileron, the computed values of

C_y and C_n are more significant. The flap-one is in front of the V-Tail: it could cause a downwash on it, which would manifest an increase in the magnitude of the angle of attack for the right tail and a decrease for the left one. Thus, it determines an increase in the differential lift projected along the Y-axis in the positive direction of the reference body system. Figure 6.9 shows this effect. Also, it gives a negative yawing moment, and the aileron-adverse yaw is not found. However, these results are obtained by solving the flow potential without considering the pressure and viscous drag. A CFD analysis solving the RANS equations would provide more accurate results accounting those effects by providing or not the validation of the results obtained for C_y and C_n .

6.3.2 Symmetryc deflections

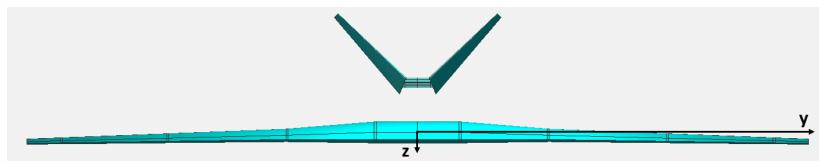
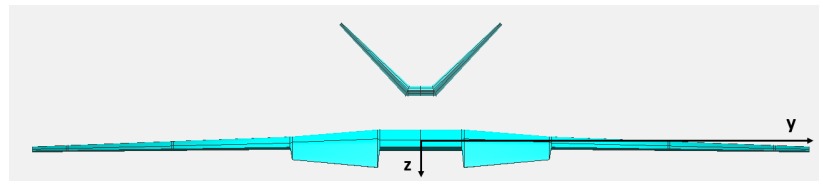
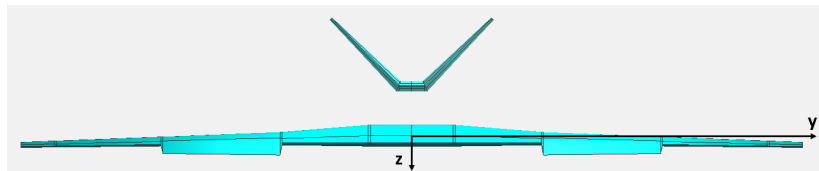


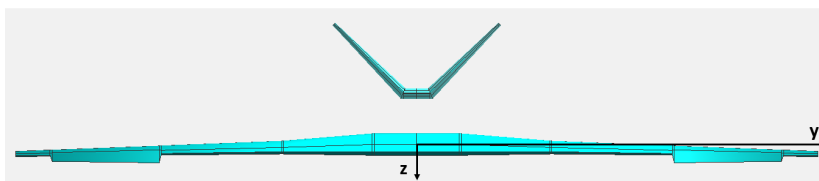
Figure 6.10. Elevator: $\delta_t^e > 0$



(a) Flap 1: $\delta_{f1}^f > 0$



(b) Flap 2: $\delta_{f2}^f > 0$



(c) Ailerons: $\delta_a^f > 0$

Figure 6.11. Positive flap deflections

Table 6.4. Derivatives due to symmetric deflections

Derivative	Expected sign	Value [1/rad]
$C_L(\delta_t^e)$	> 0	0.277
$C_L(\delta_{f1}^f)$	> 0	0.817
$C_L(\delta_{f2}^f)$	> 0	0.782
$C_L(\delta_a^f)$	> 0	0.411
$C_M(\delta_t^e)$	< 0	-1.588
$C_M(\delta_{f1}^f)$	< 0	0.202
$C_M(\delta_{f2}^f)$	< 0	-0.302
$C_M(\delta_a^f)$	< 0	-0.461

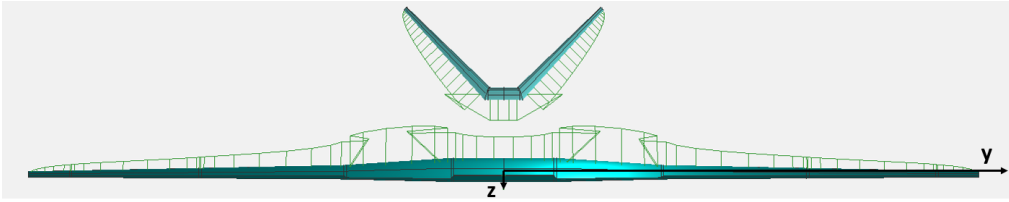
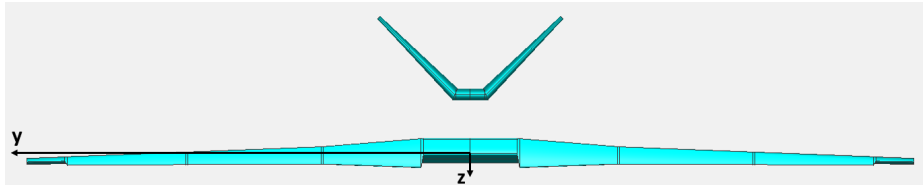
Figure 6.12. Lift distribution: $\delta_{f1}^f > 0$

Figure 6.10 shows the positive deflection of the elevator: both the ruddervators move downward. Instead, the positive deflections of the flap are shown in Figure 6.11. As previously analyzed, when the elevator is subjected to a positive deflection, there is an increase in the lift of the UAV. It is linked to a negative pitching moment. $C_{M(\delta_t^e)}$ is known as elevator power and represents the capacity of the elevator to change the UAV's equilibrium condition. The flaps and ailerons' effects on the UAV's lift coefficient are more significant than the elevator's influence since the latter is smaller if compared in terms of the surface to the others. Instead, the elevator's influence on the pitching moment is the largest since the elevator has a higher arm respecting the center of gravity of the UAV. Almost all the results are in line with the expected signs, less than the effect of flap one on the pitching moment. This aspect can be explained considering the downwash on the tail, which causes an increase of the tail's lift. It provides a positive variation of the moment coefficient since the tail has a negative incidence. Finally, also, in this case, a CFD investigation would provide more reliable results.

Figure 6.13. Leading edge flap $\delta_s^s > 0$

6.3.3 Leading edge flaps

Figure 6.13 shows the symmetric deflections of the leading edge flaps. However, the leading edge flap does not affect the variations of lift with the angle of attack [32], and they are used to postpone the stall at higher angles of attack. Thus, the found values derive from the numerical method's approximations. For a more accurate analysis of this type of device or the slats, the CFD or experimental test can provide more realistic results. Furthermore, the effects of slats on the aerodynamic coefficients can be studied only with the CFD considering the boundary layer, so the viscosity's effects, since that kind of device acts on the boundary layer.

6.3.4 Rudder deflection

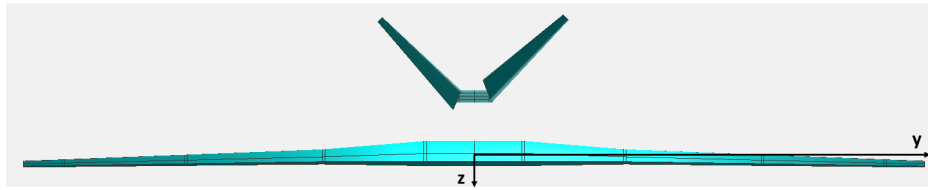


Figure 6.14. Rudder $\delta_r^t > 0$

Table 6.5. Derivatives due to rudder deflection

Derivative	Expected value	Value [1/rad]
$C_{y(\delta_r^t)}$	> 0	0.202
$C_{n(\delta_r^t)}$	< 0	-0.108

A positive deflection of the rudder, which means left ruddervator down and right ruddervator up, causes a differential lift along the positive direction of the Y -axis. It moves the UAV's nose on the left. The derivative $C_{n(\delta_r^t)}$ is also known as rudder power.

Chapter 7

CAD of the UAV

Along the design process, it was decided to make a CAD of the UAV. All the components were drawn considering the previously calculated dimensions listed in Table 2.3, using Solidworks and Catia. The cad could be used for more accurate CFD using ANSYS Fluent or STAR-CCM+. The livery was done with Adobe Photoshop.



Figure 7.1. Render of the UAV

Conclusions

The goal of the present thesis was to design a UAV whose wing was similar, in geometry and the type of control surfaces, to the most employed aircraft in the continental flights from 2000 to 4000 *NM* range. The design process started with setting the requirements in terms of cruise speed, control surfaces, dimensions, weights, and tail configuration. The cruise speed was selected at 20 *m/s*. This value was chosen considering the ability of UCR SkyTeam's pilot.

The UAV wingspan was firstly decided, and knowing the mean geometry characteristics of the identified aircraft (B737, A320, A321, ...), all the UAV's dimensions were calculated using some mathematical proportions. The first guess distance between V-Tail and wing leading edge was calculated in the same way. The control surfaces located on the wing trailing edge are flap-one, closer to the fuselage, flap-two in the middle section of the wing, and aileron. All of these surfaces are not the standard flaps and ailerons, but thanks to the hinge connection, they might work as ailerons instead of flaps or ailerons rather than flaps. On the leading edge, a slat is placed. The tail is equipped with the ruddervators, which can work as a rudder or elevator.

Some decisions were taken to simplify and reduce the UAV's manufacturing costs: one unique airfoil, and reuse of the avionics employed on the other UCR SkyTeam's UAVs. The inertial properties were determined thanks to the knowledge of the required components, avionics, and structure onboard the flight vehicle.

To chose the wing's airfoil, a two-dimensional aerodynamic study was performed. Firstly, the UAV aerodynamic problem was compared to the real-sized aircraft using the Reynolds and Mach numbers showing the differences. A background theory about the laminar separation bubble was given since the UAV's Reynolds spans from about $8 \cdot 10^4$ at the wingtip to more than $3.5 \cdot 10^5$. To choose the wing's airfoil and visualize this phenomenon, the two-dimensional CFD was performed using the transitional RANS model $k - kl - \omega$ in ANSYS Fluent. Since the limited computational resources available, the airfoils were studied in the linear region for small attack angles using a steady-state approach following indications found in the literature. This approach is acceptable for designing the UAV at the nominal cruise condition, where the flight angle of attack is about 2° . Before analyzing the different airfoils, a test case was performed to do the mesh independence study and find the more appropriate settings to study the airfoils at the mean aerodynamic chord-based Reynolds. The results were validated with the experiments carried on by the University of Illinois at Urbana-Champaign [25]. The selected airfoils were five, and they were individuated considering the constraint of about 15% thickness. Also, they

are optimized for the low to moderate Reynolds range. They may be divided into two families: semi-symmetrical and with a small reflection closed to the trailing edge to reduce the airfoil's negative pitching moment. The obtained results from the CFD in Fluent were the lift, drag, and moment coefficients. For both the type of airfoil, the airfoil with the highest effectiveness was selected for further studies considering the longitudinal static stability.

The longitudinal, lateral, and control derivatives were studied using the free, open-source software XFLR5. This tool's results were validated with experimental results from a wind tunnel investigation performed on another UCR SkyTeam's UAV. Unfortunately, only the aerodynamic coefficients of lift, drag, and moment were available. Thus, it was showed the capacity of the vortex lattice method to predict the aerodynamic characteristics for small angles of attack where the viscous effects are negligible.

In the longitudinal aerodynamic section, two different wings made by the two different airfoils were compared. The wing made by the Eppler E343 was chosen since it permits the smallest angle of attack, and the smallest elevator deflection was chosen. The UAV can fly at $\alpha_{eq} = 1.783^\circ$ with an elevator deflection of $\delta_{e,eq} = -0.834^\circ$. It is statically stable longitudinally, and $C_{M\alpha} = -2.00 \text{ 1/rad}$.

The lateral aerodynamic investigated the UAV behavior in the presence of a sideslip angle. The derivatives were calculated using a finite difference scheme, and all of them satisfied the expected sign. In particular, $C_{y\beta}$ and the dihedral effect $C_{l\beta}$ are negative. Also, the yaw stiffness $C_{n\beta}$ is positive.

The control derivatives quantified the effects of different control effectors in the control of the UAV. They were calculated using a finite difference scheme. When the control surfaces act as ailerons, they are subjected to asymmetric deflections. In this case, the most crucial derivative is $C_{l(\delta^a)}$, which is negative for all the cases as expected. Flap-one is located close to the fuselage, and it has the lowest arm from the CG: for this reason, its contribution is lower than the other flap and the aileron. For a deflection of this surface as ailerons, the force derivative along the Y -axis is the highest and positive. Moreover, the associated derivative $C_{n(\delta^a)}$ is negative instead of positive. Thus, there is not any aileron-adverse yaw. It happens because the control surfaces deflection induces a downwash on the tail, causing a positive differential lift directed along the positive Y -axis. The magnitude of this phenomenon decreases while using a control surface with increasing arms from the reference system's origin. However, this behavior would need more investigation since the VLM does not consider the parasite drag, which modifies the flow over the UAV. Only a CFD analysis would verify this behavior.

Later, the effects of symmetrical deflections were analyzed for both the wing and tail. Every symmetrical deflection is associated with a positive increase of the lift coefficient. Instead, considering the pitching moment variations, the highest contribution is given by the elevator power. The ailerons and the flaps-two have a negative effect on the pitching moment for a positive deflection. The flap close to the fuselage generates a positive moment coefficient about the center of gravity. It can be explained considering the downwash on the tail, which increases the lift on it. The tail has a negative incidence and produces a positive pitching moment about the center of gravity.

Finally, the CAD of the aircraft was done. It will help to perform a more proper investigation about the UAV's aerodynamic and control derivatives, considering the fuselage, and solving the RANS based CFD in ANSYS Fluent or STAR-CCM+. More accurate CFD will also allow investigating the stall velocity of the aircraft, the downwash effect on the tail, and the effects of the parasite drag on the control derivatives. However, previous control systems were designed using this software [1]. Furthermore, the experimental flight test performed at the UCR SkyTeam showed that the controller developed by Baggi works well. It means that the aerodynamic coefficients and control derivatives obtained in XFLR5 are trusted as input.

In conclusion, the obtained results indicated that the UAV is statically stable longitudinally, directionally stable, and the control surfaces can maneuver it. The UAV configuration seems to avoid the aileron-adverse yaw, but further investigations are needed. The calculated values for the derivatives in this thesis represent the starting point for more detailed CFD analyses and the control engineer who will develop the control system.

Appendix A

Aerodynamic and control derivatives

Tables from A.1 to A.11 collect the results obtained for $\alpha = -6^\circ \div 9^\circ$ and $\beta = 0^\circ \div 10^\circ$. Tables from A.12 to A.20 collect the data obtained from simulations with deflections of the control surfaces. From Table A.21 to A.25 the aerodynamic and control derivatives are collected. They are calculated following the finite-difference scheme:

$$C_k(\delta) = \frac{\partial C_k}{\partial \delta} = \frac{C_k(\delta = 1^\circ) - C_k(\delta = 0^\circ)}{\Delta\delta} \quad (\text{A.1})$$

Where δ is the generic control surface deflection, and $\Delta\delta$ is the unit variation in radians. The derivatives are calculated for $\alpha = -6^\circ \div 9^\circ$ and $\beta = 0^\circ$ in the body axes reference system.

Table A.1. $\alpha = -6^\circ \div 9^\circ$ and $\beta = 0^\circ$

α [°]	β [°]	CL	CDi	CDv	CD	CY	Cl	Cm	Cn	Cni	QInf	XCP
-6	0	-0.235325	0.003559	0.029482	0.033041	0	0	0.241286	0	0	20	0.4095
-5	0	-0.146361	0.002156	0.021942	0.024098	0	0	0.208377	0	0	20	0.4893
-4	0	-0.057277	0.001276	0.017171	0.018447	0	0	0.175065	0	0	20	0.8176
-3	0	0.031871	0.000923	0.015761	0.016684	0	0	0.141369	0	0	20	-0.6913
-2	0	0.121029	0.001099	0.01531	0.016408	0	0	0.107358	0	0	20	0.0229
-1	0	0.210142	0.001803	0.015832	0.017635	0	0	0.073058	0	0	20	0.1312
0	0	0.299156	0.003035	0.016313	0.019347	0	0	0.038547	0	0	20	0.1751
1	0	0.388014	0.004791	0.016814	0.021605	0	0	0.003865	0	0	20	0.1988
2	0	0.476664	0.007067	0.017103	0.02417	0	0	-0.030948	0	0	20	0.2138
3	0	0.565051	0.009857	0.017471	0.027328	0	0	-0.065861	0	0	20	0.2241
4	0	0.653121	0.013153	0.01779	0.030943	0	0	-0.100843	0	0	20	0.2317
5	0	0.740821	0.016945	0.018226	0.035171	0	0	-0.135848	0	0	20	0.2375
6	0	0.828097	0.021223	0.018792	0.040016	0	0	-0.170835	0	0	20	0.2422
7	0	0.914899	0.025975	0.019493	0.045468	0	0	-0.205769	0	0	20	0.246
8	0	1.001175	0.031187	0.020314	0.051501	0	0	-0.240612	0	0	20	0.2492
9	0	1.086874	0.036844	0.021307	0.058151	0	0	-0.275335	0	0	20	0.252

Table A.2. $\alpha = -6^\circ \div 9^\circ$ and $\beta = 1^\circ$

α [°]	β [°]	CL	CDi	CDv	CD	CY	Cl	Cm	Cn	Cni	QInf	XCP
-6	1	-0.23447	0.003264	0.029481	0.032746	-0.00419	-0.00056	0.22627	0.002222	0.002194	20	0.401
-5	1	-0.14545	0.001984	0.02194	0.023924	-0.00396	-0.00063	0.19714	0.00214	0.002119	20	0.4794
-4	1	-0.05641	0.001192	0.017171	0.018362	-0.00379	-0.0007	0.166705	0.002075	0.002051	20	0.8039
-3	1	0.032554	0.000897	0.01576	0.016657	-0.00367	-0.00077	0.135225	0.002016	0.001993	20	-0.6418
-2	1	0.12132	0.001108	0.015308	0.016416	-0.00359	-0.00086	0.103149	0.00197	0.001944	20	0.0296
-1	1	0.209777	0.001828	0.015832	0.01766	-0.00357	-0.00095	0.070691	0.00193	0.001905	20	0.1337
0	1	0.297812	0.003061	0.016312	0.019373	-0.0036	-0.00104	0.038113	0.001901	0.001876	20	0.1761
1	1	0.385309	0.004806	0.016813	0.021619	-0.00368	-0.00113	0.005601	0.001882	0.001857	20	0.1992
2	1	0.472154	0.007064	0.017103	0.024167	-0.00381	-0.00123	-0.02666	0.001874	0.001849	20	0.2138
3	1	0.558232	0.009832	0.017466	0.027299	-0.00399	-0.00132	-0.05848	0.001877	0.00185	20	0.2238
4	1	0.643426	0.013106	0.017791	0.030897	-0.00422	-0.00142	-0.08967	0.00189	0.001862	20	0.231
5	1	0.727621	0.01688	0.018227	0.035107	-0.0045	-0.00151	-0.12001	0.001914	0.001884	20	0.2365
6	1	0.810702	0.021143	0.018794	0.039937	-0.00484	-0.00161	-0.1493	0.001948	0.001915	20	0.2408
7	1	0.892552	0.025879	0.019495	0.045374	-0.00522	-0.00169	-0.1773	0.001991	0.001955	20	0.2442
8	1	0.973011	0.030962	0.020316	0.051278	-0.00565	-0.00178	-0.20368	0.00204	0.002001	20	0.2469
9	1	1.052199	0.036626	0.021309	0.057935	-0.0061	-0.00186	-0.22903	0.00208	0.002037	20	0.2492

Table A.3. $\alpha = -6^\circ \div 9^\circ$ and $\beta = 2^\circ$

$\alpha = -6^\circ \div 9^\circ - \beta = 2^\circ$												
α [°]	β [°]	CL	CDi	CDv	CD	CY	Cl	Cm	Cn	Cni	QInf	XCP
-6	2	-0.23408	0.003353	0.029484	0.032837	-0.00837	-0.00113	0.224842	0.004442	0.004384	20	0.3998
-5	2	-0.14514	0.002067	0.021945	0.024011	-0.00793	-0.00126	0.195739	0.004275	0.004233	20	0.4777
-4	2	-0.05618	0.001272	0.017171	0.018444	-0.00758	-0.0014	0.165315	0.004145	0.004099	20	0.8007
-3	2	0.032708	0.000977	0.015757	0.016734	-0.00733	-0.00155	0.133857	0.004028	0.003983	20	-0.6285
-2	2	0.121399	0.001187	0.015305	0.016491	-0.00719	-0.00172	0.101808	0.003935	0.003885	20	0.0321
-1	2	0.209782	0.001906	0.015829	0.017735	-0.00714	-0.00189	0.069372	0.003856	0.003807	20	0.135
0	2	0.297744	0.003138	0.01631	0.019448	-0.00719	-0.00208	0.036813	0.003797	0.003748	20	0.177
1	2	0.385171	0.004882	0.016811	0.021693	-0.00735	-0.00226	0.004312	0.003761	0.00371	20	0.1999
2	2	0.471947	0.007138	0.017096	0.024234	-0.00761	-0.00246	-0.02795	0.003744	0.003693	20	0.2143
3	2	0.557958	0.009904	0.017459	0.027363	-0.00797	-0.00265	-0.05978	0.00375	0.003696	20	0.2242
4	2	0.643088	0.013175	0.017783	0.030958	-0.00843	-0.00284	-0.09098	0.003776	0.00372	20	0.2314
5	2	0.72722	0.016943	0.018223	0.035166	-0.009	-0.00303	-0.12135	0.003823	0.003763	20	0.2369
6	2	0.810241	0.021201	0.018788	0.039989	-0.00967	-0.00322	-0.15067	0.003891	0.003826	20	0.2411
7	2	0.89204	0.025939	0.019484	0.045423	-0.01044	-0.0034	-0.17875	0.003977	0.003906	20	0.2445
8	2	0.972655	0.031162	0.020302	0.051464	-0.01131	-0.00357	-0.20602	0.004082	0.004004	20	0.2473
9	2	1.063395	0.033961	0.021312	0.055274	-0.01524	-0.00384	-0.28357	0.005618	0.005532	20	0.259

Table A.4. $\alpha = -6^\circ \div 9^\circ$ and $\beta = 3^\circ$

α [°]	β [°]	CL	CDi	CDv	CD	CY	Cl	Cm	Cn	Cni	QInf	XCP
-6	3	-0.23344	0.00349	0.029484	0.032974	-0.01254	-0.00171	0.222461	0.006654	0.006567	20	0.3978
-5	3	-0.14463	0.002201	0.021943	0.024144	-0.01188	-0.0019	0.193399	0.006403	0.006341	20	0.4748
-4	3	-0.05579	0.001404	0.017179	0.018583	-0.01136	-0.00211	0.163013	0.006208	0.00614	20	0.7952
-3	3	0.032964	0.001108	0.015756	0.016864	-0.01099	-0.00234	0.131587	0.006032	0.005965	20	-0.6067
-2	3	0.12153	0.001317	0.015301	0.016618	-0.01077	-0.00259	0.099581	0.005894	0.005819	20	0.0362
-1	3	0.20979	0.002035	0.015824	0.017859	-0.0107	-0.00285	0.067181	0.005775	0.005701	20	0.1372
0	3	0.297632	0.003265	0.016305	0.019571	-0.01078	-0.00313	0.034652	0.005687	0.005613	20	0.1785
1	3	0.384941	0.005008	0.016803	0.021811	-0.01101	-0.00341	0.002166	0.005631	0.005556	20	0.201
2	3	0.471602	0.007262	0.017088	0.02435	-0.01139	-0.0037	-0.03009	0.005606	0.005529	20	0.2152
3	3	0.557502	0.010025	0.017451	0.027476	-0.01193	-0.00398	-0.06193	0.005613	0.005534	20	0.2249
4	3	0.642524	0.01329	0.017774	0.031064	-0.01263	-0.00427	-0.09315	0.005653	0.005569	20	0.232
5	3	0.726553	0.017052	0.01821	0.035262	-0.01348	-0.00456	-0.12356	0.005723	0.005633	20	0.2374
6	3	0.809472	0.0213	0.018775	0.040075	-0.01448	-0.00484	-0.15294	0.005823	0.005726	20	0.2416
7	3	0.891166	0.026023	0.019466	0.045489	-0.01563	-0.00511	-0.18107	0.005953	0.005846	20	0.245
8	3	0.971451	0.031439	0.020281	0.051172	-0.01692	-0.00536	-0.20743	0.006105	0.005988	20	0.2476
9	3	1.050194	0.03707	0.021266	0.058336	-0.01817	-0.0056	-0.23075	0.006187	0.006059	20	0.2494

Table A.5. $\alpha = -6^\circ \div 9^\circ$ and $\beta = 4^\circ$

α [°]	β [°]	CL	CDi	CDv	CD	CY	Cl	Cm	Cn	Cni	QInf	XCP
-6	4	-0.23254	0.003672	0.029477	0.033148	-0.01671	-0.0023	0.21913	0.008856	0.008739	20	0.3951
-5	4	-0.14392	0.002381	0.021937	0.024318	-0.01582	-0.00255	0.190126	0.008521	0.008438	20	0.4707
-4	4	-0.05526	0.001585	0.01719	0.018775	-0.01513	-0.00283	0.159802	0.00826	0.00817	20	0.7875
-3	4	0.033321	0.001289	0.015764	0.017053	-0.01464	-0.00314	0.128437	0.008026	0.007937	20	-0.5768
-2	4	0.121712	0.001497	0.015296	0.016793	-0.01434	-0.00347	0.096479	0.007842	0.007741	20	0.042
-1	4	0.2098	0.002215	0.015819	0.018034	-0.01424	-0.00382	0.064132	0.007683	0.007584	20	0.1403
0	4	0.297473	0.003444	0.016294	0.019738	-0.01435	-0.00419	0.031639	0.007565	0.007466	20	0.1805
1	4	0.384617	0.005184	0.016791	0.021975	-0.01465	-0.00456	-0.00082	0.007489	0.007389	20	0.2025
2	4	0.471117	0.007435	0.017078	0.024514	-0.01517	-0.00495	-0.03307	0.007455	0.007354	20	0.2164
3	4	0.556861	0.010194	0.017443	0.027637	-0.01588	-0.00533	-0.06491	0.007464	0.007359	20	0.2259
4	4	0.641732	0.013455	0.017762	0.031217	-0.0168	-0.00572	-0.09617	0.007516	0.007404	20	0.2329
5	4	0.725616	0.01721	0.018192	0.035402	-0.01793	-0.0061	-0.12663	0.007608	0.007489	20	0.2382
6	4	0.808396	0.021446	0.018753	0.040199	-0.01926	-0.00647	-0.15609	0.007741	0.007612	20	0.2423
7	4	0.889958	0.02614	0.019443	0.045583	-0.0208	-0.00683	-0.18433	0.007913	0.007772	20	0.2456
8	4	0.97042	0.03117	0.020255	0.051424	-0.02257	-0.00719	-0.21209	0.008125	0.00797	20	0.2485
9	4	1.055273	0.036576	0.021256	0.057832	-0.02577	-0.00768	-0.26234	0.008906	0.008734	20	0.2551

A – Aerodynamic and control derivatives

Table A.6. $\alpha = -6^\circ \div 9^\circ$ and $\beta = 5^\circ$

α [°]	β [°]	CL	CDi	CDv	CD	CY	Cl	Cm	Cn	Cni	QInf	XCP
-6	5	-0.2314	0.003895	0.029458	0.033353	-0.02086	-0.00291	0.214854	0.011043	0.010896	20	0.3915
-5	5	-0.143	0.002607	0.021927	0.024535	-0.01976	-0.00322	0.185939	0.010624	0.01052	20	0.4654
-4	5	-0.05458	0.001813	0.017203	0.019016	-0.01889	-0.00358	0.155694	0.010298	0.010186	20	0.7774
-3	5	0.033778	0.001518	0.015777	0.017295	-0.01827	-0.00396	0.124412	0.010005	0.009895	20	-0.5396
-2	5	0.121944	0.001727	0.015297	0.017024	-0.0179	-0.00438	0.092525	0.009775	0.00965	20	0.0493
-1	5	0.20981	0.002444	0.015811	0.018255	-0.01777	-0.00481	0.060236	0.009576	0.009452	20	0.1441
0	5	0.297266	0.003671	0.016279	0.01995	-0.0179	-0.00527	0.027794	0.009427	0.009305	20	0.1831
1	5	0.384198	0.005409	0.016776	0.022186	-0.01828	-0.00574	-0.00463	0.009332	0.009208	20	0.2044
2	5	0.470492	0.007657	0.017067	0.024724	-0.01892	-0.00622	-0.03685	0.009287	0.009161	20	0.2179
3	5	0.556035	0.010412	0.017431	0.027843	-0.01981	-0.0067	-0.06871	0.009298	0.009166	20	0.2272
4	5	0.640712	0.013668	0.017747	0.031414	-0.02095	-0.00719	-0.10001	0.00936	0.009222	20	0.234
5	5	0.724409	0.017418	0.018171	0.035589	-0.02235	-0.00766	-0.13054	0.009474	0.009326	20	0.2392
6	5	0.807004	0.021664	0.018726	0.04039	-0.02401	-0.00813	-0.1601	0.009638	0.009478	20	0.2432
7	5	0.888391	0.026353	0.019413	0.045766	-0.02592	-0.00858	-0.1884	0.00985	0.009674	20	0.2464
8	5	0.968251	0.031476	0.020231	0.051708	-0.02809	-0.00901	-0.21474	0.010106	0.009912	20	0.2489
9	5	1.051375	0.037091	0.021225	0.058316	-0.03114	-0.00958	-0.25776	0.010749	0.010533	20	0.2542

Table A.7. $\alpha = -6^\circ \div 9^\circ$ and $\beta = 6^\circ$

α [°]	β [°]	CL	CDi	CDv	CD	CY	Cl	Cm	Cn	Cni	QInf	XCP
-6	6	-0.23	0.00416	0.029438	0.033599	-0.025	-0.00354	0.20966	0.013212	0.013036	20	0.3871
-5	6	-0.14189	0.002878	0.021914	0.024791	-0.02367	-0.00392	0.180849	0.01271	0.012585	20	0.459
-4	6	-0.05374	0.002087	0.017222	0.019309	-0.02263	-0.00434	0.15071	0.012319	0.012184	20	0.7649
-3	6	0.034332	0.001794	0.015792	0.017587	-0.02189	-0.0048	0.119526	0.011967	0.011835	20	-0.4957
-2	6	0.122224	0.002004	0.015302	0.017306	-0.02144	-0.0053	0.087734	0.01169	0.01154	20	0.0582
-1	6	0.20982	0.002721	0.015802	0.018523	-0.02129	-0.00582	0.055517	0.011451	0.011303	20	0.1489
0	6	0.297011	0.003947	0.016262	0.020209	-0.02143	-0.00637	0.023142	0.01127	0.011125	20	0.1863
1	6	0.383683	0.005682	0.016761	0.022443	-0.02189	-0.00693	-0.00923	0.011155	0.011007	20	0.2068
2	6	0.469724	0.007926	0.017052	0.024978	-0.02264	-0.00751	-0.04143	0.0111	0.01095	20	0.2197
3	6	0.555022	0.010675	0.017414	0.028089	-0.0237	-0.00809	-0.07329	0.01111	0.010953	20	0.2287
4	6	0.639463	0.013924	0.017728	0.031652	-0.02507	-0.00867	-0.10463	0.011182	0.011017	20	0.2353
5	6	0.722935	0.017662	0.018146	0.035809	-0.02674	-0.00925	-0.13525	0.011316	0.01114	20	0.2404
6	6	0.805328	0.021875	0.018699	0.040574	-0.02873	-0.00981	-0.16496	0.01151	0.011318	20	0.2443
7	6	0.886529	0.026583	0.019388	0.045971	-0.031	-0.01036	-0.19353	0.011761	0.01155	20	0.2475
8	6	0.966443	0.032185	0.020206	0.052392	-0.03353	-0.01089	-0.22054	0.012065	0.011832	20	0.25
9	6	1.045684	0.036933	0.021185	0.058118	-0.03625	-0.01141	-0.24789	0.012308	0.012048	20	0.2523

Table A.8. $\alpha = -6^\circ \div 9^\circ$ and $\beta = 7^\circ$

α [°]	β [°]	CL	CDi	CDv	CD	CY	Cl	Cm	Cn	Cni	QInf	XCP
-6	7	-0.22836	0.004471	0.029411	0.033883	-0.02911	-0.00419	0.203563	0.01536	0.015153	20	0.3818
-5	7	-0.14058	0.003193	0.021899	0.025092	-0.02756	-0.00464	0.174879	0.014775	0.014629	20	0.4512
-4	7	-0.05277	0.002407	0.017243	0.019651	-0.02635	-0.00513	0.144864	0.014319	0.014161	20	0.7497
-3	7	0.034983	0.002118	0.015814	0.017931	-0.02548	-0.00567	0.113804	0.013907	0.013754	20	-0.446
-2	7	0.12255	0.002329	0.015304	0.017633	-0.02495	-0.00625	0.082119	0.013583	0.01341	20	0.0685
-1	7	0.209828	0.003046	0.015798	0.018845	-0.02477	-0.00686	0.050005	0.013303	0.013132	20	0.1544
0	7	0.296705	0.00427	0.016247	0.020518	-0.02494	-0.0075	0.017711	0.013091	0.012923	20	0.1899
1	7	0.383071	0.006003	0.016745	0.022748	-0.02546	-0.00816	-0.0146	0.012955	0.012783	20	0.2095
2	7	0.468813	0.008242	0.017034	0.025275	-0.02634	-0.00883	-0.04676	0.012888	0.012714	20	0.2219
3	7	0.553821	0.010984	0.017391	0.028376	-0.02757	-0.00951	-0.07861	0.012897	0.012716	20	0.2305
4	7	0.637983	0.014224	0.017706	0.03193	-0.02915	-0.01019	-0.10999	0.012978	0.012787	20	0.2369
5	7	0.72119	0.017953	0.018122	0.036076	-0.03109	-0.01086	-0.1407	0.013131	0.012926	20	0.2417
6	7	0.803335	0.022161	0.018679	0.04084	-0.03338	-0.01153	-0.17056	0.013354	0.01313	20	0.2456
7	7	0.88432	0.026806	0.019366	0.046172	-0.03602	-0.01217	-0.1995	0.013644	0.013397	20	0.2487
8	7	0.96422	0.031054	0.020186	0.05124	-0.03911	-0.01282	-0.2288	0.014	0.013727	20	0.2516
9	7	1.039788	0.037491	0.021137	0.058628	-0.04141	-0.0132	-0.23908	0.014017	0.013714	20	0.2505

Table A.9. $\alpha = -6^\circ \div 9^\circ$ and $\beta = 8^\circ$

α [°]	β [°]	CL	CDi	CDv	CD	CY	Cl	Cm	Cn	Cni	QInf	XCP
-6	8	-0.22647	0.004821	0.029377	0.034198	-0.0332	-0.00488	0.19658	0.017484	0.017246	20	0.3758
-5	8	-0.13908	0.003553	0.021886	0.025439	-0.03143	-0.00539	0.168053	0.016817	0.016648	20	0.4422
-4	8	-0.05164	0.002773	0.017267	0.02004	-0.03005	-0.00595	0.138179	0.016296	0.016114	20	0.7316
-3	8	0.035727	0.002487	0.015834	0.018321	-0.02905	-0.00657	0.107263	0.015824	0.015649	20	-0.3915
-2	8	0.122922	0.002701	0.015309	0.01801	-0.02845	-0.00723	0.075714	0.015453	0.015255	20	0.0802
-1	8	0.209832	0.003418	0.015797	0.019215	-0.02824	-0.00792	0.043724	0.015131	0.014936	20	0.1606
0	8	0.296348	0.004641	0.016236	0.020877	-0.02842	-0.00865	0.011535	0.014888	0.014695	20	0.1941
1	8	0.382359	0.00637	0.016725	0.023095	-0.02901	-0.00941	-0.0207	0.014728	0.014534	20	0.2126
2	8	0.467757	0.008604	0.017013	0.025617	-0.03	-0.01018	-0.05281	0.014649	0.014452	20	0.2244
3	8	0.552429	0.011134	0.017366	0.028706	-0.03139	-0.01096	-0.08464	0.014655	0.01445	20	0.2326
4	8	0.636268	0.014572	0.017685	0.032257	-0.03318	-0.01174	-0.11603	0.014745	0.014527	20	0.2386
5	8	0.719164	0.018296	0.018105	0.036401	-0.03538	-0.01251	-0.1468	0.014917	0.014681	20	0.2433
6	8	0.801008	0.022511	0.018662	0.041173	-0.03797	-0.01327	-0.17678	0.015166	0.014909	20	0.247
7	8	0.881691	0.027235	0.019349	0.046584	-0.04095	-0.01401	-0.20575	0.015491	0.015207	20	0.25
8	8	0.961188	0.033045	0.020165	0.05321	-0.04426	-0.01473	-0.23348	0.015885	0.015571	20	0.2524
9	8	1.041286	0.038759	0.021134	0.059893	-0.04742	-0.01553	-0.26556	0.016055	0.015704	20	0.2553

Table A.10. $\alpha = -6^\circ \div 9^\circ$ and $\beta = 9^\circ$

α [°]	β [°]	CL	CDi	CDv	CD	CY	Cl	Cm	Cn	Cni	QInf	XCP
-6	9	-0.22435	0.005215	0.029339	0.034554	-0.03726	-0.00561	0.188739	0.01958	0.019311	20	0.3688
-5	9	-0.13738	0.003956	0.021868	0.025824	-0.03528	-0.00618	0.160388	0.018832	0.01864	20	0.4319
-4	9	-0.05038	0.003184	0.017294	0.020478	-0.03372	-0.00681	0.130682	0.018244	0.01804	20	0.7105
-3	9	0.036564	0.002903	0.015857	0.018759	-0.0326	-0.0075	0.099929	0.017713	0.017516	20	-0.333
-2	9	0.123336	0.003119	0.015318	0.018437	-0.03191	-0.00824	0.068548	0.017295	0.017073	20	0.0932
-1	9	0.209829	0.003838	0.015797	0.019635	-0.03167	-0.00902	0.036704	0.016932	0.016713	20	0.1676
0	9	0.295936	0.005059	0.016224	0.021283	-0.03187	-0.00984	0.004642	0.016655	0.01644	20	0.1988
1	9	0.381547	0.006785	0.016707	0.023492	-0.03252	-0.01069	-0.02749	0.016471	0.016255	20	0.2161
2	9	0.466552	0.009014	0.016992	0.026005	-0.03361	-0.01156	-0.05953	0.016379	0.016159	20	0.2271
3	9	0.550844	0.011742	0.017342	0.029084	-0.03516	-0.01243	-0.09132	0.016383	0.016153	20	0.2348
4	9	0.634313	0.014966	0.017672	0.032638	-0.03716	-0.01332	-0.12271	0.016481	0.016235	20	0.2406
5	9	0.716851	0.018682	0.018091	0.036773	-0.03961	-0.01419	-0.15353	0.016669	0.016403	20	0.245
6	9	0.798349	0.022891	0.01865	0.041541	-0.0425	-0.01505	-0.18361	0.016944	0.016653	20	0.2485
7	9	0.878697	0.027644	0.019335	0.046979	-0.04581	-0.0159	-0.21277	0.017301	0.016979	20	0.2514
8	9	0.958032	0.033338	0.020151	0.053488	-0.04948	-0.01673	-0.2416	0.017723	0.017366	20	0.2539
9	9	1.03633	0.038248	0.021107	0.059355	-0.05337	-0.01746	-0.26541	0.018054	0.017656	20	0.2551

Table A.11. $\alpha = -6^\circ \div 9^\circ$ and $\beta = 10^\circ$

α [°]	β [°]	CL	CDi	CDv	CD	CY	Cl	Cm	Cn	Cni	QInf	XCP
-6	10	-0.22198	0.005653	0.029295	0.034947	-0.04129	-0.00638	0.180063	0.021646	0.021345	20	0.361
-5	10	-0.1355	0.004404	0.021846	0.02625	-0.03909	-0.007	0.151912	0.020816	0.020601	20	0.4201
-4	10	-0.04898	0.00364	0.017323	0.020963	-0.03736	-0.0077	0.122399	0.020164	0.019936	20	0.686
-3	10	0.037489	0.003365	0.015887	0.019251	-0.03611	-0.00847	0.091844	0.019572	0.019354	20	-0.2715
-2	10	0.12379	0.003585	0.015327	0.018912	-0.03535	-0.00929	0.060649	0.019107	0.018861	20	0.1074
-1	10	0.209819	0.004304	0.0158	0.020104	-0.03507	-0.01016	0.028981	0.018701	0.018459	20	0.1753
0	10	0.295468	0.005525	0.016212	0.021737	-0.03528	-0.01107	-0.00293	0.018391	0.018153	20	0.204
1	10	0.38063	0.007248	0.016691	0.023939	-0.03598	-0.01201	-0.03493	0.018183	0.017945	20	0.2199
2	10	0.465198	0.009471	0.016975	0.026445	-0.03719	-0.01297	-0.06687	0.018077	0.017834	20	0.2302
3	10	0.549062	0.012192	0.017326	0.029517	-0.03889	-0.01395	-0.09859	0.018077	0.017822	20	0.2373
4	10	0.632116	0.015406	0.017662	0.033068	-0.04109	-0.01493	-0.12995	0.018181	0.017907	20	0.2427
5	10	0.714251	0.019107	0.018084	0.037191	-0.04378	-0.01591	-0.1608	0.018385	0.018088	20	0.2468
6	10	0.795359	0.023277	0.018642	0.041919	-0.04697	-0.01687	-0.19098	0.018685	0.018359	20	0.2502
7	10	0.875332	0.027833	0.019327	0.04716	-0.05065	-0.01782	-0.2204	0.019079	0.018717	20	0.253
8	10	0.953617	0.032187	0.020143	0.05233	-0.05495	-0.01871	-0.24728	0.019571	0.01917	20	0.255
9	10	1.031757	0.039081	0.021087	0.060168	-0.05857	-0.01951	-0.26931	0.019746	0.019299	20	0.2556

Table A.12. $\delta_{f_1}^f$ for $\alpha = -6^\circ \div 9^\circ$ and $\beta = 0^\circ$

α [°]	β [°]	CL	CDi	CDv	CD	CY	Cl	Cm	Cn	Cni	QInf	XCP
-6	0	-0.218873	0.003055	0.027851	0.030905	0	0	0.229708	-0.000001	0	20	0.4185
-5	0	-0.129836	0.001865	0.022085	0.023951	0	0	0.200428	0.000001	0	20	0.5186
-4	0	-0.040779	0.001164	0.017763	0.018927	0	0	0.170099	0.000001	0	20	1.0533
-3	0	0.048187	0.000961	0.016573	0.017534	0	0	0.138751	0	0	20	-0.3843
-2	0	0.13695	0.001263	0.015906	0.017169	0	0	0.106844	0	0	20	0.0434
-1	0	0.225398	0.002076	0.016047	0.018123	0	0	0.074539	0	0	20	0.1348
0	0	0.313418	0.0034	0.016414	0.019815	0	0	0.042082	0	0	20	0.1748
1	0	0.400895	0.005239	0.016813	0.022051	0	0	0.009673	0	0	20	0.1973
2	0	0.487716	0.007589	0.017053	0.024642	0	0	-0.022507	0	0	20	0.2117
3	0	0.573767	0.010451	0.017336	0.027787	0	0	-0.054276	0	0	20	0.2217
4	0	0.658934	0.013819	0.017686	0.031504	0	0	-0.085442	0	0	20	0.2291
5	0	0.743103	0.017687	0.018145	0.035832	0	0	-0.115801	0	0	20	0.2347
6	0	0.826162	0.022048	0.018736	0.040784	0	0	-0.145145	0	0	20	0.2391
7	0	0.908	0.0269	0.019467	0.046367	0	0	-0.173284	0	0	20	0.2426
8	0	0.988554	0.032389	0.020324	0.052714	0	0	-0.200159	0	0	20	0.2455
9	0	1.074584	0.036788	0.021354	0.058142	0	0	-0.255642	0	0	20	0.2532

Table A.13. $\delta_{f_2}^f$ for $\alpha = -6^\circ \div 9^\circ$ and $\beta = 0^\circ$

α [°]	β [°]	CL	CDi	CDv	CD	CY	Cl	Cm	Cn	Cni	QInf	XCP
-6	0	-0.219696	0.003136	0.028559	0.031695	0	0	0.222128	0	0	20	0.4108
-5	0	-0.130627	0.001916	0.021706	0.023622	0	0	0.192829	0	0	20	0.5047
-4	0	-0.041536	0.001183	0.017102	0.018284	0	0	0.16229	-0.000001	0	20	0.9992
-3	0	0.047465	0.000947	0.015653	0.0166	0	0	0.130719	-0.000001	0	20	-0.3585
-2	0	0.136264	0.001217	0.015487	0.016704	0	0	0.098524	-0.000001	0	20	0.055
-1	0	0.224749	0.001996	0.015901	0.017896	0	0	0.065967	0	0	20	0.1423
0	0	0.312804	0.003286	0.016342	0.019628	0	0	0.033281	0	0	20	0.1804
1	0	0.400315	0.00509	0.016721	0.021811	0	0	0.000659	0	0	20	0.2018
2	0	0.487168	0.007405	0.017024	0.024429	0	0	-0.031721	0	0	20	0.2155
3	0	0.573246	0.010229	0.01741	0.027639	0	0	-0.063662	0	0	20	0.225
4	0	0.658435	0.013559	0.017755	0.031314	0	0	-0.094979	0	0	20	0.232
5	0	0.742618	0.017388	0.018223	0.035611	0	0	-0.125449	0	0	20	0.2374
6	0	0.82568	0.021707	0.018828	0.040535	0	0	-0.154859	0	0	20	0.2415
7	0	0.90751	0.026513	0.01957	0.046083	0	0	-0.183008	0	0	20	0.2448
8	0	0.988047	0.031928	0.020431	0.052359	0	0	-0.209864	0	0	20	0.2475
9	0	1.075918	0.035964	0.02148	0.057443	0	0	-0.273089	0	0	20	0.2565

Table A.14. δ_a^α for $\alpha = -6^\circ \div 9^\circ$ and $\beta = 0^\circ$

α [°]	β [°]	CL	CDi	CDv	CD	CY	Cl	Cm	Cn	Cni	QInf	XCP
-6	0	-0.234594	0.003253	0.029041	0.032293	-0.00049	-0.002973	0.226778	-0.000009	0.000037	20	0.4014
-5	0	-0.145553	0.001975	0.021475	0.02345	-0.000387	-0.002972	0.197645	0.000067	0.000024	20	0.48
-4	0	-0.056483	0.001184	0.017122	0.018306	-0.000283	-0.002971	0.167178	0.000118	0.000011	20	0.805
-3	0	0.032503	0.00089	0.015766	0.016656	-0.00018	-0.00297	0.135685	0.000079	-0.000003	20	-0.6463
-2	0	0.121293	0.001102	0.015268	0.016369	-0.000076	-0.00297	0.103604	0.000037	-0.000016	20	0.0287
-1	0	0.209775	0.001822	0.015766	0.017588	0.000028	-0.00297	0.071138	-0.000005	-0.000029	20	0.1333
0	0	0.297833	0.003055	0.016236	0.019291	0.000132	-0.00297	0.038555	-0.000046	-0.000042	20	0.1758
1	0	0.385354	0.004802	0.016785	0.021587	0.000235	-0.00297	0.006037	-0.000074	-0.000055	20	0.199
2	0	0.472222	0.007061	0.017109	0.024171	0.000337	-0.002971	-0.026225	-0.000091	-0.000067	20	0.2136
3	0	0.558321	0.009831	0.017479	0.02731	0.000439	-0.002972	-0.058041	-0.000097	-0.000079	20	0.2236
4	0	0.643537	0.013107	0.017803	0.03091	0.000539	-0.002972	-0.089228	-0.000101	-0.000091	20	0.2309
5	0	0.727753	0.016883	0.01824	0.035123	0.000639	-0.002974	-0.119563	-0.000102	-0.000102	20	0.2364
6	0	0.810854	0.021151	0.018809	0.03996	0.000737	-0.002975	-0.148835	-0.000101	-0.000113	20	0.2407
7	0	0.892729	0.025906	0.019512	0.045418	0.000833	-0.002976	-0.176843	-0.000097	-0.000123	20	0.2441
8	0	0.973319	0.031266	0.020335	0.0516	0.000928	-0.002977	-0.203561	-0.00009	-0.000133	20	0.2469
9	0	1.061369	0.035255	0.021326	0.056581	0.001053	-0.002979	-0.267161	-0.000092	-0.000154	20	0.256

Table A.15. $\delta_{f_1}^a$ for $\alpha = -6^\circ \div 9^\circ$ and $\beta = 0^\circ$

α [°]	β [°]	CL	CDi	CDv	CD	CY	Cl	Cm	Cn	Cni	QInf	XCP
-6	0	-0.234605	0.003275	0.027987	0.031262	0.000185	-0.001393	0.226985	-0.00024	-0.000235	20	0.4014
-5	0	-0.145559	0.001994	0.021745	0.023739	0.000289	-0.001394	0.197632	-0.000196	-0.000254	20	0.48
-4	0	-0.056485	0.001202	0.017642	0.018844	0.000397	-0.001395	0.167115	-0.000266	-0.000273	20	0.805
-3	0	0.032506	0.000909	0.016433	0.017343	0.000508	-0.001397	0.135622	-0.000285	-0.000294	20	-0.6462
-2	0	0.121301	0.001122	0.015977	0.017099	0.000624	-0.0014	0.103558	-0.000325	-0.000315	20	0.0287
-1	0	0.209788	0.001846	0.01624	0.018086	0.000744	-0.001403	0.07112	-0.000359	-0.000337	20	0.1333
0	0	0.297851	0.003083	0.016605	0.019688	0.000867	-0.001406	0.038551	-0.000383	-0.000359	20	0.1758
1	0	0.385377	0.004833	0.016929	0.021762	0.000995	-0.001411	0.006046	-0.000396	-0.000381	20	0.199
2	0	0.472249	0.007096	0.017182	0.024278	0.001127	-0.001416	-0.026211	-0.000416	-0.000402	20	0.2136
3	0	0.558353	0.00987	0.017471	0.027341	0.001262	-0.001422	-0.058027	-0.000436	-0.000423	20	0.2236
4	0	0.643572	0.013148	0.017798	0.030946	0.0014	-0.001428	-0.089209	-0.000452	-0.000442	20	0.2309
5	0	0.727792	0.016926	0.018239	0.035165	0.001539	-0.001435	-0.11954	-0.000467	-0.000459	20	0.2364
6	0	0.810897	0.021196	0.018808	0.040003	0.001678	-0.001443	-0.148807	-0.000478	-0.000473	20	0.2407
7	0	0.892775	0.025951	0.019515	0.045466	0.001815	-0.00145	-0.17681	-0.000483	-0.000481	20	0.2441
8	0	0.973367	0.031312	0.020348	0.05166	0.001953	-0.001456	-0.203521	-0.000484	-0.000486	20	0.2469
9	0	1.061474	0.035276	0.021354	0.05663	0.003914	-0.001508	-0.267044	-0.001123	-0.001128	20	0.256

Table A.16. $\delta_{f_2}^a$ for $\alpha = -6^\circ \div 9^\circ$ and $\beta = 0^\circ$

α [°]	β [°]	CL	CDi	CDv	CD	CY	Cl	Cm	Cn	Cni	QInf	XCP
-6	0	-0.234597	0.003265	0.029374	0.032639	-0.000486	-0.003161	0.226757	-0.000305	-0.000104	20	0.4014
-5	0	-0.145554	0.001987	0.02215	0.024137	-0.000343	-0.003165	0.197588	-0.000218	-0.000116	20	0.48
-4	0	-0.056484	0.001196	0.017376	0.018572	-0.0002	-0.003169	0.167154	-0.000215	-0.000127	20	0.805
-3	0	0.032503	0.000902	0.015748	0.01665	-0.000058	-0.003173	0.135686	-0.000171	-0.000137	20	-0.6463
-2	0	0.121294	0.001114	0.015412	0.016526	0.000084	-0.003178	0.103596	-0.000144	-0.000146	20	0.0287
-1	0	0.209777	0.001835	0.015901	0.017735	0.000224	-0.003182	0.071133	-0.000163	-0.000154	20	0.1333
0	0	0.297836	0.003069	0.016371	0.019439	0.000362	-0.003186	0.03855	-0.000175	-0.000161	20	0.1758
1	0	0.385358	0.004816	0.016828	0.021644	0.000497	-0.003191	0.006038	-0.000193	-0.000166	20	0.199
2	0	0.472227	0.007077	0.017112	0.024189	0.00063	-0.003195	-0.026222	-0.000191	-0.000169	20	0.2136
3	0	0.558327	0.009848	0.017481	0.027329	0.00076	-0.003198	-0.058038	-0.000187	-0.000171	20	0.2236
4	0	0.643543	0.013125	0.017802	0.030928	0.000886	-0.003201	-0.089225	-0.000181	-0.000171	20	0.2309
5	0	0.72776	0.016903	0.018241	0.035144	0.001008	-0.003204	-0.11956	-0.000173	-0.00017	20	0.2364
6	0	0.810863	0.021172	0.018813	0.039984	0.001126	-0.003205	-0.148831	-0.000162	-0.000168	20	0.2407
7	0	0.892739	0.025928	0.019517	0.045445	0.001239	-0.003206	-0.176838	-0.000148	-0.000164	20	0.2441
8	0	0.973329	0.031289	0.02034	0.051629	0.001348	-0.003206	-0.203557	-0.000134	-0.000159	20	0.2469
9	0	1.061382	0.03528	0.021344	0.056624	0.001715	-0.003211	-0.267156	-0.000209	-0.000245	20	0.256

Table A.17. δ_a^f for $\alpha = -6^\circ \div 9^\circ$ and $\beta = 0^\circ$

α [°]	β [°]	CL	CDi	CDv	CD	CY	Cl	Cm	Cn	Cni	QInf	XCP
-6	0	-0.226101	0.003177	0.028809	0.031986	0	0	0.219014	0.000001	0	20	0.402
-5	0	-0.137048	0.001936	0.021496	0.023432	0	0	0.189789	0.000001	0	20	0.4858
-4	0	-0.047971	0.001182	0.017389	0.01857	0	0	0.15924	0.000001	0	20	0.879
-3	0	0.041018	0.000925	0.015965	0.01689	0	0	0.127704	0.000001	0	20	-0.4315
-2	0	0.129807	0.001173	0.01543	0.016603	0	0	0.095588	0.000001	0	20	0.0524
-1	0	0.218282	0.00193	0.015847	0.017778	0	0	0.0631	0	0	20	0.1433
0	0	0.30633	0.0032	0.016241	0.019441	0	0	0.030505	0	0	20	0.1818
1	0	0.393835	0.004983	0.016743	0.021726	0	0	-0.002016	0	0	20	0.2032
2	0	0.480683	0.007279	0.017049	0.024328	0	0	-0.034274	0	0	20	0.2168
3	0	0.566758	0.010084	0.017435	0.027518	0	0	-0.066074	0	0	20	0.2262
4	0	0.651945	0.013395	0.017779	0.031174	0	0	-0.097235	0	0	20	0.233
5	0	0.736127	0.017206	0.018243	0.035448	0	0	-0.127532	0	0	20	0.2382
6	0	0.81919	0.021507	0.018842	0.040349	0	0	-0.156754	0	0	20	0.2423
7	0	0.901022	0.026296	0.019581	0.045877	0	0	-0.1847	0	0	20	0.2455
8	0	0.981564	0.03169	0.020446	0.052136	0	0	-0.211345	0	0	20	0.2482
9	0	1.069558	0.035706	0.021482	0.057188	0	0	-0.274838	0	0	20	0.2571

Table A.18. δ_t^e for $\alpha = -6^\circ \div 9^\circ$ and $\beta = 0^\circ$

α [°]	β [°]	CL	CDi	CDv	CD	CY	Cl	Cm	Cn	Cni	QInf	XCP
-6	0	-0.228515	0.002705	0.029575	0.03228	0	0	0.201094	0	0	20	0.3831
-5	0	-0.139446	0.001543	0.022025	0.023568	0	0	0.171529	0	0	20	0.4533
-4	0	-0.050357	0.000845	0.01726	0.018104	0	0	0.140691	0	0	20	0.7699
-3	0	0.038642	0.000631	0.015837	0.016468	0	0	0.108839	0	0	20	-0.3693
-2	0	0.127441	0.000916	0.015382	0.016298	0	0	0.07643	0	0	20	0.0804
-1	0	0.215928	0.00171	0.015892	0.017601	0	0	0.043671	0	0	20	0.161
0	0	0.303988	0.003016	0.016363	0.019379	0	0	0.010834	0	0	20	0.1948
1	0	0.391507	0.004837	0.016856	0.021693	0	0	-0.021896	0	0	20	0.2134
2	0	0.478371	0.007172	0.017138	0.02431	0	0	-0.054337	0	0	20	0.2252
3	0	0.564464	0.010018	0.0175	0.027518	0	0	-0.086299	0	0	20	0.2334
4	0	0.64967	0.013372	0.01782	0.031192	0	0	-0.117591	0	0	20	0.2394
5	0	0.733876	0.017226	0.018249	0.035475	0	0	-0.148001	0	0	20	0.2439
6	0	0.816966	0.021572	0.01881	0.040382	0	0	-0.177314	0	0	20	0.2474
7	0	0.898829	0.026397	0.019507	0.045904	0	0	-0.20533	0	0	20	0.2502
8	0	0.979398	0.031709	0.020326	0.052035	0	0	-0.232051	0	0	20	0.2525
9	0	1.056898	0.037744	0.021317	0.059061	0	0	-0.249817	0	0	20	0.253

Table A.19. δ_t^r for $\alpha = -6^\circ \div 9^\circ$ and $\beta = 0^\circ$

α [°]	β [°]	CL	CDi	CDv	CD	CY	Cl	Cm	Cn	Cni	QInf	XCP
-6	0	-0.234617	0.00321	0.029505	0.032715	0.00385	0.001089	0.226806	-0.002027	-0.002022	20	0.4014
-5	0	-0.145569	0.001959	0.021972	0.023931	0.003796	0.001001	0.197675	-0.002015	-0.002011	20	0.48
-4	0	-0.056496	0.001182	0.017203	0.018385	0.003745	0.000915	0.167231	-0.001997	-0.001994	20	0.8049
-3	0	0.032493	0.000894	0.015795	0.016689	0.003693	0.00083	0.135741	-0.001973	-0.001971	20	-0.6466
-2	0	0.121284	0.001108	0.015345	0.016453	0.003638	0.000747	0.103654	-0.001944	-0.001942	20	0.0287
-1	0	0.209767	0.001829	0.015865	0.017694	0.003581	0.000666	0.071181	-0.001909	-0.001908	20	0.1332
0	0	0.297826	0.003062	0.016344	0.019406	0.003522	0.000587	0.038592	-0.001869	-0.001868	20	0.1758
1	0	0.385348	0.004808	0.016845	0.021653	0.00346	0.000512	0.006074	-0.001824	-0.001824	20	0.199
2	0	0.472216	0.007066	0.017135	0.024201	0.003397	0.00044	-0.02619	-0.001774	-0.001774	20	0.2136
3	0	0.558316	0.009834	0.017499	0.027334	0.003333	0.000372	-0.058014	-0.00172	-0.00172	20	0.2236
4	0	0.643532	0.013108	0.017823	0.030931	0.003267	0.000308	-0.089201	-0.001661	-0.001661	20	0.2309
5	0	0.727749	0.01688	0.01826	0.03514	0.0032	0.000248	-0.11954	-0.001598	-0.001599	20	0.2364
6	0	0.810851	0.021143	0.018827	0.03997	0.003132	0.000192	-0.148815	-0.001532	-0.001532	20	0.2407
7	0	0.892727	0.025896	0.019529	0.045425	0.003061	0.000142	-0.176827	-0.001462	-0.001463	20	0.2441
8	0	0.973317	0.031255	0.020354	0.051609	0.002992	0.000096	-0.203551	-0.00139	-0.001391	20	0.2469
9	0	1.052405	0.03693	0.02135	0.05828	0.002416	0.000071	-0.228411	-0.001105	-0.001106	20	0.2491

Table A.20. δ_s^s for $\alpha = -6^\circ \div 9^\circ$ and $\beta = 0^\circ$

α [°]	β [°]	CL	CDi	CDv	CD	CY	Cl	Cm	Cn	Cni	QInf	XCP
-6	0	-0.2346	0.003233	0	0.003233	0	0	0.227114	0	0	20	0.4014
-5	0	-0.14555	0.001955	0	0.001955	0	0	0.19694	0	0	20	0.48
-4	0	-0.05648	0.001164	0	0.001164	0	0	0.165929	0	0	20	0.805
-3	0	0.032503	0.000871	0	0.000871	0	0	0.134249	0	0	20	-0.6462
-2	0	0.121294	0.001082	0	0.001082	0	0	0.102069	0	0	20	0.0287
-1	0	0.209775	0.001802	0	0.001802	0	0	0.069568	0	0	20	0.1333
0	0	0.297834	0.003035	0	0.003035	0	0	0.036928	0	0	20	0.1758
1	0	0.385355	0.004781	0	0.004781	0	0	0.004338	0	0	20	0.199
2	0	0.472223	0.00704	0	0.00704	0	0	-0.02801	0	0	20	0.2136
3	0	0.558323	0.009809	0	0.009809	0	0	-0.05991	0	0	20	0.2236
4	0	0.643538	0.013084	0	0.013084	0	0	-0.09117	0	0	20	0.2309
5	0	0.727755	0.016859	0	0.016859	0	0	-0.12158	0	0	20	0.2364
6	0	0.810856	0.021126	0	0.021126	0	0	-0.15093	0	0	20	0.2407
7	0	0.892732	0.02588	0	0.02588	0	0	-0.17902	0	0	20	0.2441
8	0	0.973321	0.031239	0	0.031239	0	0	-0.20583	0	0	20	0.2469
9	0	1.061372	0.035228	0	0.035228	0	0	-0.26951	0	0	20	0.256

Table A.21. C_y

α [°]	$C_{y(\delta_a^a)}$ [1/rad]	$C_{y(\delta_{f_1}^a)}$ [1/rad]	$C_{y(\delta_{f_2}^a)}$ [1/rad]	$C_{y(\delta_r^a)}$ [1/rad]	$C_{y\beta}$ [1/rad]
-6	-0.02807	0.0106	-0.02785	0.220589	-0.23978
-5	-0.02217	0.016558	-0.01965	0.217495	-0.22712
-4	-0.01621	0.022746	-0.01146	0.214573	-0.21721
-3	-0.01031	0.029106	-0.00332	0.211593	-0.21016
-2	-0.00435	0.035753	0.004813	0.208442	-0.20592
-1	0.001604	0.042628	0.012834	0.205176	-0.2046
0	0.007563	0.049675	0.020741	0.201796	-0.20615
1	0.013465	0.057009	0.028476	0.198243	-0.21062
2	0.019309	0.064572	0.036096	0.194634	-0.21801
3	0.025153	0.072307	0.043545	0.190967	-0.22838
4	0.030882	0.080214	0.050764	0.187185	-0.24173
5	0.036612	0.088178	0.057754	0.183346	-0.25795
6	0.042227	0.096142	0.064515	0.17945	-0.27714
7	0.047727	0.103992	0.070989	0.175382	-0.2992
8	0.05317	0.111899	0.077235	0.171429	-0.32395
9	0.060332	0.224256	0.098262	0.138427	-0.34945

Table A.22. C_L

α [°]	$C_{L(\delta_{f_1}^f)}$ [1/rad]	$C_{L(\delta_{f_2}^f)}$ [1/rad]	$C_{L(\delta_a^f)}$ [1/rad]	$C_{L(\delta_{f_1}^f)}$ [1/rad]	$C_{L(\delta_{f_2}^f)}$ [1/rad]	$C_{L(\delta_r^f)}$ [1/rad]	$C_{L(\delta_f^f)}$ [1/rad]	$C_{L(\delta_r^f)}$ [1/rad]	$C_{L\beta}$ [1/rad]
-6	0.942630165	0.895475738	0.041883215	0.041252961	0.041711327	0.52849627	0.390184258	0.0405654	0.049217075
-5	0.946812756	0.901491795	0.04629499	0.045951215	0.046237694	0.533595595	0.396200315	0.0453783	0.052196455
-4	0.94526577	0.901892865	0.045492849	0.045378257	0.045435553	0.533194524	0.396486794	0.044748	0.049847328
-3	0.934837939	0.893470386	0.036210933	0.03638282	0.036210933	0.524084495	0.387949723	0.035638	0.039133017
-2	0.912206106	0.872901201	0.015126086	0.015584452	0.015183382	0.502942353	0.367380538	0.0146104	0.016673072
-1	0.874104412	0.836919451	-0.021027551	-0.020282706	-0.02091296	0.466387645	0.33151338	-0.021486	-0.02091296
0	0.817152407	0.781972799	-0.075802316	-0.074770992	-0.075630429	0.411039922	0.276853207	-0.076203	-0.077005528
1	0.738026936	0.704795384	-0.152406774	-0.151088971	-0.15217759	0.333518733	0.200134158	-0.152751	-0.154985084
2	0.633232955	0.601834868	-0.254507853	-0.252960867	-0.254221374	0.230271738	0.097803896	-0.254852	-0.258403966
3	0.499390014	0.469538913	-0.385600596	-0.383767131	-0.385256821	0.097803896	-0.033632623	-0.385887	-0.39069992
4	0.333060366	0.304469772	-0.549122751	-0.547117399	-0.548778976	-0.067379837	-0.197727735	-0.549409	-0.555482582
5	0.130748969	0.102960516	-0.748741247	-0.746506711	-0.748340176	-0.268946389	-0.397919189	-0.74897	-0.75630429
6	-0.110867333	-0.138483899	-0.987951126	-0.985487408	-0.987435464	-0.510333508	-0.637759322	-0.988123	-0.996660085
7	-0.395283583	-0.423358515	-1.270247432	-1.267611826	-1.269674474	-0.795093532	-0.920743177	-1.270362	-1.280388785
8	-0.723130033	-0.752178993	-1.596031234	-1.593281037	-1.595458276	-1.123627532	-1.24773019	-1.596146	-1.613678334
9	-0.70416513	-0.62773256	-1.461328856	-1.4553128	-1.460584011	-0.992133718	-1.717498287	-1.974928	-1.986731155

Table A.23. C_M

α [°]	$C_{M(\delta_{f_1}^a)}$ [1/rad]	$C_{M(\delta_{f_2}^a)}$ [1/rad]	$C_{M(\delta_a)}$ [1/rad]	$C_{M(\delta_{f_1}^s)}$ [1/rad]	$C_{M(\delta_{f_2}^s)}$ [1/rad]	$C_{M(\delta_f^s)}$ [1/rad]	$C_{M(\delta_s)}$ [1/rad]	$C_{M(\delta_Y)}$ [1/rad]	$C_{M\beta}$ [1/rad]
-6	-0.663370535	-1.097672544	-0.831247169	-0.819386943	-0.832450381	-1.276091601	-2.30283197	-0.829643	-0.860353425
-5	-0.455444151	-0.89083478	-0.614898306	-0.615643151	-0.618164165	-1.06501395	-2.111234883	-0.613179	-0.643832674
-4	-0.284530841	-0.731953583	-0.451891813	-0.455501447	-0.453266912	-0.906705711	-1.969485125	-0.448855	-0.478992717
-3	-0.150000351	-0.610200052	-0.325669211	-0.329278845	-0.325611915	-0.782946827	-1.863831708	-0.322461	-0.352025269
-2	-0.029450031	-0.506150916	-0.215088356	-0.217723962	-0.215546723	-0.674371325	-1.772043869	-0.212224	-0.241157936
-1	0.084855049	-0.406284373	-0.110007897	-0.111039221	-0.110294376	-0.570551372	-1.683751073	-0.107544	-0.13561911
0	0.202540581	-0.301719575	0.000458366	0.000229183	0.000171887	-0.460772659	-1.587837938	0.0025783	-0.024866368
1	0.332773887	-0.183690269	0.124446433	0.124962095	0.124503729	-0.336956479	-1.475996576	0.1265664	0.099465473
2	0.483633675	-0.044289638	0.270607967	0.271410108	0.270779854	-0.190565763	-1.340090987	0.2726133	0.245741598
3	0.663771606	0.125993419	0.448052996	0.448855137	0.448224883	-0.012204001	-1.171011142	0.4496	0.422842853
4	0.8824123	0.335982451	0.665490479	0.666579099	0.665662366	0.206723172	-0.959589715	0.6670375	0.64022304
5	1.148608492	0.595818811	0.933061769	0.934379572	0.933233657	0.476471702	-0.696315608	0.9343796	0.907278669
6	1.471928576	0.915357374	1.260507149	1.262111431	1.260736332	0.806781871	-0.371219355	1.2616531	1.234093795
7	1.861253397	1.304109237	1.657337718	1.659228479	1.657624197	1.207164779	0.025152847	1.6582545	1.631210843
8	2.317786169	1.761730628	2.122865927	2.125157758	2.12309511	1.676875579	0.490509168	2.1234389	2.116276912
9	1.128325786	0.128686321	0.468335702	0.475039308	0.468622181	0.028476002	1.462073702	2.6885472	2.652966479

Table A.24. C_l

α [°]	$C_{l(\delta_a^a)}$ [1/rad]	$C_{l(\delta_{f_1}^a)}$ [1/rad]	$C_{l(\delta_{f_2}^a)}$ [1/rad]	$C_{l\beta}$ [1/rad]
-6	-0.170340352	-0.079813021	-0.181111959	-0.032257524
-5	-0.170283057	-0.079870317	-0.181341142	-0.035867158
-4	-0.170225761	-0.079927612	-0.181570325	-0.039935158
-3	-0.170168465	-0.080042204	-0.181799508	-0.044346933
-2	-0.170168465	-0.080214091	-0.182085987	-0.049102483
-1	-0.170168465	-0.080385979	-0.18231517	-0.054144512
0	-0.170168465	-0.080557866	-0.182544354	-0.059358428
1	-0.170168465	-0.080844345	-0.182830832	-0.064744231
2	-0.170225761	-0.081130824	-0.183060016	-0.070244626
3	-0.170283057	-0.081474598	-0.183231903	-0.075745021
4	-0.170283057	-0.081818373	-0.18340379	-0.081245415
5	-0.170397648	-0.082219444	-0.183575678	-0.086688514
6	-0.170454944	-0.08267781	-0.183632973	-0.091959726
7	-0.17051224	-0.08307888	-0.183690269	-0.09705905
8	-0.170569536	-0.083422655	-0.183690269	-0.101929192
9	-0.170684127	-0.086402036	-0.183976748	-0.106684741

Table A.25. C_n

α [°]	$C_{n(\delta_a^a)}$ [1/rad]	$C_{n(\delta_{f1}^a)}$ [1/rad]	$C_{n(\delta_{f2}^a)}$ [1/rad]	$C_{n(\delta_t^r)}$ [1/rad]	$C_{n\beta}$ [1/rad]
-6	-0.000515662	-0.013750987	-0.017475213	-0.116138545	0.127311222
-5	0.003838817	-0.011229973	-0.01249048	-0.115450996	0.122612968
-4	0.006760902	-0.015240677	-0.012318593	-0.114419672	0.118888742
-3	0.004526367	-0.016329297	-0.009797578	-0.113044573	0.115508291
-2	0.002119944	-0.018621128	-0.008250592	-0.111382995	0.112872686
-1	-0.000286479	-0.020569185	-0.009339212	-0.109377643	0.110580854
0	-0.002635606	-0.021944284	-0.010026761	-0.107085812	0.108919277
1	-0.004239888	-0.022689129	-0.011058085	-0.104507502	0.107830657
2	-0.005213916	-0.023835044	-0.010943494	-0.101642713	0.107372291
3	-0.005557691	-0.02498096	-0.010714311	-0.098548741	0.107544178
4	-0.005786874	-0.025897692	-0.010370536	-0.09516829	0.108289023
5	-0.00584417	-0.026757129	-0.00991217	-0.091558656	0.109664122
6	-0.005786874	-0.027387383	-0.009281916	-0.087777134	0.111612178
7	-0.005557691	-0.027673862	-0.008479775	-0.08376643	0.114075897
8	-0.00515662	-0.027731157	-0.007677634	-0.079641134	0.11688339
9	-0.005271212	-0.06434316	-0.011974818	-0.063311836	0.119175221

Bibliography

- [1] R. Baggi, E. Franco, A. Serrani. *Dynamic Control Allocation for a Class of Over-actuated Aircraft*. AIAA 2020-0841. 2020.
- [2] UCR SkyTeam - <http://skyteambcoe.ucr.acsitefactory.com/>
- [3] U.S. Department of Transportation, Federal Aviation Administration. *Pilot's Handbook of Aeronautical Knowledge*. 2016.
- [4] <https://booksite.elsevier.com/9780340741528/appendices/data-a/default.htm>
- [5] <http://www.b737.org.uk/techspecsoriginals.htm>
- [6] <https://www.airbus.com/aircraft/support-services/airport-operations-and-technical-data/autocad-3-view-aircraft-drawings.html>
- [7] M. Drela. *Basic sizing checks for homebrew RC thermal gliders*. The Journal for R/C Soaring Enthusiasts. Vol.21, N.8, pp. 13-15, 2004.
- [8] M. H. Sadraey. *Aircraft Design. A Systems Engineering Approach*. John Wiley & Sons, Ltd. 2013, pp. 631-638.
- [9] Brian L. Stevens, Frank L. Lewis, Eric N. Johnson. *Aircraft Control and Simulation, Third Edition. Dynamics, Control Desing, and Autonomous Systems*. John Wiley & Sons, 2011; pp. 111.
- [10] P. B. S. Lissaman. *Low-Reynolds-Number Airfoils*. Annu. Rev. Fluid Mech., 1983.
- [11] J. H. McMasters, M. L. Henderson. *Low speed single element airfoil synthesis*. Tech. Soaring 6(2):1-21, 1980.
- [12] H.P. Horton, *Laminar Separation Bubbles in Two- and Three-Dimensional Incompressible Flow*, Ph.D. Thesis, University of London, 1968.
- [13] L. L. Pauley, P. Moin, & W. C. Reynolds. *The structure of two-dimensional separation*. Journal of Fluid Mechanics, 220, pp. 397-411, 1990.
- [14] K. L. Hansen, R. M. Kelso, A. Choudhry, and M. Arjomandi. *Laminar Separation Bubble Effect on the Lift Curve Slope of an Airfoil*. 19th Australasian Fluid Mechanics Conference Melbourne, Australia, 8-11 December 2014.
- [15] J. D. Anderson, Jr. *Fundamentals of Aerodynamics, Third Edition*. McGraw-Hill Higher Education, 2001.
- [16] S. B. Pope. *Turbulent Flows*. Cambridge University Press, 2000, pp. 301.
- [17] S. B. Pope. *Turbulent Flows*. Cambridge University Press, 2000, pp. 276.
- [18] J. Windte, U. Scholz, R. Radespiel. *Validation of the RANS-simulation of laminar separation bubbles on airfoils*. Aerospace Science and Technology, 2006.

- [19] A. Crivellini et al. 2014 J. Phys.: Conf. Ser. 501 012024.
- [20] C. L. Rumsey, P. R. Spalart. *Turbulence Model Behavior in Low Reynolds Number Regions of Aerodynamic Flowfields*. 38th AIAA Fluid Dynamics Conference and Exhibit, June 23 – 26, 2008, Seattle, WA.
- [21] P. L. Delafin, F. Deniset, J. A. Astolfi. *Effect of the laminar separation bubble induced transition on the hydrodynamic performance of a hydrofoil*. European Journal of Mechanics-B/Fluids, Elsevier, 2014, Vol. 46, pp.190-200.
- [22] D. K. Walters, D. Cokljat. *A Three-Equation Eddy-Viscosity Model for Reynolds-Averaged Navier–Stokes Simulations of Transitional Flow*, J. Fluids Eng. Dec 2008, 130(12): 121401.
- [23] *ANSYS Fluent Theory Guide, Release 15*. pp. 625 - 669, 2013.
- [24] M. S. Selig, J.J. Guglielmo, A. P. Broeren, P. Giguère. *Summary of Low-Speed Airfoil Data, Volume 1*. SoarTech Publications, 1995.
- [25] Y. Zhang, Z. Sun and A. van Zuijlen and G. van Bussel. *Numerical simulation of transitional flow on a wind turbine airfoil with RANS-based transition model*. Journal of Turbulence, V. 18, n. 9, pp 879-898, Taylor & Francis, 2017.
- [26] P. Catalano, R. Tognaccini. *RANS analysis of the low-Reynolds number flow around the SD7003 airfoil*. Aerospace Science and Technology, Volume 15, Issue 8, December 2011, pp 615-626.
- [27] XFLR5 - <http://www.xflr5.tech/xflr5.htm>
- [28] T. C. Shafer, C. E. Lynch, S. A. Viken, N. Favaregh, C. Zeune, N. Williams, J. Dansie. *Comparison of Computational Approaches for Rapid Aerodynamic Assessment of Small UAVs*. AIAA Science and Technology Forum and Exposition.
- [29] A. Deperrois. *Analysis of foils and wings operating at low Reynolds numbers*. Guidelines for XFLR5, Vol.4, 2009.
- [30] B. Etkin. *Dynamics of Atmospheric Flight*. Dover Publications Inc, 2005, pp. 199.
- [31] B. Etkin. *Dynamics of Atmospheric Flight*. Dover Publications Inc, 2005, pp. 200 - 215.
- [32] J. C. Heitmeyer, (National Advisory Committee for Aeronautics. Ames Aeronautical Lab., Moffett Field, CA, United States). *Effect of a Leading-edge Flap upon the Lift, Drag, and Pitching Moment of an Airplane Employing a Thin, Unswept Wing*. 1954.